Technische Universität München

Fakultät für Physik

Electrochemical Scanning Probe Microscopy Studies of Enzyme Immobilization on Model Electrodes

Christoph Sebastian Traunsteiner

Vollständiger Abdruck der von der Fakultät für Physik der Technischen Universität München zur Erlangung des akademischen Grades eines

Doktors der Naturwissenschaften (Dr. rer. nat.)

genehmigten Dissertation.

Vorsitzende:	Prof. Dr. Nora Brambilla
Prüfer der Dissertation:	1. Prof. Dr. Julia Kunze-Liebhäuser
	2. Prof. Dr. Aliaksandr Bandarenka

Die Dissertation wurde am 13.06.2016 bei der Technischen Universität München eingereicht und durch die Fakultät für Physik am 14.09.2016 angenommen.

Contents

Abstract

Immobilization of laccase from *Trametes versicolor* (TvLc) on cathode surfaces in an orientation that enables direct electron transfer (DET) to the active center allows for exploitation of the enzyme's potential towards the oxygen reduction reaction (ORR) and for the study of its bioelectrocatalytic behavior.

In the first part of this work, TvLc is immobilized on mixed self-assembled monolayers (SAMs) on Au(111) consisting of a linker molecule, thiolated veratric acid (tVA) with a moiety similar to the enzyme's natural substrates, and a diluent molecule, 3-Mercaptopropionic acid (MPA). Electrochemical scanning tunneling microscopy (EC-STM) is used to determine the molecular arrangement of the two species that form the monolayer in two different SAMs and thus to prove the effect of linker separation on enzyme activity. Negligible enzymatic activity is found on a monolayer, where a close packing of tVA linkers is observed. Maximum catalytic currents are measured on a SAM, where tVA and MPA mix homogeneously. This shows that a certain distance between neighboring linkers is required for induced-fit binding of TvLc to the linker moiety, which leads to a proper enzyme orientation and allows for DET to the active center. Immobilized enzymes are studied with electrochemical atomic force microscopy (EC-AFM), EC-STM and scanning electrochemical potential microscopy (SECPM), a scanning probe technique for the detection of the electrical double-layer (EDL) potential, which previously showed high-resolution imaging capabilities of biomolecules. In this work, EC-STM and SECPM images show an unexpected degree of similarity. Differences between enzymatic activities measured here and literature data are explained with a model developed in the frame of this thesis that is based on results from EC-SPM, electrochemistry and electrochemical impedance spectroscopy (EIS).

The second part of this thesis consists of a mechanistic study of the working principle of the SECPM technique. The OH adsorbate structure formed on a Cu(111) WE in

alkaline solution is used as a model system and imaged with this method, revealing a structural parameter of (0.60 ± 0.04) nm in excellent agreement with that found with EC-STM. This is the first evidence of high-resolution imaging with SECPM. The origin of the potential signal measured with the SECPM probe is discussed taking into account leakage currents that have to be transported between tip and surface. Two different approaches are presented to measure these currents, the obtained values are similar to tunneling currents in EC-STM. At a probe position far away from the electrode surface, leakage currents are transported via faradaic reactions with the electrolyte. At close tip-surface distances corresponding to potential set-points typical for SECPM surface scans, the potential detected with the tip can be explained by tunneling currents. Thus, the SECPM imaging principle is similar to that of an EC-STM with feedback signal set to potential instead of current and cannot deliver information on the EDL potential.

Die Immobilisierung von *Trametes versicolor* Laccase (TvLc) auf Kathodenoberflächen in einer passenden Orientierung für direkten Elektronentransfer (DET) zum aktiven Zentrum ermöglicht es, das hohe Sauerstoff-Reduktionspotential des Enzyms zu nutzen und den bioelektrokatalytischen Prozess zu studieren.

Im ersten Teil dieser Arbeit wird TvLc auf gemischten selbstorganisierten Monoschichten (SAMs) auf Au(111) immobilisiert. Diese bestehen aus einem Linkermolekül, thiolierter Veratrinsäure (tVA) mit einer funktionellen Gruppe ähnlich dem natürlichen Enzymsubstrat und einem Separatormolekül, 3-Mercaptopropionsäure (MPA). Mittels elektrochemischer Rastertunnelmikroskopie (EC-STM) wird die molekulare Anordnung der beiden Spezies bestimmt, um damit den Effekt der Linker-Separation auf die Enzymaktivität nachzuweisen. Die Aktivität ist vernachlässigbar auf einer SAM mit einer dichten Anordnung von tVA-Linkern. Die höchsten katalytischen Ströme werden auf einer SAM gemessen, in welcher tVA und MPA homogen gemischt vorliegen. Dies zeigt, dass eine gewisse Distanz zwischen benachbarten Linkern nötig ist, um die Induced-Fit-Anbindung von TvLc an die funktionelle Gruppe des Linkers zu ermöglichen, wodurch das Enzym passend für DET zum aktiven Zentrum orientiert wird. Die immobilisierten Enzyme werden untersucht mittels elektrochemischer Rasterkraftmikroskopie, EC-STM und rasternder elektrochemischer Potentialmikroskopie (SECPM), einer Rastersondenmethode für die Messung des elektrochemischen Doppelschicht(EDL)-Potentials, mit welcher bereits Biomoleküle hochaufgelöst abgebildet werden konnten. Die in dieser Arbeit gemessenen EC-STM- und SECPM-Bilder zeigen dabei unerwartet starke Übereinstimmungen. Unterschiede zwischen den hier gemessenen Enzymaktivitäten und Literaturdaten werden mittels eines im Rahmen dieser Dissertation entwickelten Modells erklärt, welches auf EC-SPM-, Elektrochemie- und Elektrochemischer-Impedanzspektroskopie-Resultaten basiert.

Der zweite Teil besteht aus einer mechanistischen Studie des SECPM-Funktionsprinzips. Dafür wird die auf einer Cu(111)-Arbeitselektrode ausgebildete OH-Adsor-

batstruktur als Modellsystem studiert und mit dieser Methode abgebildet, wobei sich ein Strukturparameter von (0.60 ± 0.04) nm ergibt, in exzellenter Übereinstimmung mit EC-STM-Messungen. Dies stellt den ersten Nachweis der hochauflösenden Abbildungsfähigkeit des SECPM dar. Der Ursprung des von der SECPM-Sonde gemessenen Potentialsignals wird unter Einbeziehung von Leckströmen zwischen Spitze und Oberfläche diskutiert. Die mittels zweier unterschiedlicher Ansätze der Leckstrombestimmung erhaltenen Werte sind vergleichbar mit den Tunnelströmen im EC-STM. Bei einer Sondenposition weit weg von der Elektrodenoberfläche werden die Leckströme über faradaische Reaktionen mit dem Elektrolyten abtransportiert. Bei geringen Entfernungen zwischen Spitze und Oberfläche, entsprechend den typischen Potential-Sollwerten für SECPM-Oberflächenmessungen, kann das Potential an der Spitze mittels Tunnelströmen erklärt werden. Das heißt, das SECPM-Abbildungsprinzip ist vergleichbar mit dem eines EC-STM mit einem Potential-Feedback anstelle des Stromes. Es kann somit keine Informationen über das EDL-Potential liefern.

"*Don't keep forever on the public road, going only where others have gone, and following one after the other like a flock of sheep. Leave the beaten track occasionally and dive into the woods. Every time you do so you will be certain to find something that you have never seen before.*"

Alexander Graham Bell

1. Introduction

Probably the main challenge of mankind for the next decades is to deal with the dangers of climate change induced by anthropogenic greenhouse gas emissions. In order to limit global warming to 2 °C compared to pre-industrial levels,[1] the amount of greenhouse gases in the atmosphere has to stabilize below a 450 ppm CO_2-equivalent until the year 2100.[2] As a consequence, a drastic reduction of global greenhouse gas emissions of 40-70% until 2050 and close to zero until 2100 is necessary, compared to 2010 levels. This reduction can only be achieved by a series of measures starting from efficiency enhancements of present technologies to a full transition to emission-free technologies using renewable energy sources in all fields of energy conversion.

A promising technique especially in the field of electricity generation and transportation, and also for some niche applications, are fuel cells (FCs). Compared to internal combustion engines (ICE) with typical efficiencies of 20-40%, FCs can reach efficiencies of 40-60% and higher, depending on the size of the plant.[3] While in an ICE the fuel is mixed with the oxidant and brought to reaction, converting chemical to mechanical energy and optionally in an additional step to electricity, a FC converts chemical energy directly to electrical energy by separating the combustion of fuel and oxidant into two electrochemical reactions. In the following, the working principle shall be explained considering the example of a proton exchange membrane (PEM) FC, a low-temperature FC typically used in vehicular and portable applications. The eponymous polymer membrane separates anode and cathode side to avoid mixing of the two reacting species. The

fuel, in most cases hydrogen (H_2), methane, methanol or ethanol, ideally from renewable sources is oxidized at the three-phase boundary of anode, electrolyte and fuel, creating protons that permeate through the ion-conducting membrane to the cathode. At the cathode-electrolyte interface, atmospheric oxygen (O_2) is reduced to water (H_2O) by reacting with the protons that have been transported via the membrane and electrons that traveled along an external electric circuit. The theoretical maximum voltage obtainable from this arrangement is determined by the difference between the electrochemical potentials of cathode and anode reactions. In praxis, the voltage is reduced by overpotentials necessary to create finite reaction rates corresponding to a current output. In general, electrocatalysts like platinum (Pt) or Pt alloys are used to increase reaction rates and thus improve the non-linear current-voltage characteristics of a FC.

Especially the sluggish kinetics of the ORR at the cathode is a limiting factor for the efficiency of most low-temperature FCs. At present, high amounts of noble metals like Pt are required to operate a fuel cell at the necessary currents. This complicates large-scale production due to high costs and limited availability of raw materials. Current research is focusing on a reduction of Pt loading below $0.1\,\mathrm{mg\,cm^{-2}}$ (comparable to the amount of Pt in a present-day ICE vehicle) without loss of activity and durability,[4, 5] either by increasing the specific activity or by (partial) replacement of the noble metal.

For the development of improved catalysts it is import to gain a better understanding of the basic processes occurring during the electrochemical reaction. Taking a look at nature shows that some of the apparent limitations to inorganic catalysts have been overcome by enzymes. Two of these bio(electro)catalysts' outstanding properties have to be mentioned: specificity and activity. During millions of years of evolution some of them optimized the catalysis of a specific reaction resulting in reaction rates close to or sometimes overpassing the diffusion limit of reactants and products.[6] The specific (per reaction site) activity towards the ORR of some enzymes was found to be higher than for Pt based catalysts.[7–9] The second main advantage of enzymatic biocatalysts,

namely high specificity towards a single reaction pathway, helps to avoid side reactions. Furthermore, this allows to extend the range of fuels, if an enzyme can be found for the desired reaction. Examples include the oxidation of glucose[10], fructose[11, 12] and lactate[13]. If the enzyme used for the anode reaction is tolerant to the reactants and products of the cathode reaction and vice versa, the membrane can be omitted, which helps in the construction of miniaturized fuel cells.[14–16]

Nevertheless, enzymatic FCs have some drawbacks which limit an industrial application. Due to the large size of an enzyme compared to the reaction site of a (nanoparticular) inorganic catalyst, the density of active sites on a bioelectrode is low, resulting in lower current and power densities. Current research is trying to overcome this by using 3-dimensional high-surface area electrode structures like (carbon) nanotubes[17–19] or multilayer enzyme entrapment in redox hydrogels[7]. Issues include the electronic coupling of enzymes to the 3D electrode and mass transport of reactants and products to and from the bioelectrocatalyst, respectively.

More substantial is the limited range of temperature and pH, where enzymes are stable. This restricts the field of operation to an environment at or close to physiological conditions and renders enzymatic FCs less useful for automotive or large-scale energy conversion applications. Typical fields of application are sensors for glucose levels in the human body or powering of small implanted electronic devices like pacemakers or even electronic contact lenses.[20–22]

A different approach tries to make use of the fact that some enzymes can be regarded as performance benchmark for electrocatalysts. Their electrochemical potential is close to that of the catalyzed reaction, thus maximizing the efficiency of the reaction. A better understanding of the biocatalytic processes during the reaction can help in the development of improved inorganic catalysts that require less or no noble metals.[23, 24] Several Pt-free catalysts found in literature are based on or influenced by metallic active centers of enzymes.[25, 26]

Whether the goal is the construction of a high-performance enzymatic bioelectrode or a fundamental in-situ study of biocatalytic processes, it is necessary to achieve a stable enzyme immobilization on the electrode surface allowing for an efficient electron transfer to the enzyme's active center. During the last decades, there have been several breakthroughs in the development of enzymatic bioelectrodes.[27] Several approaches, especially those dealing with the cathode side, are based on an electrode surface modification with linker molecules exhibiting a moiety similar to the enzyme's natural substrate.[19, 28–30] Increased currents have been explained by free-standing linkers, that are accessible to the enzyme. If the enzyme can bind to the linker with its active center oriented towards the surface, electronic communication between electrode and enzymatic redox center can be established, resulting in enzymatic activity. Although this explanation is intuitively reasonable, a detailed molecular-level analysis of the interaction between enzyme and linkers on a functionalized electrode surface is still missing.

An instrument for the high-resolution investigation of flat surfaces was developed in 1982, the STM.[31] This technique uses an electronic tunneling current between an ultrasharp probe and an electrode to map electron densities on the electrode surface. Soon after its invention, it was shown that it is capable of atomic-resolution imaging of metallic and semi-metallic surfaces as well as organic monolayers on conducting surfaces in vacuum, ambient and liquid environment. Together with its sister technology, the AFM[32], which is based on the mechanical interaction between probe and sample, both techniques have been used for the study of enzyme coverages on various surfaces.

A more recent development following up the invention of the STM is the SECPM.[33] This instrument claims to fulfill the dream of many electrochemists, the direct measurement of the potential in the proximity of an electrode surface, in the EDL. The resulting possibility of contact-less surface mapping offers many advantages, e.g. in the field of bioelectrochemistry. It was shown that biomolecules can be imaged with this instrument with a resolution exceeding that of STM.[34] Submolecular features could be assigned to

enzyme components known from crystallographic data. This makes SECPM a promising technique for the direct local study of enzymatic properties impossible with previous technology.

The goal of this thesis is to gain a better understanding of the interaction between enzymes and functionalized electrode surfaces. Therefore, the influence of different molecular arrangements of electrode surfaces functionalized through coverage with mixed SAMs on the activity of immobilized enzymes is studied using electrochemistry and EC-SPM techniques. The results give valuable input for the development of improved biocathodes. EC-SPM investigations of enzyme covered electrode surfaces show an unexpected high degree of similarity between EC-STM and SECPM micrographs. This triggers a more intensive investigation of the SECPM working principle, supposedly detecting the EDL potential of an electrode. A Cu electrode is used as model surface for SECPM imaging aiming at a deeper understanding of the physical and electrochemical origin of the potential measured with this technology.

This thesis is structured into five chapters. After this introduction, chapter 2 explains the basic theories of interfacial physics, electrochemistry and bioelectrochemistry as well as the principles of electrochemical and electrochemical scanning probe techniques. In chapter 3, an overview of the chemicals and materials used in this work is given followed by a description of the preparation and realization of experiments. Chapter 4 is divided into two sections and deals with the obtained results and a critical discussion thereof. In section 4.1, the molecular arrangement of linkers in two different monolayers is resolved with EC-STM followed by electrochemical studies of enzymatic activity after immobilization of the biomolecules on these monolayers. Immobilized enzymes are further investigated with EC-STM, EC-AFM and SECPM. The results are used to estimate the ratio of active enzymes on the surface. Section 4.2 takes a closer look at the SECPM technique, presenting the first high-resolution images obtained with this instrument and

an examination of the working principle taking into account leakage currents present in the system. Finally, a summary and conclusions are given in chapter 5.

2. Fundamentals

This chapter gives an introduction to the theories describing processes at the electrode-solution interface and to techniques employed for its investigation. After a description of the EDL (section 2.1), electrochemical reactions in general and the ORR in particular are treated in section 2.2. Electrochemical methods and surfaces used in this work are described in sections 2.3 and 2.4, respectively. Section 2.5 introduces enzymatic bioelectrocatalysis and finally electrochemical scanning probe techniques are described in section 2.6. If not stated explicitly, the presentation in this chapter follows standard text books such as references [3, 35–37].

2.1. The solid-electrolyte interface

Electrochemical reactions take place at the electrode-electrolyte interface. Before electrode reactions can be studied, it is important to discuss the arrangement of ionic charge carriers in the solution close to the interface. The resulting parameters like charge and potential distribution can have a strong influence on the reaction.

At the beginning, it is convenient to define a Cartesian coordinate system that will be used in this work: the x and y axes describe positions on the electrode surface, the z axis is used to measure the orthogonal distance from the surface.

2.1.1. The Helmholtz model of the electrical double layer

When an electrode is immersed into an electrolyte, the charge q on its surface A is counterbalanced by solvated ions in solution carrying the opposite charge. The simplest model for the arrangement of ions in the EDL has been proposed by Helmholtz in 1879.[38] He suggested that the surface charge σ is compensated by one layer of solvated ions at a close distance z_{OHP} from the surface, similar to a parallel plate capacitor. This compact ion layer is nowadays referred to as outer Helmholtz plane (OHP) and z_{OHP} corresponds to the radius of the ions including their solvation shell. In analogy to a parallel plate capacitor, σ can be calculated via

$$\sigma = \frac{q}{A} = \frac{\varepsilon\varepsilon_0 E}{z_{\mathrm{OHP}}}, \tag{2.1}$$

where according to electrochemical conventions the electric potential is called E, ε_0 is the vacuum permittivity and ε is the permittivity of the electrolyte in the region between the electrode surface and the OHP.

An important quantity in electrochemistry is the differential capacitance C_{D} of the EDL, defined as

$$C_{\mathrm{D}} = \left.\frac{\mathrm{d}\sigma}{\mathrm{d}E}\right|_{z=0}. \tag{2.2}$$

For the Helmholtz model, (2.2) yields

$$C_{\mathrm{D,H}} = \frac{\mathrm{d}}{\mathrm{d}E}\left(\varepsilon\varepsilon_0\frac{E}{z_{\mathrm{OHP}}}\right)\bigg|_{z=0} = \frac{\varepsilon\varepsilon_0}{z_{\mathrm{OHP}}}. \tag{2.3}$$

Thus, a constant $C_{\mathrm{D,H}}$ is predicted by this model.

As z_{OHP} corresponds to the closest distance the electrode can be approached by the center of charge of solvated ions, the volume between the electrode surface and the OHP is considered free of charge. The behavior of the electric potential normal to the surface $E(z)$ between the potential of the electrode E_{WE} and the potential of the bulk electrolyte

E_{bulk} can be calculated from the one-dimensional Poisson equation:

$$\frac{\mathrm{d}^2 E(z)}{\mathrm{d}z^2} = -\frac{\rho}{\varepsilon\varepsilon_0}, \tag{2.4}$$

where ρ is the electric charge density. From $\rho = 0$ follows that $\frac{\mathrm{d}E(z)}{\mathrm{d}z} = const.$ Rearranging and integrating yields

$$\int_{E_{\text{WE}}}^{E} \mathrm{d}E' = \int_{0}^{z} \text{const.}\, \mathrm{d}z', \tag{2.5}$$

which results in

$$E(z) = E_{\text{WE}} - \frac{E_{\text{WE}}}{z_{\text{OHP}}} \cdot z. \tag{2.6}$$

For the last step, the boundary condition $E(0) = E_{\text{WE}}$ is used and, without loss of generality, $E(z_{\text{OHP}}) = E_{\text{bulk}} = 0$ is assumed. Hence, a linear potential behavior is predicted by the Helmholtz model.

This model yields the right order of magnitude for the C_{D}, but it is not suitable for explaining some experimental observations like a dependency of the capacitance on electrolyte concentration, on the potential applied to the electrode and on temperature, i.e. thermal movement of the ions.

2.1.2. The Gouy-Chapman theory

Gouy[39] and Chapman[40] used a more realistic approach to describe the distribution of solvated ions i in an electrostatic potential $E(\boldsymbol{x})$ by Boltzmann statistics:

$$\mathfrak{n}_i(\boldsymbol{x}) = \mathfrak{n}_i^0 \exp \frac{-\mathfrak{z}_i e E(\boldsymbol{x})}{k_{\text{B}} T}, \tag{2.7}$$

where $\mathfrak{n}_i(\boldsymbol{x})$ is the number density and $\mathfrak{z}_i$ the charge number of ion i at position $\boldsymbol{x}$, e is the elementary charge and T the thermodynamic or absolute temperature. The charge

density $\rho(\boldsymbol{x})$ corresponding to the distribution of ions described by equation (2.7) is

$$\rho(\boldsymbol{x}) = \sum_i \mathfrak{n}_i(\boldsymbol{x})\mathfrak{z}_i e = \sum_i \mathfrak{n}_i^0 \mathfrak{z}_i e \exp \frac{-\mathfrak{z}_i e E(\boldsymbol{x})}{k_\mathrm{B} T}. \tag{2.8}$$

To obtain the relation between charge density and electric field perpendicular to a planar electrode, the one-dimensional Poisson equation (2.4) is used. Inserting (2.8) into (2.4) results in the Poisson-Boltzmann equation:

$$\frac{\mathrm{d}^2 E(z)}{\mathrm{d}z^2} = -\frac{e}{\varepsilon\varepsilon_0} \sum_i \mathfrak{n}_i^0 \mathfrak{z}_i \exp \frac{-\mathfrak{z}_i e E(z)}{k_\mathrm{B} T}. \tag{2.9}$$

Using the identity $\frac{\mathrm{d}^2 E(z)}{\mathrm{d}z^2} = \frac{1}{2}\frac{\mathrm{d}}{\mathrm{d}E}\left(\frac{\mathrm{d}E(z)}{\mathrm{d}z}\right)^2$ and rearranging leads to

$$\mathrm{d}\left(\frac{\mathrm{d}E(z)}{\mathrm{d}z}\right)^2 = -\frac{2e}{\varepsilon\varepsilon_0} \sum_i \mathfrak{n}_i^0 \mathfrak{z}_i \exp \frac{-\mathfrak{z}_i e E(z)}{k_\mathrm{B} T}\, \mathrm{d}E, \tag{2.10}$$

which can be integrated to

$$\left(\frac{\mathrm{d}E(z)}{\mathrm{d}z}\right)^2 = \frac{2k_\mathrm{B} T}{\varepsilon\varepsilon_0} \sum_i \mathfrak{n}_i^0 \exp \frac{-\mathfrak{z}_i e E(z)}{k_\mathrm{B} T} + \text{const.} \tag{2.11}$$

The constant term in (2.11) is found using the boundary conditions $\frac{\mathrm{d}E(z)}{\mathrm{d}z} \to 0$ and $E(z) \to 0$ for $z \to \infty$:

$$\left(\frac{\mathrm{d}E(z)}{\mathrm{d}z}\right)^2 = \frac{2k_\mathrm{B} T}{\varepsilon\varepsilon_0} \sum_i \mathfrak{n}_i^0 \left(\exp \frac{-\mathfrak{z}_i e E(z)}{k_\mathrm{B} T} - 1\right). \tag{2.12}$$

For a symmetrical electrolyte like NaOH in aqueous solution, $\mathfrak{z}_1 = -\mathfrak{z}_2 = \mathfrak{z}$ and $\mathfrak{n}_1^0 = \mathfrak{n}_2^0 = \mathfrak{n}^0$, thus

$$\frac{\mathrm{d}E(z)}{\mathrm{d}z} = -\sqrt{\frac{8k_\mathrm{B} T \mathfrak{n}^0}{\varepsilon\varepsilon_0}} \sinh \frac{\mathfrak{z} e E(z)}{2k_\mathrm{B} T}. \tag{2.13}$$

Rearranging and integrating leads to

$$\int_{E_{\mathrm{WE}}}^{E} \frac{\mathrm{d}E'}{\sinh \frac{2eE'(z)}{2k_{\mathrm{B}}T}} = -\sqrt{\frac{8k_{\mathrm{B}}T\mathfrak{n}^0}{\varepsilon\varepsilon_0}} \int_0^z \mathrm{d}z' \tag{2.14}$$

The result of the integration is:

$$\frac{2k_{\mathrm{B}}T}{\mathfrak{z}e} \log \frac{\tanh \frac{\mathfrak{z}eE(z)}{4k_{\mathrm{B}}T}}{\tanh \frac{\mathfrak{z}eE_{WE}}{4k_{\mathrm{B}}T}} = -\sqrt{\frac{8k_{\mathrm{B}}T\mathfrak{n}^0}{\varepsilon\varepsilon_0}} \cdot z \tag{2.15}$$

or

$$\frac{\tanh \frac{\mathfrak{z}eE(z)}{4k_{\mathrm{B}}T}}{\tanh \frac{\mathfrak{z}eE_{WE}}{4k_{\mathrm{B}}T}} = \exp(-\kappa z). \tag{2.16}$$

In the last step, the characteristic Debye length

$$\lambda_{\mathrm{D}} = \frac{1}{\kappa} = \sqrt{\frac{\varepsilon\varepsilon_0 k_{\mathrm{B}}T}{2\mathfrak{z}^2 e^2 \mathfrak{n}^0}} \tag{2.17}$$

has been introduced, defined by the distance where the potential drops to $\frac{1}{\mathrm{e}}$ of its initial value. For a monovalent symmetric electrolyte like NaOH at a concentration of 0.1 M at room temperature (20 °C), $\lambda_{\mathrm{D}} = 0.96\,\mathrm{nm}$. To further simplify (2.16), the approximation $\tanh(x) \approx x$ is used, which is valid for $x \lesssim 0.5$. At room temperature $\frac{4k_{\mathrm{B}}T}{e} = 0.1\,\mathrm{V}$. Thus, for $E(z) < 50\,\mathrm{mV}$, (2.16) can be approximated for a monovalent electrolyte by

$$E(z) = const.\,\mathrm{e}^{-\kappa \cdot z}\,. \tag{2.18}$$

Hence, the potential drop in the double layer predicted by this theory is exponential.

In order to obtain the differential capacitance of the EDL in the Gouy-Chapman model, the surface charge on the electrode is determined using Gauss's law:

$$\frac{q}{\varepsilon\varepsilon_0} = \oint_{\mathrm{A}} \mathfrak{E}\,\mathrm{d}\boldsymbol{S}. \tag{2.19}$$

According to (2.19), the charge q contained in an arbitrarily chosen volume is equal to the integral over the electric field $\mathfrak{E}$ passing through the enclosing surface S. The volume can be chosen as a cuboid with its front face A parallel to the electrode surface and in the interface between electrode and electrolyte and the back face located far enough in the electrolyte, where $\mathfrak{E} = \frac{\mathrm{d}E}{\mathrm{d}z} = 0$. The side surfaces of the cuboid are parallel to $\mathfrak{E}$, hence $\mathfrak{E}\,\mathrm{d}\boldsymbol{S} \neq 0$ only in the interface, where $\mathfrak{E} \parallel \mathrm{d}\boldsymbol{A}$. Then, (2.19) simplifies to:

$$\frac{q}{\varepsilon\varepsilon_0} = \int \frac{\mathrm{d}E(z)}{\mathrm{d}z}\Big|_{z=0} \mathrm{d}A = A\,\frac{\mathrm{d}E(z)}{\mathrm{d}z}\Big|_{z=0}. \tag{2.20}$$

Inserting $\frac{\mathrm{d}E(z)}{\mathrm{d}z}$ from (2.13) results in

$$\sigma = \frac{q}{A} = -\sqrt{8k_\mathrm{B}T\mathfrak{n}^0\varepsilon\varepsilon_0}\,\sinh\frac{\mathfrak{z}eE_{WE}}{2k_\mathrm{B}T}, \tag{2.21}$$

where $E(z = 0) = E_\mathrm{WE}$ is the potential applied to the electrode. From (2.21), the differential capacitance according to the Gouy-Chapman theory can be obtained:

$$C_\mathrm{D,GC} = \frac{\mathrm{d}\sigma}{\mathrm{d}E_\mathrm{WE}} = -\sqrt{\frac{2\mathfrak{z}^2e^2\mathfrak{n}^0\varepsilon\varepsilon_0}{k_\mathrm{B}T}}\,\cosh\frac{\mathfrak{z}eE_\mathrm{WE}}{2k_\mathrm{B}T}. \tag{2.22}$$

The Gouy-Chapman model introduces a dependency of $E(z)$ and C_D on electrolyte concentration, temperature and electrode potential and manages to describe the correct trend when these parameters are changed. Especially a C_D minimum at potentials close to the potential of zero charge E_PZC, which is observed under certain experimental conditions, can be described by the cosh function in (2.22). However, the capacitances and potentials resulting from the Gouy-Chapman theory are generally higher than experimental values. The main drawback of the Gouy-Chapman theory is its treatment of the solvated ions as pointlike particles, which allows for their unrestricted approach towards the electrode surface resulting in a divergent behavior of $E(z)$ and C_D.

2.1.3. Stern's modification

The description of the EDL proposed by Stern in 1924[41] is a combination of the Helmholtz and the Gouy-Chapman model, which is nowadays referred to as Gouy-Chapman-Stern (GCS) theory. The arrangement of ions in the electrolyte follows the Poisson-Boltzmann equation, but their closest approach to the electrode surface is limited by their ionic radius including the solvation shell. The result is a first compact layer of ions in the outer Helmholtz plane followed by a diffuse layer between the OHP and the bulk electrolyte as described by the Gouy-Chapman theory (see Figure 2.1A). The potential between the electrode and the compact layer is obtained from (2.5) using the boundary conditions $E(0) = E_{\mathrm{WE}}$ and $E(z_{\mathrm{OHP}}) = E_{\mathrm{OHP}}$:

$$E(z) = E_{\mathrm{WE}} - \frac{E_{\mathrm{WE}} - E_{\mathrm{OHP}}}{z_{\mathrm{OHP}}} \cdot z \qquad \text{for } 0 < z < z_{\mathrm{OHP}}. \tag{2.23}$$

In the diffuse layer, the potential is described by the Gouy-Chapman theory according to (2.18) using the boundary condition $E(z_{\mathrm{OHP}}) = E_{\mathrm{OHP}}$

$$E(z) = E_{\mathrm{OHP}} \cdot \mathrm{e}^{-\kappa \cdot (z - z_{\mathrm{OHP}})} \qquad \text{for } z > z_{\mathrm{OHP}}. \tag{2.24}$$

Hence, the potential drops linearly from E_{WE} to E_{OHP} between $z = 0$ and z_{OHP}, followed by an exponential decrease to $E = 0$ in the bulk electrolyte (see Figure 2.1C).

According to the Stern model, C_{D} can be treated as a series connection of a Helmholtz capacitance and a Gouy-Chapman capacitance:

$$\frac{1}{C_{\mathrm{D}}} = \frac{1}{C_{\mathrm{D,H}}} + \frac{1}{C_{\mathrm{D,GC}}}, \tag{2.25}$$

where $C_{\mathrm{D,H}}$ and $C_{\mathrm{D,GC}}$ are defined via (2.3) and (2.22). This treatment retains the potential dependency of C_{D} according to the Gouy-Chapman theory while preventing any divergent behavior by including the $C_{\mathrm{D,H}}$ term.

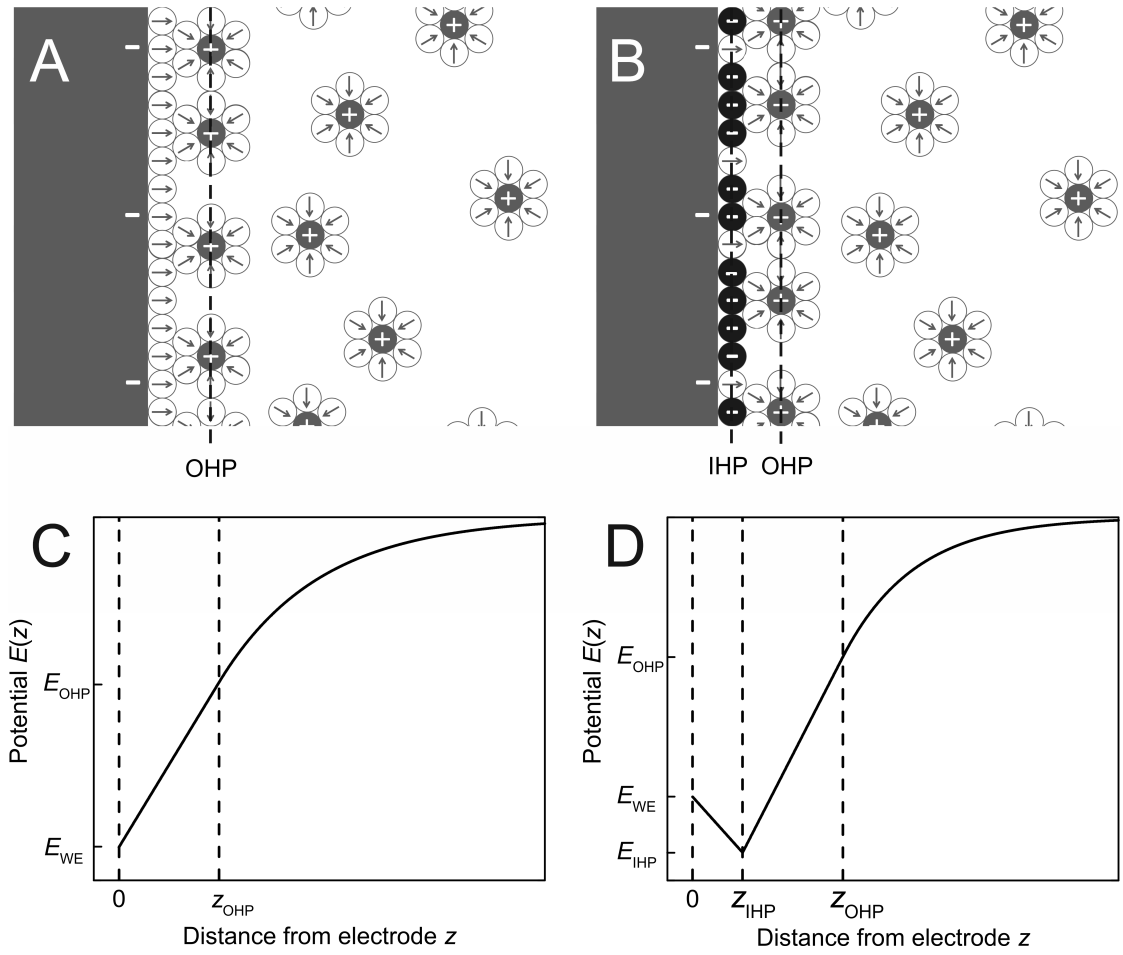

Figure 2.1.: Schematic of the electrochemical double layer according to the Gouy-Chapman-Stern theory in the A) absence and B) presence of specifically adsorbed ions. Diagrams in C) and D) depict the double layer potentials in A) and B).

2.1.4. Specific adsorption

So far, only solvated ions moving freely in the electrolyte have been considered. In case of a strong chemical interaction between ions and electrode, they can lose their solvation shell and form an additional layer between electrode surface and OHP, called inner Helmholtz plane (IHP) (see Figure 2.1B).[42] This effect is called specific adsorption. Considering the charge of the specifically adsorbed ions as being located in the IHP, the volume between electrode surface and IHP and between the IHP and the OHP is free of charge. Thus, following the same argument as for the Helmholtz model, the potential behavior in these two regions is linear:

$$E(z) = E_{\mathrm{WE}} - \frac{E_{\mathrm{WE}} - E_{\mathrm{IHP}}}{z_{\mathrm{IHP}}} \cdot z \qquad \text{for} \quad 0 < z < z_{\mathrm{IHP}} \tag{2.26}$$

$$E(z) = E_{\mathrm{IHP}} - \frac{E_{\mathrm{IHP}} - E_{\mathrm{OHP}}}{z_{\mathrm{OHP}} - z_{\mathrm{IHP}}} \cdot (z - z_{\mathrm{IHP}}) \qquad \text{for} \quad z_{\mathrm{IHP}} < z < z_{\mathrm{OHP}} \tag{2.27}$$

followed by an exponential decrease between the OHP and the bulk electrolyte according to (2.24) (see Figure 2.1D).

There are further theories taking into account additional details like a variation of the electrolyte permittivity due to molecular orientation in the Helmholtz layers.[43] These models will not be taken into account explicitly in this work.

2.2. Electrochemical reactions

In this section, the theoretical background of interfacial electrochemistry will be presented. In order for an electrochemical reaction to proceed, electrons have to be transported from the inside of the electrode to the interface (or vice versa), where their reaction with species in the electrolyte solution takes place.

2.2.1. Thermodynamics and potentials of electrochemical reactions

In the following, a general electrochemical reaction in equilibrium taking place at the interface between an electronic conductive phase I (e.g. a solid electrode) and an ionic conductive phase II (e.g. an electrolyte) is considered:

$$\sum_{\mathrm{Ox}} \nu_{\mathrm{Ox}}\,\mathrm{Ox}^{\mathfrak{z}_{\mathrm{Ox}}} + n\,\mathrm{e}^- \rightleftarrows \sum_{\mathrm{Red}} \nu_{\mathrm{Red}}\,\mathrm{Red}^{\mathfrak{z}_{\mathrm{Red}}}, \tag{2.28}$$

i.e. the oxidized forms of species Ox with charge number $\mathfrak{z}_{\mathrm{Ox}}$ change to their reduced forms Red with charge number $\mathfrak{z}_{\mathrm{Red}}$ by accepting n electrons from the electrode. ν_i is the stoichiometric number of species i. Equation (2.28) is called a half-cell reaction, as the free electrons and ions have to be supplied/consumed by a second electrochemical (half-cell) reaction connected to the first cell in order to close the electric circuit. Currents originating from the reduction or oxidation of a substance at an electrode surface are also known as faradaic currents.

The electrochemical equilibrium between the two states of a species in phase I and II is described by

$$\bar{\mu}_i(\mathrm{I}) = \bar{\mu}_i(\mathrm{II}), \tag{2.29}$$

where $\bar{\mu}_i = \left.\frac{\partial G}{\partial n_i}\right|_{T,p,n_j\neq n_i}$ is the electrochemical potential of species i in phase I or II, G is the Gibbs (free) energy, n_i is the amount of substance i and p the pressure. $\bar{\mu}_i = \mu_i + \mathfrak{z}_i F E^0$ differs from the chemical potential $\mu_i = \mu_i^0 + RT\log a_i$ by the electric energy per mole $\mathfrak{z}_i F E^0(\mathrm{I/II})$, where $E^0(\mathrm{I/II})$ is the inner or Galvani potential in phase I or II. μ_i^0 is the standard chemical potential, F and R are the Faraday and the gas constant and a_i is the activity of species i. For (2.28), one obtains

$$\sum_{\mathrm{Ox}} \nu_{\mathrm{Ox}}\bar{\mu}_{\mathrm{Ox}} + n\bar{\mu}_{\mathrm{e}} = \sum_{\mathrm{Red}} \nu_{\mathrm{Red}}\bar{\mu}_{\mathrm{Red}} \tag{2.30}$$

or

$$\sum_{\mathrm{Ox}} \nu_{\mathrm{Ox}} \mu^0_{\mathrm{Ox}} + RT \log \prod_{\mathrm{Ox}} a^{\nu_{\mathrm{Ox}}}_{\mathrm{Ox}} + \sum_{\mathrm{Ox}} \nu_{\mathrm{Ox}} \mathfrak{z}_{\mathrm{Ox}} F E^0(\mathrm{II}) + n\mu^0_{\mathrm{e}} - nFE^0(\mathrm{I}) = \sum_{\mathrm{Red}} \nu_{\mathrm{Red}} \mu^0_{\mathrm{Red}} + RT \log \prod_{\mathrm{Red}} a^{\nu_{\mathrm{Red}}}_{\mathrm{Red}} + \sum_{\mathrm{Red}} \nu_{\mathrm{Red}} \mathfrak{z}_{\mathrm{Red}} F E^0(\mathrm{II}). \tag{2.31}$$

Solving for the potential and keeping in mind that $\sum_{\mathrm{Ox}} \nu_{\mathrm{Ox}} \mathfrak{z}_{\mathrm{Ox}} - \sum_{\mathrm{Red}} \nu_{\mathrm{Red}} \mathfrak{z}_{\mathrm{Red}} = n$ results in

$$\begin{aligned} \Delta E^0 &= \frac{\sum_{\mathrm{Ox}} \nu_{\mathrm{Ox}} \mu^0_{\mathrm{Ox}} + n\mu^0_{\mathrm{e}} - \sum_{\mathrm{Red}} \nu_{\mathrm{Red}} \mu^0_{\mathrm{Red}}}{nF} + \frac{RT}{nF} \log \frac{\prod_{\mathrm{Ox}} a^{\nu_{\mathrm{Ox}}}_{\mathrm{Ox}}}{\prod_{\mathrm{Red}} a^{\nu_{\mathrm{Red}}}_{\mathrm{Red}}} \\ &= \Delta E^{00} + \frac{RT}{nF} \log \frac{\prod_{\mathrm{Ox}} a^{\nu_{\mathrm{Ox}}}_{\mathrm{Ox}}}{\prod_{\mathrm{Red}} a^{\nu_{\mathrm{Red}}}_{\mathrm{Red}}}, \end{aligned} \tag{2.32}$$

where the equilibrium or redox potential $\Delta E^0 = E^0(\mathrm{I}) - E^0(\mathrm{II})$ is the difference between the inner potentials of electrode and electrolyte and constant terms have been collected in the standard potential ΔE^{00} of the reaction. Equation (2.32) is the so-called Nernst equation. The potential of an electrochemical reaction taking place at the solid-liquid interface is not accessible by experiment as it is not possible to directly determine the electrolyte potential: such a measurement requires the immersion of a second electrode in the liquid creating an additional interface with another redox potential that has to be taken into account. To overcome this limitation, potentials in electrochemistry are measured against the potential of a reference electrode (RE), where a known reaction takes place, thus avoiding $E_{\mathrm{electrolyte}}$:

$$\begin{aligned} \Delta E^0 - \Delta E^0_{\mathrm{RE}} &= E^0_{\mathrm{electrode}} - E^0_{\mathrm{electrolyte}} - E^0_{\mathrm{RE}} + E^0_{\mathrm{electrolyte}} \\ &= E^0_{\mathrm{electrode}} - E^0_{\mathrm{RE}}. \end{aligned} \tag{2.33}$$

By convention, the standard potential of the hydrogen reaction

$$2\mathrm{H}^+(\mathrm{aq}) + 2\,\mathrm{e}^- \rightleftarrows \mathrm{H}_2 \tag{2.34}$$

is defined as $E^{00} \equiv 0\,\mathrm{V}$. This potential is experimentally available at the standard hydrogen electrode (SHE), where reaction (2.34) takes place under standard conditions ($T = 298\,\mathrm{K}$, $p = 101.3\,\mathrm{kPa}$, $a_\mathrm{i} = 1\ \forall\, i$), hence $E^0 = E^{00}$. All potentials E in this work are given versus SHE, so the Nernst equation (2.32) can be written as

$$E^0 = E^{00} + \frac{RT}{nF} \log \frac{\prod_\mathrm{Ox} a_\mathrm{Ox}^{\nu_\mathrm{Ox}}}{\prod_\mathrm{Red} a_\mathrm{Red}^{\nu_\mathrm{Red}}}. \tag{2.35}$$

2.2.2. Kinetics of electrochemical reactions

So far, electrochemical reactions in dynamic equilibrium have been considered, i.e. a situation where the rate or current of forward and back reaction are equal. In this subsection, the effect of non-equilibrium potentials on current will be treated.

2.2.2.1. Transition state theory

In 1889, Arrhenius found an exponential correlation between the temperature and the rate constant k of a chemical reaction:

$$k = A' \exp\left(-\frac{U_\mathrm{A}}{k_\mathrm{B} T}\right), \tag{2.36}$$

where U_A was termed activation energy of the reaction and A' was called frequency factor (nowadays pre-exponential factor). Only 46 years later and through the contribution of several others, Eyring developed the transition state theory (TST), which could finally explain the meaning of U_A and A'.[44] According to the TST, a chemical reaction proceeds along the reaction coordinate, an abstract one-dimensional parameter. The reaction coordinate is usually related to geometrical parameters like e.g. bond lengths that

change during the reaction and can thus be used to continuously describe the process from reactant to product states. As reactants and products are stable, they both exhibit a minimum on the potential energy surface. During the reaction from one minimum to the other, a local maximum in potential energy has to be overcome, which is assigned to a so-called transition state or activated complex represented by the double-dagger (‡) symbol. This transition state is usually located at or near a saddle point on the potential energy surface. The difference between the potential energies of transition state and reactant, i.e. the energy barrier that has to be overcome for the reaction to proceed, is the activation energy U_A in (2.36).

For a solution phase reaction under laboratory conditions, ΔpV is negligible. Thus, differences in internal energy ΔU can be expressed via changes in enthalpy $\Delta H = \Delta G + T\Delta S$, where S is the entropy. With this, (2.36) can be rewritten as

$$k = A' \exp\left(-\frac{\Delta H^\ddagger}{k_\mathrm{B}T}\right) = A' \exp\left(-\frac{\Delta G^\ddagger}{k_\mathrm{B}T}\right) \exp\left(-\frac{\Delta S^\ddagger}{k_\mathrm{B}}\right) = A \exp\left(-\frac{\Delta G^\ddagger}{k_\mathrm{B}T}\right). \quad (2.37)$$

In the last step, all temperature independent terms have been collected in A. As the internal energies of reactant and product are different in general, also the Gibbs energy of activation $\Delta G^\ddagger$ is different for the forward ($\Delta G^\ddagger_\mathrm{r}$) and back ($\Delta G^\ddagger_\mathrm{p}$) reaction (see Figure 2.2).

2.2.2.2. Marcus theory

Electrochemical reactions can be categorized in inner sphere (IS) and outer sphere (OS) reactions. IS reactions involve a strong, usually specific interaction between the reacting species and the electrode. This leads to changes in bond lengths of the participating compounds and their tightly bound solvation shell and/or the breaking and formation of bonds during the reaction. During an OS reaction, there is only a weak interaction with the electrode. The main reaction is an electron transfer from the electrode to

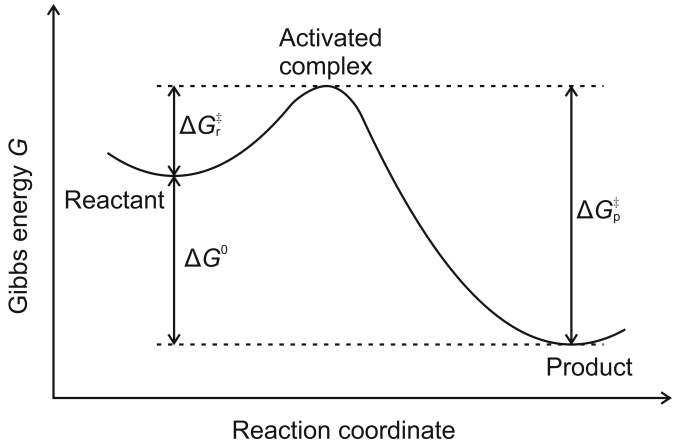

Figure 2.2.: Progress of a chemical reaction along the reaction coordinate according to the transition state theory. In order for the reactant to proceed to the product state, it has to overcome an activation barrier $\Delta G_r^{\ddagger}$. The Gibbs energy of reaction is indicated as ΔG^0.

the reactant, or vice versa, leading to changes in the outer, loosely bound solvation molecules. According to the Franck-Condon principle, electronic changes occur on a much faster timescale than nuclear changes. Hence, there is no variation in nuclear coordinates that could be chosen as reaction coordinate during the electron transfer, it is assumed to happen instantaneously. Additionally, charge cannot be transferred in arbitrary amounts, only as whole electrons, i.e. due to its quantized nature it is not appropriate as a direct measure of the continuous reaction pathway.

Still, the rate constant behavior observed for OS electrochemical reactions shows an exponential behavior according to the Arrhenius equation (2.37). This implies the existence of an activation barrier $G^{\ddagger}$ between the reactant and product states, which has to be overcome along a reaction pathway in order for the reaction to proceed.

Marcus was the first to discover a parameter that can be used as reaction coordinate by finding a reversible path to this intermediate state.[45] As the charge distributions of reactant and product states are different (an electron has been transferred during the reaction), also the polarization of the solvent is different before and after the reaction.

Due to the different timescales, changes in solvent polarization can be separated in those originating from the electron transfer and those coming from the atomic reorganization. Marcus first treated the electron polarization with a macroscopic model, where an arbitrary amount of charge Δe can be transferred between two spheres with radius r_1 and r_2 in a solvent. The Gibbs energy of polarization for this system is:

$$G = \left(\frac{1}{2r_1} + \frac{1}{2r_2} - \frac{1}{R}\right)\left(\frac{1}{\varepsilon_\infty} - \frac{1}{\varepsilon_0}\right)(\Delta e)^2, \tag{2.38}$$

where R is the distance between the two spheres and the solvent is described by the optical (high frequency) and static dielectric constants (permittivity) ε_∞ and ε_0. For a microscopic electrode reaction, the expression is

$$G = \left(\frac{1}{r} - \frac{1}{R}\right)\left(\frac{1}{\varepsilon_\infty} - \frac{1}{\varepsilon_0}\right)(\Delta e)^2, \tag{2.39}$$

where the reactant is treated as a sphere with radius r and R is the distance between the reactant and its image charge in the electrode.

According to the quadratic dependency of G on the transferred charge Δe in (2.39), the Gibbs energy of reactant $G_r(P)$ and product $G_p(P)$ in a one-electron reaction can be described as

$$G_\mathrm{r}(\Delta e) = a(\Delta e)^2 \tag{2.40a}$$

$$G_\mathrm{p}(\Delta e) = a(\Delta e - 1)^2 + \Delta G^0, \tag{2.40b}$$

where ΔG^0 is the change in Gibbs energy from reactant to product (see Figure 2.3) and the same coefficient a for both curves (see (2.39)). In this system, the transferred charge is limited to whole elementary charges, but the solvent polarization is not subject to this restriction. The position of the point of intersection between the two curves $\Delta e^\ddagger$, i.e. the position of the maximum in Gibbs energy, is found by setting $G_\mathrm{r}(\Delta e^\ddagger) = G_\mathrm{p}(\Delta e^\ddagger)$.

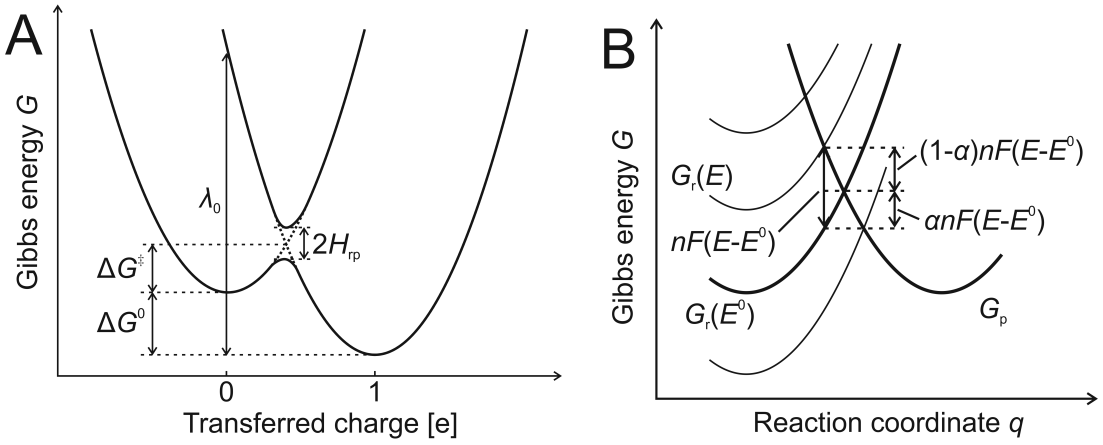

Figure 2.3.: A) Gibbs energies of reactant and product state according to Marcus theory. B) Close up of the intersection point between the two Gibbs functions shown in A). The influence of the applied potential on the symmetry factor α is depicted.

Inserting $\Delta e^{\ddagger}$ in (2.40a) results in

$$\Delta G^{\ddagger} = \frac{(\lambda_{\mathrm{o}} + \Delta G^{0})^{2}}{4\lambda_{\mathrm{o}}}, \tag{2.41}$$

where the outer reorganization energy λ_{o} is defined as

$$\lambda_{\mathrm{o}} = G_{\mathrm{p}}(0) - G_{\mathrm{p}}(\Delta e) = a(\Delta e)^{2} \tag{2.42}$$

(see Figure 2.3A). It represents the energy necessary to transform the solvent configuration from the reactant to the product state.

During the reaction, at least one ligand is shared between reactant species and electrode. The ion-ligand vibrations can be approximated as harmonic oscillations, giving a quadratic dependency of the potential energy on the displacement along a normal coordinate q for reactant and product species. Treating the resulting energy curves in a way similar to the solvent polarization as outlined above, leads to an inner reorganiza-

tion energy λ_i. As outer and inner reorganization energies are independent, they can be summed up to $\lambda = \lambda_\mathrm{i} + \lambda_\mathrm{o}$.

The probability of charge transfer between reactants and electrode at the intersection point between the two Gibbs functions is a function of the matrix element H_rp coupling reactant and product states (see Figure 2.3A). The current density for the reaction from reactant to product is

$$j_\mathrm{rp} = j_0(H_\mathrm{rp}) \exp\left(-\frac{\Delta G^\ddagger}{RT}\right) = j_0(H_\mathrm{rp}) \exp\left(-\frac{(\Delta G^0 + \lambda)^2}{4\lambda RT}\right), \tag{2.43}$$

where the temperature independent terms have been collected in the H_rp dependent exchange current density $j_0(H_\mathrm{rp})$. For an electrode reaction, $\Delta G^0 = F(E - E^0) = F\eta$, where the overpotential $\eta = E - E^0$ is introduced. The effect on the current density (2.43) is

$$j_\mathrm{rp} = j_0(H_\mathrm{rp}) \exp\left(-\frac{(\lambda + F\eta)^2}{4\lambda RT}\right) \tag{2.44}$$

Taking into account the current density of the back reaction $j_\mathrm{pr} = -j_0(H_\mathrm{rp}) \exp\left(-\frac{(\lambda - F\eta)^2}{4\lambda RT}\right)$, which is deduced similarly to the forward reaction, the net current density for the reaction becomes

$$j = j_\mathrm{rp} + j_\mathrm{pr} = j_0 \left(\exp\left(-\frac{(\lambda + F\eta)^2}{4\lambda RT}\right) - \exp\left(-\frac{(\lambda - F\eta)^2}{4\lambda RT}\right)\right), \tag{2.45}$$

which is called the Butler-Volmer-Marcus equation. From (2.45) it can be seen that non-zero net current densities are only obtained for $\eta \neq 0$. Under typical experimental conditions, the current density is limited by diffusion of reactants to the electrode before the quadratic term in the exponents in (2.45) shows an effect at higher overpotentials. Hence, for most cases, the exponent can be linearized assuming $\eta \ll \frac{F}{\lambda}$, which leads to

$$(\lambda \pm F\eta)^2 = \lambda^2 \pm 2\lambda F\eta + (F\eta)^2 \approx \lambda^2 \pm 2\lambda F\eta. \tag{2.46}$$

Thus, (2.45) simplifies to

$$j = j_0 \left(\exp\left(-\frac{\lambda + 2F\eta}{4RT} \right) - \exp\left(-\frac{\lambda - 2F\eta}{4RT} \right) \right). \tag{2.47}$$

This is a variant of the so-called Butler-Volmer equation[46, 47]

$$j = j_0 \left(\exp\left(\frac{\alpha F\eta}{RT} \right) - \exp\left(-\frac{(1-\alpha)F\eta}{RT} \right) \right), \tag{2.48}$$

where α is the so-called charge transfer coefficient or symmetry factor. A comparison of (2.47) and (2.48) shows that $\alpha = \frac{1}{2} + \frac{\lambda}{4F\eta}$. The meaning of α can be seen in Figure 2.3B at the crossing of G_r and G_p. At E^0, $\Delta G^0 = 0$, the two curves are symmetric. Applying a small overpotential η to the electrode changes G_r by $F\eta$. This results in a change of $\Delta G^\ddagger$ by $\frac{1}{2}F\eta$, hence, $\alpha = \frac{1}{2}$. If $\Delta G^0 < 0$ ($G_\mathrm{r}(0) > G_\mathrm{p}(1)$), G_r proceeds flatter and G_p runs steeper, thus $\alpha < \frac{1}{2}$. Similarly, $\alpha > \frac{1}{2}$ for $\Delta G^0 > 0$. In general, the charge transfer coefficient is limited to $0 < \alpha < 1$.

The Butler-Volmer equation (2.48) consists of an overlap of two exponential terms, the first one corresponding to the anodic and the second one to the cathodic half-reaction. For low overpotentials, the currents originating from these two reactions overlap, resulting in low net currents, at high positive (negative) overpotentials, the anodic (cathodic) reaction predominates. In a real system, the currents at high absolute overpotentials are limited by mass transport of reactants to or from the electrode. This can be described by a more complex modification of the Butler-Volmer equation including Fick's laws of diffusion, which will not be treated in this work.

2.2.2.3. Multistep reactions

So far, reactions consisting only of a single one-electron step have been considered. If a redox reaction

$$\mathrm{Ox} + n\,\mathrm{e}^- \rightleftarrows \mathrm{Red} \tag{2.49}$$

consists of a sequence of electron transfer steps, it is in general not possible to describe it by simple Butler-Volmer characteristics. However, in many cases one of the steps proceeds at a much slower rate than the others (ideally by at least a factor of 10), which determines the rate of the overall reaction. This sub-reaction is called the rate-determining step (RDS):

$$\mathrm{Ox} + \gamma\,\mathrm{e}^- \rightleftarrows \mathrm{Ox}' \tag{2.49a}$$

$$\nu(\mathrm{Ox}' + r\,\mathrm{e}^- \rightleftarrows \mathrm{Red}') \quad \text{(RDS)} \tag{2.49b}$$

$$\mathrm{Red}' + (n - \gamma - \nu r)\,\mathrm{e}^- \rightleftarrows \mathrm{Red}\,. \tag{2.49c}$$

Here, γ is the amount of electrons transferred in all steps prior to the RDS (2.49a), r is the number of electrons reacting per RDS (2.49b) and ν is the stoichiometric number, i.e. the number of repetitions of the RDS per one complete reaction (2.49). In this case, a more generalized Butler-Volmer equation can be used:

$$j = j_0 \left(\exp\left(\frac{\alpha_\mathrm{a} F \eta}{RT} \right) - \exp\left(-\frac{\alpha_\mathrm{c} F \eta}{RT} \right) \right), \tag{2.50}$$

where the apparent anodic and cathodic charge transfer coefficients are defined as

$$\alpha_\mathrm{a} = \frac{n - \gamma}{\nu} - r\alpha_\mathrm{RDS} \tag{2.51a}$$

$$\alpha_\mathrm{c} = \frac{\gamma}{\nu} + r\alpha_\mathrm{RDS}. \tag{2.51b}$$

Here, α_RDS is the charge transfer coefficient of the RDS. In general, $0 < \alpha_\mathrm{a/c} < n$.

There are two limiting cases of the Butler-Volmer equation, which are often considered, the high and the low overpotential case. For $|\eta| \gg \frac{RT}{\alpha_{\mathrm{a/c}} F}$, which is typically fulfilled for $|\eta| \gtrsim 50\,\mathrm{mV}$, the first (second) term in (2.50) prevails and the Butler-Volmer equation simplifies to

$$j = j_0 \exp\left(\frac{\alpha_{\mathrm{a}} F \eta}{RT}\right) \tag{2.52}$$

and

$$j = -j_0 \exp\left(-\frac{\alpha_{\mathrm{c}} F \eta}{RT}\right) \tag{2.53}$$

in the anodic and cathodic regime of the Butler-Volmer equation, respectively. Taking the logarithm leads to

$$\log_{10} j = \log_{10} j_0 + \frac{\log_{10}(\mathrm{e}) \cdot \alpha_{\mathrm{a}} F}{RT} \cdot \eta, \tag{2.54}$$

and

$$\log_{10} |j| = \log_{10} |j_0| - \frac{\log_{10}(\mathrm{e}) \cdot \alpha_{\mathrm{c}} F}{RT} \cdot \eta, \tag{2.55}$$

the so-called Tafel equation for the anodic and cathodic branch of the redox reaction. According to (2.54) and (2.55), a base-10 logarithmic plot of the absolute value of the current density j versus overpotential η, known as Tafel plot, leads to two straight lines at $|\eta| \gtrsim 50\,\mathrm{mV}$ (see Figure 2.4). Their slopes, also known as anodic and cathodic Tafel coefficients $\beta_{\mathrm{a/c}}^{-1}$, are equal to $\beta_{\mathrm{a}}^{-1} = \frac{\log_{10}(\mathrm{e}) \cdot \alpha_{\mathrm{a}} F}{RT}$ and $\beta_{\mathrm{c}}^{-1} = -\frac{\log_{10}(\mathrm{e}) \cdot \alpha_{\mathrm{c}} F}{RT}$. The exchange current density j_0 can be found by extrapolating the two straight lines to their intersection point at $\eta = 0$.

For small overpotentials $\eta \ll \frac{RT}{\alpha_{\mathrm{a/c}} F}$, the exponential function $\exp\left(\frac{\alpha_{\mathrm{a/c}} F \eta}{RT}\right)$ can be approximated by the first two terms in the Taylor expansion series $\exp x = \sum_{m=0}^{\infty} \frac{x^m}{m!} \approx 1 + x$. Thus, (2.50) yields

$$j = j_0 \frac{nF}{\nu RT} \cdot \eta, \tag{2.56}$$

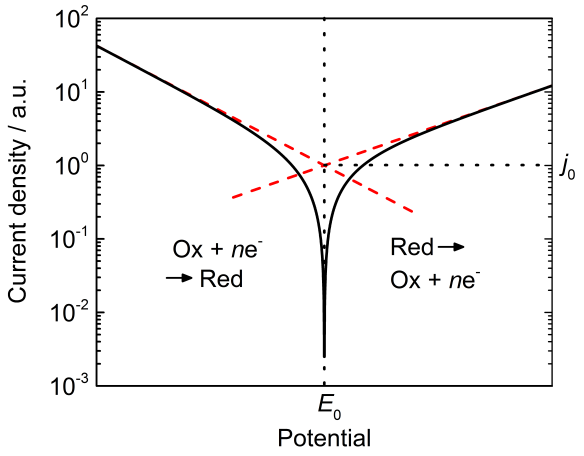

Figure 2.4.: Tafel plot of a redox reaction taking place at an electrode. Dashed red lines are fits to the current density - potential curves at $|\eta| > 50\,\mathrm{mV}$.

i.e. the current response on overpotential is linear. In the last step, $\alpha_\mathrm{a} + \alpha_\mathrm{c} = \frac{n}{\nu}$ (see (2.51)) has been used.

2.2.2.4. Mixed potentials

In the following, an electrode is considered, where two redox reactions

$$\mathrm{Red_A} \rightleftarrows \mathrm{Ox_A} + n_\mathrm{A}\,\mathrm{e}^- \qquad E^0_\mathrm{A} \qquad (2.57a)$$

$$\mathrm{Red_B} \rightleftarrows \mathrm{Ox_B} + n_\mathrm{B}\,\mathrm{e}^- \qquad E^0_\mathrm{B} \qquad (2.57b)$$

with two different equilibrium potentials E^0_A and E^0_B can occur simultaneously. Without loss of generality, $E^0_\mathrm{A} < E^0_\mathrm{B}$ is assumed. Especially in corrosion science, the electrochemical dissolution/oxidation of a metal $\mathrm{Red_A}$ (forward reaction in (2.57a)) is accompanied by the reduction of a species $\mathrm{Ox_B}$ (back reaction in (2.57b)), if no external current is supplied. In aqueous electrolyte, reaction (2.57b) is typically either the hydrogen evolution reaction (2.34) or the ORR (see below in subsection 2.2.3). In equilibrium, the net

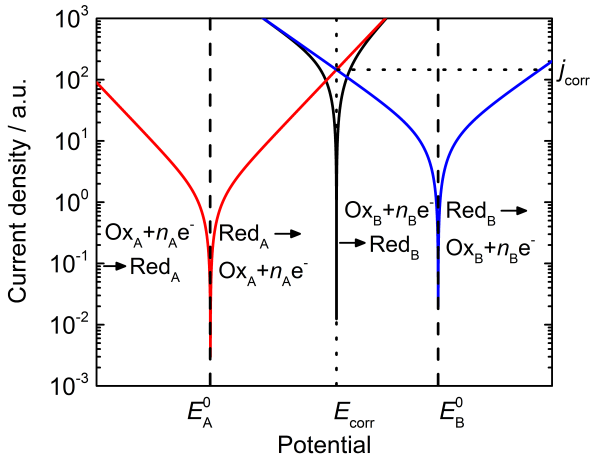

Figure 2.5.: Tafel plot of an electrode where two redox reactions take place. The current density j_{corr} and potential E_{corr} at the equilibrium are found at the intersection point of the two Tafel lines corresponding to reaction A (red) and B (blue) according to Equations (2.57).

reaction is

$$n_{\mathrm{B}}\,\mathrm{Red_A} + n_{\mathrm{A}}\,\mathrm{Ox_B} \rightarrow n_{\mathrm{B}}\,\mathrm{Ox_A} + n_{\mathrm{A}}\,\mathrm{Red_B} \qquad E_{\mathrm{corr}} \tag{2.58}$$

with a mixed or corrosion potential E_{corr} lying between E^0_{A} and E^0_{B} and corrosion current density j_{corr}. A theoretical treatment of this problem has been described for the first time by Wagner and Traud in 1938.[48] Their basic assumption is that in the absence of external current sources or sinks the rate of electron generation (oxidation of A) is equal to the rate of electron consumption (reduction of B). This leads to the conclusion that the equilibrium condition is found at the intersection point of the Tafel lines corresponding to the two half reactions (see Figure 2.5). If an external power supply is connected and a potential $E \neq E_{\mathrm{corr}}$ is applied, i.e. additional electrons are consumed or supplied, the current density curve follows the sum of the two individual branches, which can be calculated by the Butler-Volmer equation as shown in black in Figure 2.5.

2.2.2.5. Electrocatalysis

Several electrochemical reactions, e.g. those involving the breaking of a C-C or O-O bond, exhibit at least one sluggish reaction step, i.e. one with a high activation barrier, which results in low exchange currents. A high overpotential is necessary for the reaction to proceed at an adequate rate, thus lowering the efficiency of the overall reaction. The reaction rate can be increased by the use of an electrocatalyst. Just like catalysts in any chemical reaction, electrocatalysts lower the rate determining activation barrier by taking part in the reaction without being consumed or modified in the overall process. In many electrochemical reactions, the electrode acts as electrocatalyst. The activity of an electrocatalyst is determined by the surface of the electrode facing the electrolyte, i.e. composition, crystallographic orientation, defects, nanoparticles or biomolecules present on the surface.

The catalyst changes the reaction rate by interacting with the reactants. This can lower the activation barrier of the RDS or change the reaction path by creating a new intermediate with a lower Gibbs energy maximum to be overcome during the reaction. Plotting the exchange current density as a function of the interaction energy between reactant and different catalysts results in a so-called volcano plot (see Figure 2.6). This is explained by the Sabatier principle, which in simplified terms states that there is an optimum in the strength of reactant-catalyst interaction. If the adsorption is too weak, too few reactants can bind to the surface and react per time interval, if it is too strong, the catalyst will get blocked by reactants or products bound to the surface. Maximum activity is found at an intermediate bond strength.

It is important for the study of an electrocatalytic reaction that the electrolyte and the electrode are electrochemically stable in the potential range under investigation and do not interfere with the reaction of interest via auxiliary electrochemical reactions. Typical examples are C and Au surfaces. In order to suppress undesired side-reactions taking

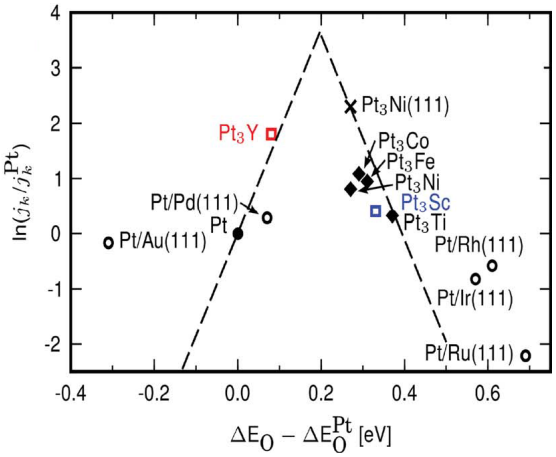

Figure 2.6.: Volcano plot for the oxygen reduction reaction at different catalysts. Oxygen interaction energies and current densities are plotted relative to Pt. From [49].

place at the electrode surface, it can also be covered by a thin layer of non-reactive material, like a SAM.

2.2.3. The oxygen reduction reaction

Due to the abundance of oxygen in the atmosphere and its high redox potential, the ORR is used as cathodic reaction in many fuel cells and lithium air batteries. In acidic media, this reaction can proceed either via the direct 4-electron pathway:

$$\mathrm{O_2 + 4H^+ + 4\,e^- \rightarrow 2H_2O} \qquad E^{00} = 1.23\,\mathrm{V}, \tag{2.59}$$

or via a 2-step process involving hydrogen peroxide as intermediate:

$$\mathrm{O_2 + 2H^+ + 2\,e^- \rightarrow H_2O_2} \qquad E^{00} = 0.67\,\mathrm{V} \tag{2.60a}$$

$$\mathrm{H_2O_2 + 2H^+ + 2\,e^- \rightarrow 2H_2O} \qquad E^{00} = 1.77\,\mathrm{V}. \tag{2.60b}$$

In general, the 2-step process is less efficient, as the peroxide intermediate can react back to oxygen via $H_2O_2 \rightleftarrows O_2 + H_2O$ or desorb from the electrode after the first step (2.60a). Hence, one requirement for a good ORR electrocatalyst is its selectivity towards (2.59).

Unfortunately, also the kinetics of the direct reaction is rather sluggish. Extensive efforts have been made to find an optimal catalyst for this reaction. The best inorganic catalysts, i.e. those located at the top of the volcano curve, are nanoparticles of Pt and Pt-based alloys like Pt_3Ni and Pt_3Y (see Figure 2.6). Still, exchange current densities are rather low and the minimal overpotentials are in the range 0.3 - 0.4 V[50]. The same is true for the reverse reaction to (2.59), the oxygen evolution reaction. Computational studies based on density functional theory (DFT) simulations associated the required high overpotentials with a so-called universal scaling relation.[51,52] Reaction (2.59) can be modeled as four consecutive steps. During each step a $(H^+ + e^-)$ pair is added to the intermediate oxygen containing species adsorbed $(*)$ on the electrode surface. Starting point is molecular oxygen that adsorbs to the surface:

$$O_2 + * + (H^+ + e^-) \rightarrow OOH* \tag{2.61a}$$

$$OOH* + (H^+ + e^-) \rightarrow 2OH* \tag{2.61b}$$

$$OH* + (H^+ + e^-) \rightarrow H_2O + * \quad (\cdot 2) \tag{2.61c}$$

According to multi-electron transfer theory, the energy levels of intermediate adsorbates ($OOH*$ and $OH*$) in reactions (2.61) are not independent of each other, but related linearly by a scaling factor. This makes it possible to describe the energy levels and the related activity of a chosen catalyst by the Gibbs energy of one of the oxygen-containing adsorbates only (see Figure 2.6).

The Gibbs energy of reaction for the 4-electron process (2.59) is

$$\Delta G = 4eE^0 = 4.92\,\text{eV}. \tag{2.62}$$

An ideal catalyst should generate the following conditions corresponding to equally separated energy steps:

$$G_{\mathrm{OOH}*,\mathrm{ideal}} = \ eE^0 = 1.23\,\mathrm{eV} \tag{2.63a}$$

$$G_{\mathrm{OH}*,\mathrm{ideal}} = 3eE^0 = 3.69\,\mathrm{eV}. \tag{2.63b}$$

Energies obtained from DFT calculations on two-dimensional electrodes show a scaling relation between the energies $G_{\mathrm{OH}*}$ and $G_{\mathrm{OOH}*}$ [53]:

$$G_{\mathrm{OH}*} = G_{\mathrm{OOH}*} + 3.29\,\mathrm{eV}. \tag{2.64}$$

Hence, it is not possible to find a two-dimensional material which catalyzes the ORR at an overpotential below

$$\eta = \frac{(G_{\mathrm{OH}*} - G_{\mathrm{OOH}*}) - (G_{\mathrm{OH}*,\mathrm{ideal}} - G_{\mathrm{OOH}*,\mathrm{ideal}})}{2e} = 0.4\,\mathrm{V}. \tag{2.65}$$

It has been suggested that three-dimensional catalyst structures could stabilize OOH$*$ relative to OH$*$ and thus help to overcome this universal scaling relation.[52] In nature, this is achieved with enzymes, which will be addressed in section 2.5.

2.3. Electrochemical methods

The main electrochemical methods used in this work are cyclic voltammetry and electrochemical impedance spectroscopy (EIS), both carried out in a standard three-electrode configuration controlled by a potentiostat.

2.3.1. Three-electrode half-cell measurements

In order to study redox reactions at a WE in an electrolyte solution, high control of current and potential at the electrode-electrolyte interface is required. This is realized

with a 3-electrode configuration, where the potential at the WE is controlled by a RE and the current is measured between the WE and a counter electrode (CE). While in general, one electrode can serve both as RE and CE in the two-electrode configuration, this complicates potential control due to the current flowing through the same electrode and is typically used if exact and stable potentials are less important.

The perfect RE would be an ideal nonpolarizable electrode, i.e. one with a defined potential that stays constant independent of current, equivalent to a very high current density. In a real system, an electrode with a stable and well-known potential in a defined environment is used. This RE is connected to a high-impedance input of the potentiostat reducing currents to a minimum and thus keeping the potential constant.

The purpose of a CE is to allow for current flow to/from the WE by closing the electric circuit. Therefore, it serves as an anode when the WE is operated as a cathode and vice versa. The CE potential is floating, thus allowing to adjust the current to the WE current. CE surface areas are considerably higher than those of the working electrode which prevents current limitations at the WE. To avoid any electrolyte contamination from dissolution of the WE, an electrode material has to be chosen that stays inert under the respective experimental conditions. Typical choices are noble metals like Au or Pt.

2.3.2. Cyclic voltammetry

Cathodic and anodic electrochemical redox reactions at the WE are investigated dynamically by recording the current during a triangular potential sweep that is applied to the WE. The potential starts at an initial potential in positive or negative direction at constant potential sweep rate (or scan rate) $\nu = \frac{\mathrm{d}E}{\mathrm{d}t}$. When a chosen positive or negative return potential is reached, the scan direction is reversed and the potential is cycled between these two extreme values. During the scan, the current I is measured and the data points are plotted in an $I - E$ representation, the so-called cyclic voltammogram

(CV). To allow for comparison between different electrodes, the current is commonly referred to the surface area of the electrode A. The current density is defined as $j = \frac{I}{A}$.

At potentials where no redox reactions take place, only the charging current of the EDL is observed. From the definition of the differential capacitance C_D (see Equation (2.2)) follows

$$C_\mathrm{D} = \frac{\mathrm{d}\sigma}{\mathrm{d}E} = j\frac{\mathrm{d}t}{\mathrm{d}E}, \tag{2.66}$$

or after rearranging

$$j = C_\mathrm{D}\nu, \tag{2.67}$$

i.e. the current density depends linearly on the scan rate ν. For simplicity's sake, a potential independent C_D has been assumed in this derivation.

If a redox species is adsorbed on the electrode surface and the reaction is not kinetically hindered (which can be achieved by sufficiently low scan rates), two symmetric peaks for oxidation and reduction are observed. Both maxima are located at E^0, the peak current density j_p can be calculated as

$$|j_\mathrm{p}| = \frac{n^2F^2\Gamma_0}{4RT}\nu, \tag{2.68}$$

where Γ_0 is the surface coverage of the redox species. Hence, (2.68) predicts a linear dependency of j_p on the scan rate ν.

In case of redox species in solution, the oxidant (reductant) is consumed during the reduction (oxidation) reaction and has to be transported from the bulk electrolyte to the electrode surface via diffusion in order to take part in the redox reaction. This leads to a depletion of reactants in the proximity of the electrode surface, the diffusion layer. Hence, also in this case, a pair of peaks is visible, corresponding to the oxidation and reduction reaction. Mass transport limitation causes a separation between anodic and cathodic peak potentials in a CV, which, for a reversible system equals

$$E_\mathrm{a} - E_\mathrm{c} = \frac{2.3RT}{nF} = \frac{59\,\mathrm{mV}}{n}, \tag{2.69}$$

where $E_{a(c)}$ is the potential of the anodic (cathodic) peak. For the last step, a temperature of 25 °C has been assumed. The deviation of the peak separation in a non-reversible system may serve as a measure of the irreversibility of the process. The so-called formal redox potential for a reversible or quasi-reversible system is calculated via

$$E^0 = \frac{E_a + E_c}{2}. \tag{2.70}$$

The peak current density in $\mathrm{A\,cm^{-2}}$ at room temperature is obtained using the Randles-Sevcik equation

$$j_p = 2.69 \times 10^5 n^{3/2} D_0^{1/2} C_0^* \nu, \tag{2.71}$$

where D_0 is the diffusion coefficient in $\mathrm{cm^2\,s^{-1}}$, C_0^* is the bulk concentration of the redox species in $\mathrm{mol\,dm^{-3}}$ and ν is in $\mathrm{V\,s^{-1}}$.

2.3.3. Electrochemical impedance spectroscopy

While cyclic voltammetry belongs to the quasi-stationary methods, EIS is an alternating current (AC) technique that allows to gain information on electrical parameters in the electrochemical cell like electrolyte and charge transfer resistance or capacitance of the EDL. During an EIS experiment, a sinusoidal potential perturbation $E = E_{amp} \exp(i\omega t)$ is superimposed on a static potential applied to the WE in an electrochemical cell, where E_{amp} is the potential amplitude, $i = \sqrt{-1}$ the imaginary unit and ω the angular frequency. In order to keep the perturbation small and to get a linear response, $E_{amp} < 10\,\mathrm{mV}$ is used. The time-dependent current response $I = I_{amp}(\omega) \exp(i(\omega t + \varphi))$ of the system is recorded, where I_{amp} is the current amplitude and φ is the phase shift between potential input and current output signal. From the frequency dependent complex impedance

$$Z = \frac{E}{I} = \frac{E_{amp} \exp(i\omega t)}{I_{amp}(\omega) \exp(i(\omega t + \varphi))} = Z_{amp}(\omega) \exp(-i\varphi), \tag{2.72}$$

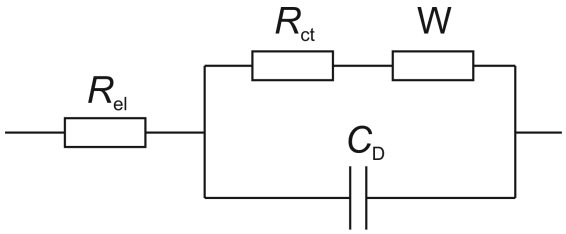

Figure 2.7.: Randles equivalent circuit for a redox reaction at an electrode-electrolyte interface taking into account diffusion of the redox couple in solution. R_{el} and R_{ct} represent electrolyte and charge transfer resistance, W is the Warburg element and the C_{D} describes the double layer capacitance.

information on the electrochemical system can be obtained.

In order to understand the generally complex behavior of $Z(\omega)$, the electrochemical cell is usually modeled by an electric equivalent circuit (EEC) with simple circuit components representing different electrochemical processes in the cell. The proposed EEC has to give a good physical description of the system and guarantee a good fitting of the experimental data. The simplest model describing an electrochemical cell that includes diffusion, charge transfer and the EDL capacitance is the Randles circuit (see Figure 2.7). Starting from the electrolyte (left side), the resistor R_{el} represents the ohmic resistance of the electrolyte between WE and RE. At the electrolyte-electrode interface, the current can take two paths. The first one is charging of the EDL, which is represented by the capacitor (bottom part of the parallel circuit) with impedance $Z_{\mathrm{C}} = \frac{1}{i\omega C_{\mathrm{D}}}$, where C_{D} is the EDL capacitance. The second path, electrochemical charge transfer through the interface, is described by the top part of the parallel circuit. It consists of a charge transfer resistance R_{ct} for the actual redox reaction at the surface and the so-called Warburg element W modeling diffusion processes of the redox species in solution. In general, the charge-transfer current response to an applied potential is described by the Butler-Volmer equation (2.50). Due to the small amplitude of the perturbation potential E_{amp}, the current response is locally linear, i.e. R_{ct} is

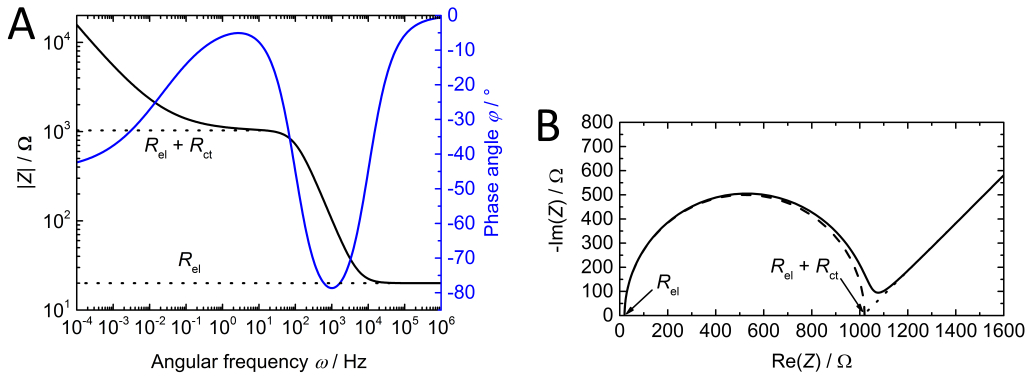

Figure 2.8.: A) Nyquist and B) Bode representations of impedance data that can be modeled by a Randles circuit according to (2.73) (see Figure 2.7). Parameters used to calculate these plots: $R_{\mathrm{el}} = 20\,\Omega$, $R_{\mathrm{ct}} = 1000\,\Omega$, $C_{\mathrm{D}} = 20\,\mu\mathrm{F}$, $\sigma = 150\,\Omega\,\mathrm{s}^{-0.5}$

modeled as ohmic. The Warburg impedance is $Z_{\mathrm{W}} = \frac{\sigma_{\mathrm{W}}}{\sqrt{i\omega}}$, where the Warburg coefficient $\sigma_{\mathrm{W}} = \frac{RT}{n^2F^2A\sqrt{2}}\left(\frac{1}{C^*_{\mathrm{Ox}}\sqrt{D_{\mathrm{Ox}}}} + \frac{1}{C^*_{\mathrm{Red}}\sqrt{D_{\mathrm{Red}}}}\right)$ is a function of the diffusion constants $D_{\mathrm{Ox\ (Red)}}$ and bulk concentrations $C^*_{\mathrm{Ox\ (Red)}}$ of the oxidant (reductant) species taking part in the reaction. The resulting expression for the impedance is

$$Z = R_{\mathrm{ct}} + \frac{1}{i\omega C_{\mathrm{D}} + \frac{1}{R_{\mathrm{ct}} + \frac{\sigma_{\mathrm{W}}}{\sqrt{i\omega}}}}. \tag{2.73}$$

By fitting an equivalent circuit like Figure 2.7 to the measured impedance $Z(\omega)$ of an electrochemical system, values for the above described parameters can be obtained.

There are two important representations for impedance data that will be used in this work, the Bode and the Nyquist plot. The Bode plot consists of two graphs, $|Z(\omega)|$ and $\varphi(\omega)$ in double-logarithmic and semi-logarithmic presentation, respectively. The Nyquist plot uses the complex plane to depict the real and the imaginary part of Z. In Figure 2.8, both representations are shown for an electrochemical cell that can be modeled by Figure 2.7 with typical parameters. Starting at high frequencies, the capacitive impedance is negligible, only the ohmic resistance R_{el} is measured, as can be seen

by the plateau in the Bode plot Figure 2.8A. The corresponding phase shift is $\varphi = 0$. With decreasing frequencies, the influence of the capacitance increases and φ approaches $-90°$. At $\omega \approx 1 - 10\,\mathrm{Hz}$, a second plateau is visible corresponding to $|Z| = R_{\mathrm{el}} + R_{\mathrm{ct}}$ with φ approaching 0. Below 0.1 Hz, the Warburg impedance dominates in this example with a phase shift of $\varphi = -45°$.

The Nyquist plot consists of a semicircle at high frequencies and a straight line at lower values of ω (see Figure 2.8B). The semicircle (dashed line) corresponds to a Randles circuit without Warburg element, thus neglecting mass transport effects. The two points of contact with the abscissa, i.e. values where Z is purely real, correspond to R_{el} and $R_{\mathrm{el}} + R_{\mathrm{ct}}$. The Warburg element in the Randles circuit leads to a linear progression of the curve according to the dotted line with an angle of $\varphi = -45°$.

2.4. Electrode surfaces

In this work, mainly single-crystalline electrodes of Au and Cu are used. Due to high cost and high demands on preparation and handling, single-crystals are seldom used in practical applications. For basic research, they provide well-defined model surfaces that allow for a fundamental understanding of electrochemical and structural processes taking place at their surface.

2.4.1. Au(111) single crystals

The Au(111) surface is widely used in electrochemistry, e.g. as a support material for catalyst immobilization due to its (electro)chemical inertness towards the reaction of interest. This includes catalytic inertness and corrosion resistance in the chosen potential window for the chosen electrolytes. Additionally, Au(111) surfaces are well-suited for thiol SAM formation.

2.4.1.1. Structure and characteristics

Au does not react with most chemicals and shows a large electrochemical potential window between hydrogen evolution and Au oxidation, where mainly EDL charging occurs.[54] Au crystallizes in a face-centered cubic (fcc) phase with a lattice constant of $a_0 = 4.079\,\text{Å}$,[55] leading to a hexagonal symmetry of the unreconstructed topmost atomic layer in the (111) orientation with a next-neighbor spacing of $a = 2.88\,\text{Å}$. The surface ordering can be increased by flame annealing, which creates large atomically flat terraces. A side effect of this procedure is a reconstruction of the surface driven by a lowering of the surface energy. The reconstructed topmost atomic layer is compressed by 4.4%, equal to one additional atom every 22 atoms of the underlying lattice.[56, 57] The unit cell is rectangular with dimensions of $22 \times \sqrt{3}$. The arrangement of the reconstructed atoms relative to the unreconstructed ones results in alternating elevations and depressions of the top layer. Parallel stripes of constant height change their direction every 20 nm on average at angles of 120°,[57] leading to a zig-zag pattern, which is the origin of the alternative name for this structure, "Herringbone" reconstruction. In an electrochemical environment, the reconstruction of the Au(111) surface is lifted by increasing the potential above a certain value, depending on the electrolyte and on surface quality (∼0.5 V for a very low defect surface in H_2SO_4[54, 58]). By decreasing the potential below this value, the reconstruction is formed again, however in a less ordered way.[58–60]

2.4.1.2. Thiol self-assembled monolayers on Au(111)

In this work, Au(111) single crystals are used as support for enzyme immobilization. A main disadvantage of Au surfaces regarding biocompatibility is their high negative surface charge and strong interaction with organic material, which often leads to a denaturation and inactivation of biologic structures. This can be overcome by the formation of a monolayer of organic molecules creating an interlayer to protect the delicate

biomolecules. A simple method to achieve this is the formation of a SAM, preferentially by using thiols.[61] The thiol sulfur group has a high affinity for Au,[62] spontaneously forming a self-organized chemisorbed organic monolayer on the surface. The functional group, i.e. the second moiety of the thiol molecule usually determines the surface properties, e.g. the surface charge or its hydrophobicity.

The probably simplest protocol for SAM formation is the immersion of a clean Au surface in a dilute thiol solution in ethanol.[63] For many thiol species, this leads to a well-ordered monolayer, that densely covers the surface. The adsorption proceeds in three phases,[64] the first one being a random low density arrangement where the underlying reconstructed Au surface stays intact. During the second phase with medium thiol density, the Au reconstruction is lifted, and the redundant Au appears as adatoms on the surface. Finally, the thiols rearrange on the surface, creating a close-packed monolayer, phase three. During the rearrangement, the redundant Au adatoms move on the surface, creating one-monolayer deep pitch holes on the surface via an Ostwald ripening process.[65] The timescale for the first two steps of SAM formation is seconds to minutes, the final ordering takes hours to days. The interaction between the sulfur of the thiol end group and Au is dominated by bonds to a bridging adatom in the medium coverage phase.[66] In the final, dense arrangement, sulfur binding to threefold hollow sites on the atomically flat Au(111) exhibits the lowest surface energy and hence, most stable structure.[67] The tilt angle between the thiol's molecular axis and the surface normal is close to 30° for alkanethiols,[68] but can vary over a wide range for other thiols.[61] The variety of thiol SAMs is not limited to homogeneous single-species layers, but includes mixed monolayers. Depending on the relative length of the different thiol species and on the interaction between them, a separation into different domains of homogeneous phases or a mixing on the molecular level could be observed with STM.[69] For alkanethiols, long-chain molecules predominate in a mixed SAM, which can be explained by

the faster adsorption dynamics of longer molecules compared to short-chain thiols due to stronger intermolecular forces.[63]

2.4.2. Cu(111)

Monolayers of OH adsorbed on Cu(111) surfaces are used in this work to test the high-resolution capability of the SECPM technique. Similar to Au, the crystal structure of Cu is fcc, the lattice constant is $a_0 = 3.615\,\text{Å}$,[70] corresponding to $a = 2.56\,\text{Å}$ in the Cu(111) plane. Electrochemical properties and surface modifications of Cu(111) in 0.1 M NaOH at different electrochemical potentials have been thoroughly investigated; an overview is given in the introduction of Ref. [71]. EC-STM studies have revealed the morphologies and structures of metallic and oxidized Cu(111) in this electrolyte.[71–74]

These investigations show that the formation of anodic layers is preceded by adsorption of OH species at more negative potentials ($-0.70\,\text{V} < E < -0.25\,\text{V}$),[71–73] which is indicated by a redox peak pair in the underpotential range of oxidation. During adsorption, a reconstruction process of the Cu surface is evidenced by the lateral growth of the terraces. This is explained by a reordering of the topmost Cu plane from the close-packed structure of (111)-oriented metallic copper to the hexagonal structure of the Cu planes in (111) oriented Cu_2O. This reconstruction corresponds to a 30% decrease in the atomic density of the topmost Cu plane. The excess Cu atoms are transferred to the step edges of the terraces, which results in lateral growth of the terraces. The ratio of OH groups to Cu atoms in the reconstructed topmost plane is 1:4, as inferred from the structure of Cu_2O. The formation of the phase of adsorbed OH on reconstructed Cu is, therefore, thought to correspond to a precursor stage in the formation of Cu(I) oxide (Cu_2O) at a higher potential. At low overpotential of adsorption, the adsorbed layer preferentially nucleates at the step edges of the terraces. The adsorbed OH layer increases the image resolution of the step edges that appear fuzzy in their absence, which is assigned to a lower mobility of Cu atoms.

2.5. Bioelectrochemistry

In nature, the role of catalysts is mainly taken over by enzymes.[75] Their turnover rate, i.e. the number of catalyzed reactions per active site and time can reach values up to the diffusion limit of 10^7-$10^8\,s^{-1}$, which is several orders of magnitude higher than what can be achieved with inorganic catalysts. Furthermore, they are highly specific towards the catalyzed reaction, hence avoiding by-products like H_2O_2 as in reactions (2.60). There are two ways how the field of electrocatalysis can profit from enzymes: they can be used directly as biocatalysts on the cathode and/or anode in a biological fuel cell, or if the origin of their superior characteristics is understood, they can serve as an inspiration for new synthetic electrocatalysts that combine the advantages of biological and inorganic catalysts.[23]

2.5.1. Enzyme structure and kinetics

Most enzymes are globular proteins, i.e. they consist of a defined amino acid chain folded to a three-dimensional almost-spherical structure. Their typical molecular weight lies between 20 and 200 kDa[75], with 1 Da corresponding to 1 atomic mass unit. This usually makes them much larger than the reactants, which in enzyme bioelectrochemistry are termed substrates. Hence, during the reaction, the substrate is in contact with only a small fraction of the enzyme, the active center. In 1890, Fischer proposed a mechanism for enzyme-substrate interaction, called lock-and-key model.[76, 77] The specificity of most enzymes towards one or only very few reactants was explained by a perfect fit between these two species, i.e. the active center was thought of as a negative of the substrate. This mechanism was refined by Koshland in 1958 to the induced-fit model, which takes into account the flexibility of the enzyme.[78] The enzyme was no longer thought of as a rigid "lock", but as a molecule that deforms during enzyme-substrate interaction in order to stabilize the transition state of the reaction. Some enzymes need

additional molecules, called cofactors in order to catalyze a reaction. Cofactors can be metal ions or organic or inorganic compounds.

The kinetics of enzymatically catalyzed reactions was first described by Michaelis and Menten in 1913.[79] The basic reaction of an enzyme E with a substrate S is

$$\mathrm{E} + \mathrm{S} \underset{k_{-1}}{\overset{k_1}{\rightleftharpoons}} \mathrm{ES} \xrightarrow{k_2} \mathrm{E} + \mathrm{P}, \tag{2.74}$$

where $k_{1/-1}$ are the rate constants for the reversible reaction to the enzyme-substrate complex ES and k_2 is the rate constant for the decomposition of ES to E and product P. Due to the enzyme's high specificity, the second step is considered irreversible. According to the law of mass action, the changes over time in product and enzyme-substrate complex concentrations c_P and c_ES are

$$v := \frac{\mathrm{d}c_\mathrm{P}}{\mathrm{d}t} = k_2 c_\mathrm{ES} \tag{2.75}$$

$$\frac{\mathrm{d}c_\mathrm{ES}}{\mathrm{d}t} = k_1 c_\mathrm{E} c_\mathrm{S} - k_{-1} c_\mathrm{ES} - k_2 c_\mathrm{ES}. \tag{2.76}$$

Usually, a steady-state approximation for c_ES is used for this process,[80] i.e.

$$\frac{\mathrm{d}c_\mathrm{ES}}{\mathrm{d}t} = 0. \tag{2.77}$$

Thus (2.76) yields

$$c_\mathrm{E} = \frac{(k_{-1} + k_2) c_\mathrm{ES}}{k_1 c_\mathrm{S}}. \tag{2.78}$$

The Michaelis constant K_M is defined as

$$K_\mathrm{M} := \frac{c_\mathrm{E} c_\mathrm{S}}{c_\mathrm{ES}} = \frac{k_{-1} + k_2}{k_1} \tag{2.79}$$

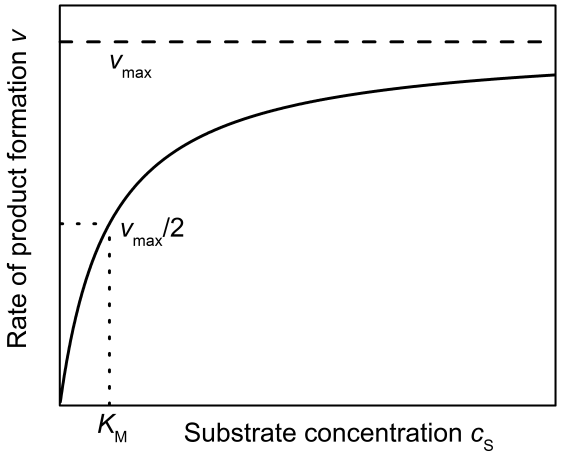

Figure 2.9.: Graph of the rate of product formation v according to the Michaelis-Menten equation 2.82. The limiting rate $v_{\max}$ and the concentration corresponding to the Michaelis constant K_{M} are indicated by dashed and dotted lines, respectively.

The number of enzymes is constant during the reaction

$$c_{\mathrm{E},0} = c_{\mathrm{E}} + c_{\mathrm{ES}} = \frac{c_{\mathrm{ES}} K_{\mathrm{M}}}{c_{\mathrm{S}}} + c_{\mathrm{ES}} \tag{2.80}$$

where $c_{\mathrm{E},0}$ is the initial concentration of enzymes and c_{E} has been replaced by (2.78). Solving (2.80) for c_{ES} and inserting the result in (2.75) yields

$$v = \frac{k_2 c_{\mathrm{E},0} c_{\mathrm{S}}}{K_{\mathrm{M}} + c_{\mathrm{S}}}, \tag{2.81}$$

the Michaelis-Menten equation.

In Figure 2.9, the reaction rate v is plotted as a function of the substrate concentration c_{S}. At high values of c_{S}, v approaches a limiting value $v_{\max} = k_2 c_{\mathrm{E},0}$. This is the situation, when every enzyme is continuously interacting with a substrate. Thus, equation (2.81) can also be written as

$$v = \frac{v_{\max} c_{\mathrm{S}}}{K_{\mathrm{M}} + c_{\mathrm{S}}}. \tag{2.82}$$

K_M corresponds to the substrate concentration, where $v(K_\mathrm{M}) = \frac{v_\mathrm{max}}{2}$.

Some enzymes catalyze a reaction via a so-called ping-pong bi-bi mechanism.[6] This means that two substrates A and B consecutively react to two products P and Q (bi-bi), whereby the catalyzing enzyme E changes to a modified form E* (ping) during the first reaction and reacts back to its initial state in the second step (pong):

$$\mathrm{E} + \mathrm{A} \rightarrow \mathrm{E}^* + \mathrm{P} \tag{2.83a}$$

$$\mathrm{E}^* + \mathrm{B} \rightarrow \mathrm{E} + \mathrm{Q} \tag{2.83b}$$

Examples for such a reaction are chemical groups or electrons that have to be transferred from substrate A to the enzyme before the reaction of B to Q can be catalyzed.

2.5.2. Oxygen reduction biocatalysis in multicopper oxidases

Multicopper oxidases (MCOs) are a family of enzymes belonging to the group of oxidoreductases that catalyze the ORR while concomitantly oxidizing a wide variety of substrates. Oxidoreductases are enzymes that catalyze redox reactions by taking electrons from the oxidation process of a donor molecule and by supplying them to the reduction of an acceptor. Members of the MCO family are laccases, bilirubin oxidases (BOxs), ascorbate oxidases and ceruplasmin. The name MCOs originates from the four Cu ions that serve as cofactors for the biocatalytic process. They are arranged in one single type 1 (T1) Cu, a single T2 Cu and the T3 site, a pair of Cu's, that are antiferromagnetically coupled through a bridging hydroxide ligand in their oxidized state. The T1 site exhibits a strong optical absorption band at ∼600 nm, which is the reason why this family of enzymes is also called 'blue' MCOs. The T2 and T3 Cu's are arranged in an almost equilateral triangle, the trinuclear cluster (TNC).

The biocatalytic process follows a ping-pong bi-bi mechanism. In short, a total of four substrates is subsequently oxidized at the T1 site via a one-electron reaction, the accepted

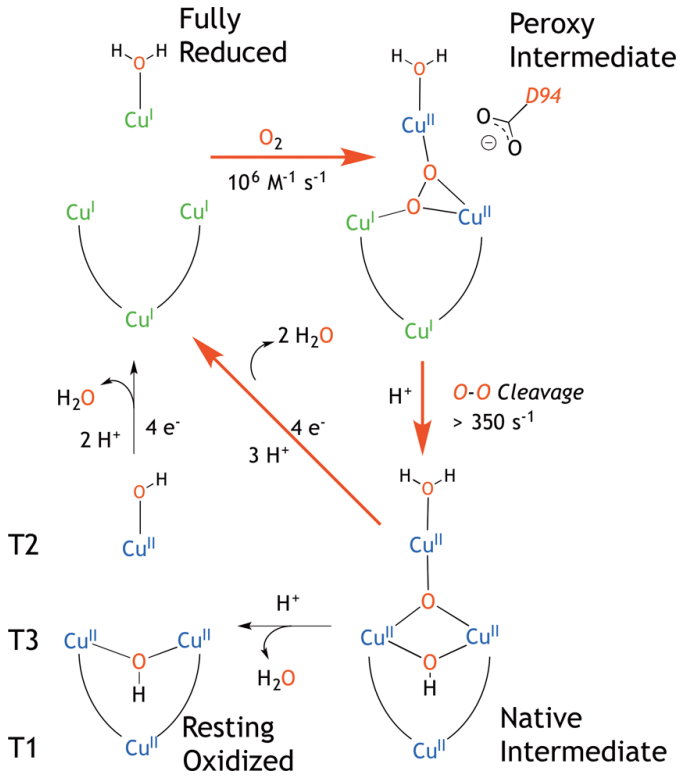

Figure 2.10.: Scheme of the molecular reaction mechanism in MCOs, where the oxidation of four substrate molecules is followed by the reduction of oxygen to water. From [84]

electrons are transferred from the T1 Cu to the TNC, where the four-electron reduction of oxygen to water takes place.[81] Although some details are still under discussion and can also differ between different MCOs, Solomon et al. developed a model for the molecular reaction mechanism based on a combination of spectroscopic techniques and DFT simulations (see Figure 2.10).[82–84]

Starting at the bottom left, the enzyme is in its resting oxidized configuration, i.e. all four Cu's are in the Cu(II) state. In the presence of substrate molecules, four electrons are received from the subsequent outer sphere oxidation of four substrate molecules at the T1 Cu. These electrons are transported along a cysteine-histidine (cys-his) pathway over a distance of ∼13 Å to the TNC, so that all four coppers are in the Cu(I) state (fully reduced configuration). This process is the slowest in the whole catalytic cycle.

The reaction of the fully reduced MCO with an oxygen molecule leads to the peroxy intermediate (PI) configuration, where O_2 is bound in a peroxy state bridging the T2 and T3 coppers of the TNC. Herewith, two electrons have been transferred from the T2 and one of the T3 Cu's, which return to their initial Cu(II) state. The cleavage of the peroxy O-O bond takes place during the decay of the PI to the native intermediate (NI) configuration, which is accompanied by the uptake of one proton. Hereby, also the remaining T3 and the T1 copper are oxidized to the Cu(II) state. In the absence of substrates, the enzyme reacts back to the resting oxidized state in a rather slow process, releasing one H_2O during this step. In the presence of substrates, a fast re-reduction from the NI directly to the fully reduced state occurs via the oxidation of four substrate molecules, leading to the release of two water molecules. The enzyme reacts along the catalytic cycle between fully oxidized - PI - NI as indicated by red arrows in Figure 2.10 as long as substrates are present in solution.

A typical characteristic of MCOs is the electrochemical potential of the T1 site E_{T1} as studied by redox titration experiments. While the T2 potential $E_{T2} \approx 400\,\mathrm{mV}$ for all studied MCOs, it was found that $400\,\mathrm{mV} \lesssim E_{T1} \lesssim 800\,\mathrm{mV}$.[85, 86] MCOs are divided according to their E_{T1} in low ($\lesssim 500\,\mathrm{mV}$), medium and high potential ($\gtrsim 700\,\mathrm{mV}$) enzymes. There is an ongoing controversy on how the ligand environment of the T1 copper influences E_{T1}.

2.5.3. Laccase from *Trametes versicolor*

Laccases (benzenediol:oxygen oxidoreductases, EC: 1.10.3.2) are an important member of the MCO family. The name laccase originates from the Japanese lacquer tree *Rhus vernicifera* where this enzyme was discovered in 1883.[87] Nowadays, these oxidoreductases are widely used in the food and textile industries.[88] For this study, laccase from the fungus *Trametes versicolor* (TvLc) was chosen as it exhibits one of the highest redox potentials of $E_{T1} = 780\,\mathrm{mV}$ among MCOs. This is only 150 mV lower than the formal

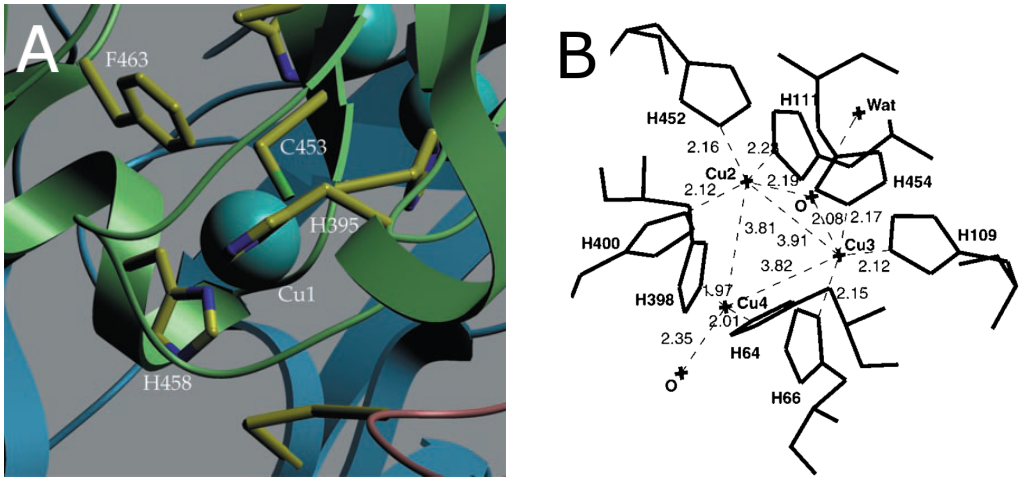

Figure 2.11.: Ligand environment of A) the T1 copper (Cu1) and B) the trinuclear center (Cu2, Cu3 and Cu4) in the enzyme laccase from *Trametes versicolor*. C, H, and F stands for cysteine, histidine, and phenylanaline, respectively. Numbers following single letters indicate the position in the amino acid chain. Isolated numbers are distances in Å. From [90].

ORR redox potential at pH 5. Its amino-acid sequence and crystallographic structure have been reported in Refs. [89, 90].

The T1 center is located ∼6.5 Å below the surface of TvLc in a hydrophobic pocket-shaped notch. The ligand environment of the T1 copper is shown in Figure 2.11A. It is threefold coordinated to the Nδ1 nitrogen of two histidines and the sulfur of a cysteine. At a closest distance of 12 Å from the T1 and connected via a His-Cys-His tripeptide, the two T3 coppers can be found. The mean distances between the coppers in the TNC are 3.85 Å (see Figure 2.11B). The two T3 Cu are four-fold coordinated via one common O and the N of six histidines. The T2 copper has three ligands, the N of two histidines and one O. Between the TNC and the surface, there are two narrow channels, which provide access for small molecules like O_2.

2.5.4. Multicopper oxidase immobilization on electrode surfaces

In order to use enzymes as bioelectrocatalysts, an electron transfer between the electrode surface and the enzyme has to be established. There are two main approaches to achieve this goal: mediator based or indirect electron transfer and DET. Mediators are electrochemically active molecules or ions that react readily with the electrode as well as with the enzyme. In case of a reduction reaction like the ORR, the electrons participating in the reaction are first transferred to the mediator and subsequently to the enzyme. Hence, the mediator redox potential has to be lower than the redox potential of the enzyme's active center, thus limiting the efficiency of the overall process. Mediators can be dissolved in the electrolyte and actively shuttle between electrode and enzyme[91] or be immobilized on the surface, e.g. as part of an organic monolayer[92] or a conductive polymer layer[93].

To make full use of the redox potential of some MCOs like TvLc, it is necessary to establish DET to the immobilized enzyme[94], i.e. electrons are directly supplied from the electrode to the T1 Cu, without intermediate redox molecules being involved in the process. It has been shown that for internal electron transfer in biomolecules, the maximum distance between redox centers has to be less than 14 Å.[95] This allows for efficient electron tunneling between the centers. The same principle seems to hold for DET, in this case for the distance between electrode surface and redox center.[96] The closest distance between the T1 center, i.e. the site where electrons are accepted in MCOs and a planar surface is ~ 8 Å.[97] Hence, if oriented with the T1 center facing the electrode, DET to the T1 Cu is possible with MCOs. The concomitant biocatalytic mechanism is similar to the natural process. Electrons are supplied from the electrode and transported via the T1 copper to the TNC, where the ORR is catalyzed.

There is a variety of strategies for enzyme immobilization on electrode surfaces: physisorption on bare and monolayer modified surfaces, covalent coupling, cross-linking, entrapment, etc. In the following, the first three methods will be treated more extensively

for MCO immobilization on carbon (C) and Au surfaces. Physisorption of different laccases and BOxs on unmodified C surfaces allows for DET-based ORR bioelectrocatalysis as has been shown by cathodic currents starting at potentials negative of the T1 redox potential.[19, 28, 29, 96, 98–100] It was concluded that the interaction between C and laccase leads to a preferred orientation of the enzyme with the active center facing the electrode.[96] Currents could be further increased by covering the electrode surface with monolayers of molecules exhibiting an aromatic moiety.[19, 29, 98, 100] The authors suggested that aromatic end groups protrude from the modified surfaces, which enables a specific binding to the enzyme's active center. This leads to a proper laccase orientation on the surface and consequent DET from the electrode to the T1 center.

The situation is different for MCO immobilization on Au surfaces. Most MCOs do not show ORR activity at high potentials on unmodified Au.[99–103] This can be partially explained by enzyme denaturation due to strong interaction between surface and protein. However, a cathodic wave starting at $\sim 400\,\mathrm{mV}$ is usually observed in these experiments. This has been assigned to bioelectrocatalytic reduction of oxygen to hydrogen peroxide. If immobilized enzymes are oriented in a way that their TNC is in tunneling distance from the surface, DET to the TNC without involvement of the high-potential T1 center is expected. This way, O_2 can only be reduced to H_2O_2 at potentials lower than the T2 redox potential ($\sim 400\,\mathrm{mV}$).[86, 104] There are few reports about high-potential DET bioelectrocatalysis on bare Au. Physisorption of laccase from *Coprinus cinereus* (CcLc) on Au(111) and BOx from *Myrothecium verrucaria* (MvBOx) on Au(111) and polycrystalline Au resulted in ORR currents starting at the T1 redox potentials of the enzymes.[102, 103] In case of these two enzymes, the surface charge of the proteins in the vicinity of the T1 center is predominantly positive.[102] Hence, an interaction with the negatively charged Au surface leads to a preferred enzyme orientation with the T1 copper facing the electrode. On nanoporous Au, laccase from *Trametes hirsuta* (ThLc) showed bioelectrocatalytic activity at onset potentials in agreement with the T1 redox

potential.[105] This was explained by enzyme immobilization in nano-cavities which decreases the average distance between the T1 center and the closest electrode surface.

Denaturation due to strong interaction between enzyme and Au electrode can be avoided by covering the electrode with a layer of organic molecules, like a thiol SAM (see subsection 2.4.1.2). Enzyme immobilization can be performed via the formation of covalent bonds between functional groups on the SAM and on the enzyme surface or via physisorption. The two most frequently used techniques for covalent immobilization are the formation of a peptide bond between an amine and a carboxylic acid moiety via a two-step process and the formation of a so-called Schiff base between a carbohydrate moiety of a glycoprotein and an amine group on the functionalized electrode surface. For MCO immobilization on SAM covered Au, both strategies applied individually did not result in observable current densities at high potentials that could be assigned to bioelectrocatalytic activity as each of these two techniques usually does not favor an oriented MCO immobilization with the T1 center close to the surface.[91, 106, 107] A combination of peptide bond and Schiff base formation on a mixed monolayer on Au was found to give current densities up to $\sim 30\,\mu A\,cm^{-2}$.[108,109] The authors suggested that this could be explained in part by the relatively high amount of sugar residues located close to the T1 center of the enzyme used in this study, ThLc. The reaction of the sugar molecules with amine moieties of one component of the mixed SAM during the Schiff base formation leads to an enzyme orientation favorable for DET bioelectrocatalysis. The authors also assumed that the hydroxyl moiety of the second SAM component further promotes an enzyme orientation with the T1 Cu close to the surface due to its similarity to natural substrates, which often contain hydroxyl groups.

Bioelectrocatalytic activity of MCOs physisorbed on SAM covered Au was found to be low or not detectable at all for most systems.[19, 86, 91, 99, 102–104, 110] One possibility to obtain high-potential ORR currents is to tailor the surface properties like charge and hydrophobicity to the used MCO. The environment of the enzyme surface surrounding

the T1 center can greatly differ between MCOs depending on the amino acids that are located there.[102] Depending on the pH of the electrolyte, arginine, histidine and lysine can show a positive charge, aspartic acid and glutamic acid are negatively charged and the other amino acids found in nature are hydrophobic. An attractive interaction between the T1 environment and the surface results in proper enzyme orientation for DET bioelectrocatalysis. Climent et al. used protein surface charge maps obtained from crystallographic data to explain varying activities of four MCOs on SAMs with different surface charges.[102] This effect has also been confirmed by an analysis of *Cerrena unicolor* laccase (CuLc) orientation on positively and negatively charged surfaces.[110] The protein orientation was obtained from infrared (IR) measurements and correlated to ORR activity.

A different strategy for proper enzyme orientation is based on attractive interaction between the cavity where the T1 center is located and the natural substrates of MCOs. Thorum et al. compared the activity of TvLc on single-crystalline and roughened Au surfaces covered with anthracene-2-methanethiol (AMT).[30] While ORR currents on the flat electrode were below the detection limit, high current densities of $\sim 10\,\mu A\,cm^{-2}$ were measured on the rough surface. The authors explained this by anthracene moieties protruding from the rough surface that mimic natural substrates and allow for an oriented enzyme immobilization with the T1 center close to the surface, similar to what has been observed on C surfaces covered with aromatic molecules. Current densities have been further increased to almost $25\,\mu A\,cm^{-2}$ by adding short ethanethiols to the SAM, which are supposed to bind to the surface in between the AMT molecules and thus increase the distance between neighboring linker molecules.

Isolated aromatic linker molecules where MCOs can bind to are a reasonable explanation for the current increase on monolayer covered C and Au surfaces. However, the high surface roughness of electrodes, where this effect has been observed in literature prevents a direct visualization of this effect, e.g. with scanning probe techniques. Scan-

ning probe microscopy (SPM) requires monoatomically flat surfaces to obtain molecular or atomic resolution. This can be used to determine the distance between neighboring linker molecules on a SAM covered surface and to study the effect of linker separation on the activity of immobilized enzymes. One of the goals of this thesis is the assembly of mixed SAMs on Au(111) with different distances between nearest linkers, i.e. different degrees of isolation and the investigation of the effect on enzymatic activity.

2.6. Electrochemical scanning probe microscopy

In 1982, Binnig and Rohrer reported about a new instrument, the STM, which allows for direct, real-space observation of surfaces on an atomic scale.[31] This was the first step towards a series of scanning probe microscopy (SPM) techniques including AFM and SECPM. In this section, the working principle of these instruments in air/vacuum and liquid environment will be discussed.

2.6.1. Electrochemical scanning tunneling microscopy

The STM makes use of the quantum mechanical tunneling of electrons between two electrodes. The probe, an ultra-sharp metal tip, is brought close to a conductive sample. At gap distances $z_{\mathrm{tip}} \lesssim$ nm, the electron wave functions of tip and sample overlap, resulting in a tunneling current between these two electrodes. This current depends on the applied bias voltage E_{bias} as well as on the distance z_{tip} between tip and sample and serves as feedback signal to control z_{tip}.

2.6.1.1. The tunneling effect

Formally, the space between tip and sample corresponds to a potential barrier that has to be passed by the electrons. Although forbidden in classical physics, quantum mechanics as described e.g. by the Schrödinger equation gives a finite probability for this effect by assigning a wave function to the particles, which yields a probability of presence in the

classically forbidden region. Theories presented in this subsection only deal with elastic tunneling, i.e. energy losses during the tunneling process are not taken into account.

If two metals with different electronic energy states ϵ as described by the Fermi function $f(\epsilon)$ are electrically connected, their Fermi levels align. In order to enable tunneling between them, a bias voltage E_{bias} has to be applied thus shifting the electronic energy level by eE_{bias}. Tunneling is only possible between the occupied states $f(\epsilon_\mu)$ of one metal and the unoccupied states $f(1-\epsilon_\nu+eE_{\mathrm{bias}})$ of the second. Tersoff and Hamann were the first to report about a theory describing tunneling in an STM,[111] based on a formalism developed by Bardeen in 1961.[112] The tunneling current I_{tun} is calculated via

$$I_{\mathrm{tun}} = \frac{2\pi e}{\hbar^2}\sum_{\mu\nu} f(\epsilon_\mu)[1-f(\epsilon_\nu+eE_{\mathrm{bias}})]\left|M_{\mu\nu}\right|^2\delta(\epsilon_\mu-\epsilon_\nu), \tag{2.84}$$

where the sum is over all possible states μ and ν of tip and surface, respectively, and $M_{\mu\nu}$ is the tunneling matrix element. Isoenergetic tunneling is included by $\delta(\epsilon_\mu-\epsilon_\nu)$. At the limit of low temperatures and for small bias voltages ($E_{bias} \lesssim 10\,\mathrm{mV}$), equation (2.84) yields

$$I_{\mathrm{tun}} = \frac{2\pi}{\hbar}e^2E_{\mathrm{bias}}\sum_{\mu\nu}\left|M_{\mu\nu}\right|^2\delta(\epsilon_\nu-\epsilon_{\mathrm{F}})\delta(\epsilon_\mu-\epsilon_{\mathrm{F}}). \tag{2.85}$$

From (2.85), one can see that only states with an energy close to the Fermi energy ϵ_F contribute to the tunneling current.

According to Bardeen[112], the tunneling matrix element can be calculated as

$$M_{\mu\nu} = \frac{\hbar^2}{2m}\int \mathrm{d}\boldsymbol{S}(\psi_\mu^*\boldsymbol{\nabla}\psi_\nu - \psi_\nu^*\boldsymbol{\nabla}\psi_\mu), \tag{2.86}$$

where m is the electron mass and $\psi_{\mu(\nu)}$ is the wave function of the tip (surface). The integral is over any surface S lying entirely in the region of the isolator. By describing ψ_μ as spherical waves, i.e. taking into account only s orbitals for the tip, Tersoff and

Hamann found

$$M_{\mu\nu} = \frac{2\pi\hbar^2}{m}\Omega_{\mathrm{t}}^{-1/2} R\,\mathrm{e}^{\kappa R}\,\psi_\nu(\boldsymbol{r}_0), \tag{2.87}$$

where Ω_{t} is the tip volume, R is the tip radius, $\kappa = \hbar^{-1}\sqrt{2m\phi}$ is the minimum inverse decay length for the wave functions in vacuum and ϕ is the work function of the metal. For simplicity, two identical metals have been considered as tip and sample material. $\boldsymbol{r}_0$ is the position of the center of curvature of the tip. Inserting (2.87) into (2.85) results in

$$I_{\mathrm{tun}} = 32\pi^3\hbar^{-1}e^2 E_{\mathrm{bias}}\phi^2 D_{\mathrm{t}}(\epsilon_{\mathrm{F}}) R^2\kappa^{-4}\,\mathrm{e}^{2\kappa R}\sum_\nu \left|\psi_\nu(\boldsymbol{r}_0)\right|^2 \delta(\epsilon_\nu - \epsilon_{\mathrm{F}}), \tag{2.88}$$

where D_{t} is the density of states per unit volume of the tip. For a spherical tip, $\left|\psi_\nu(\boldsymbol{r}_0)\right|^2 \propto \mathrm{e}^{-2\kappa(R+z_{\mathrm{tip}})}$, hence

$$I_{\mathrm{tun}} \propto E_{\mathrm{bias}}\,\mathrm{e}^{-\frac{2\sqrt{2m\phi}}{\hbar}z_{\mathrm{tip}}} = E_{\mathrm{bias}}\,\mathrm{e}^{-1.025\sqrt{\phi}z_{\mathrm{tip}}}\,. \tag{2.89}$$

The exponential dependency of the tunneling current on the gap distance between tip and sample surface is the reason for the extraordinary resolution of the STM in z direction. Furthermore, it simplifies the fabrication of STM probes. It is very challenging to obtain a tip that continuously tapers off, finally ending in a single atom at the very apex. In practice, tip apex radii $\mathcal{O}(10\,\mathrm{nm})$ with several sharp minitips are more realistic.[31] Due to the exponential dependency between I_{tun} and z_{tip}, only the minitip closest to the surface is used for tunneling.

Tersoff and Hamann also calculated the lateral resolution of an STM based on their assumption of s wave functions for the tip. The resulting value of lateral resolution is able to explain measured larger-scale structures like the reconstruction of Au surfaces, but fails to explain the observed atomic resolution achieved on many metallic surfaces. Chen extended the Tersoff-Hamann model by taking into account not only s wave functions, but also d_{z^2} states of the tip[113, 114]. His theory gives an explanation for the

atomic resolution data on Ag(111). A more detailed treatment of this and other theories describing tip-sample interactions can be found e.g. in [115].

2.6.1.2. Operation modes

In order to start an STM experiment, the tip has to be approached to the surface. This is typically done by applying E_{bias} between tip and surface and reducing the distance z_{tip} between them, e.g. with help of a micrometer screw. At close distances, I_{tun} rises according to (2.89) until a chosen setpoint current is reached. The position of the tip above the surface is then controlled with sub-nanometer precision by a piezoelectric scanner.

There are two ways how STM can be used for imaging of a sample surface: constant current and constant height. Constant current means that a feedback loop keeps I_{tun} at the setpoint value while the tip is scanned line by line over the surface. At depressions or protrusions on the surface, the tip's z position is re-adjusted to keep I_{tun} constant. The image contrast is calculated from the z position data. In general, the data contains a convolution of topographic features and electric properties, i.e. areas on the surface with low charge densities may appear lower because a closer tip-sample separation is necessary for the setpoint current. The maximum measurable roughness of the sample surface is determined by the piezo's z limits, the scan rate is limited by the sensitivity of feedback and scanner on changes in z direction.

The second imaging mode, constant height, avoids the limits of tip reaction by switching off the tip feedback in z direction. Hence, the tunneling gap changes while the tip is scanned over the surface. The image contrast is created from the resulting changes in tunneling current. This allows for a faster scan rate and often a concomitant higher lateral resolution. The disadvantage is that the tip cannot be withdrawn to evade obstacles on the surface and might crash into the sample if the tip-surface distance is decreased below the initial tunneling distance. Hence, this method can only be used on atomically

flat surfaces. Information about height differences is also limited as it is difficult to obtain this information from changes in tunneling current.

2.6.1.3. Scanning tunneling microscopy in electrochemical environment

In general, STM is not restricted to vacuum or air, but can also be operated in liquid environment. This mainly changes the tunneling barrier from typical values of $\phi_{\text{vacuum}} = 3 - 4\,\text{eV}$[116] to $\phi_{\text{H}_2\text{O}} = 1 - 2\,\text{eV}$[117, 118] in aqueous media. In practice, the immersion of an electrode in aqueous solutions will generate faradaic currents I_{Far} that depend on the area of the electrode surface. At typical dimensions of an STM tip, $I_{\text{Far}} \gg I_{\text{tun}}$. The current measured at the tip used for comparison with the setpoint current is the sum of I_{Far} and I_{tun}, hence the approach of the tip is hindered by the faradaic background current. This issue is typically overcome by covering the tip except for the very apex with an insulating material like polyethylene (PE), apiezon wax, glass, etc. If I_{Far} is reduced below typical setpoint currents $I_{\text{set}} \approx 0.1 - 1\,\text{nA}$, the tip can be approached to the surface. Only a few years after the invention of the STM, Sonnenfeld et al. showed the operation of this instrument on samples immersed in water, achieving atomic resolution on highly oriented pyrolytic graphite (HOPG).[119] The first reports about an EC-STM, which allows to control the potential of the sample, followed shortly after.[120, 121] The setup consists of an STM in combination with a bipotentiostat in a four-electrode configuration (see Figure 2.12A). Electrochemical potentials of sample and tip are individually controlled relative to a reference electrode, i.e. both act as a WE. By convention, only the sample is referred to as WE. The reference electrode might be e.g. a miniaturized Ag/AgCl electrode or a pseudo-reference electrode consisting of a wire of Pt, Ag or oxidized Au, if its potential is stable enough in the chosen electrolyte. Electrochemical currents are balanced by the counter electrode, typically a Pt or Au wire. Potential control at the sample allows to adjust the surface to the desired conditions, e.g. by choosing stable electrochemical conditions or inducing reactions at the surface

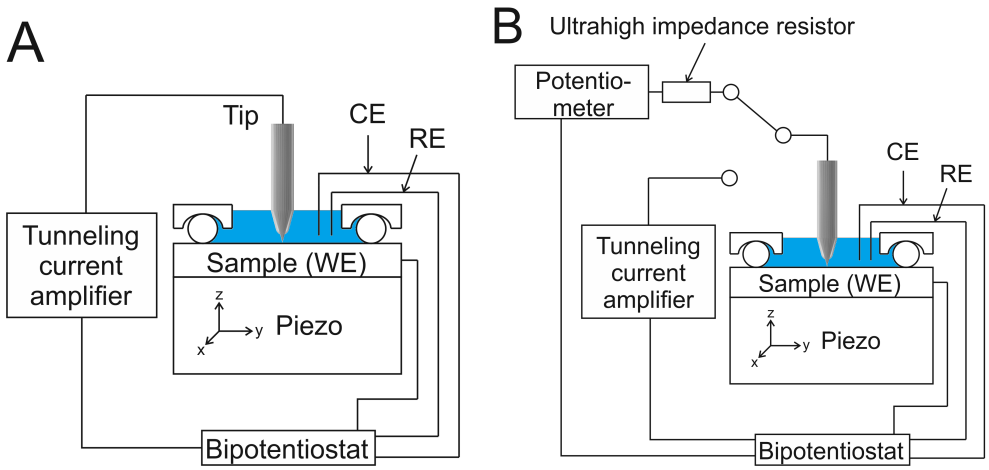

Figure 2.12.: Scheme illustrating the setup of A) an EC-STM and B) an SECPM instrument.

that can be studied by STM. The bias potential in an EC-STM is defined as $E_{\text{bias}} = E_{\text{tip}} - E_{\text{sample}}$, i.e. it results directly from the chosen tip potential.

EC-STM makes it possible to study an electrode surface immersed in electrolyte solution with unrivaled resolution. This includes the in-situ observation of electrochemical reactions induced at chosen potentials and the observation of biomolecules immobilized on electrode surfaces in their native liquid environment. Still, the last point is subject to some restrictions. At typical STM current setpoints of $0.1-1\,\text{nA}$, $\mathcal{O}(10^9\,\text{electrons/s})$ flow through an electrode area $\mathcal{O}(\text{nm}^2)$, resulting in enormous local current densities. For the imaging of delicate molecules like proteins, a SPM technique involving less interaction with the surface would be desirable.

2.6.2. Scanning electrochemical potential microscopy

During the last decades, there have been several approaches to study the EDL experimentally. Most of them were based on integral electrochemical techniques like EIS and cyclic voltammetry. Local techniques were mainly measuring the potentials indirectly via forces between probe and sample surface like Kelvin probe force microscopy also known as scanning surface potential microscopy.[122–124]

A more recent EC-SPM for the direct measurement of the EDL potential at an electrode surface immersed in electrolyte solution is the SECPM.[33] It is based on an EC-STM instrument, using a nanometer potential probe to scan the sample surface. This is expected to allow for a current-less measurement, hence reducing the tip-surface interaction to a minimum.

2.6.2.1. Operation principles

In an SECPM setup, the tunneling current amplifier of an STM is replaced by a potential difference operational amplifier with an ultrahigh input impedance ($\sim 10^{15}\,\Omega$), which suppresses the current flow through the tip (see Figure 2.12B). The potential of the sample is controlled in a three-electrode configuration, the tip is left at OCP. This allows to measure the potential difference between the probe and sample. At $I_{\mathrm{tip}} = 0$, the tip directly reads the potential in the electrolyte, i.e. it is supposed to follow the potential gradient in the EDL as described in section 2.1. In the system used in this work (Bruker Multimode 8), both EC-STM and SECPM are integrated in one head. An analog switch allows to change between these two modes without changing the hardware.

2.6.2.2. Potential distance curves

In 2004, Woo et al. reported about a modified EC-STM that allowed them to record potential-distance curves of the solid-electrolyte interface at sub-nanometer resolution.[125] They used Au probes flattened with an ultrashort pulse-etching method. This technique, now called SECPM was established in the group of Bard, who investigated the vertical potential profile on metallic and semi-conductive supports.[126] Yoon et al. managed to eliminate the hysteresis between tip approach and retract curves seen in other studies by using a gap-distance modulation technique.[127] They could show that their modulated potential-distance curves coincide mostly with the approach curve of an SECPM, i.e. the hysteresis mainly influences the retract curve. In all three studies a potential change

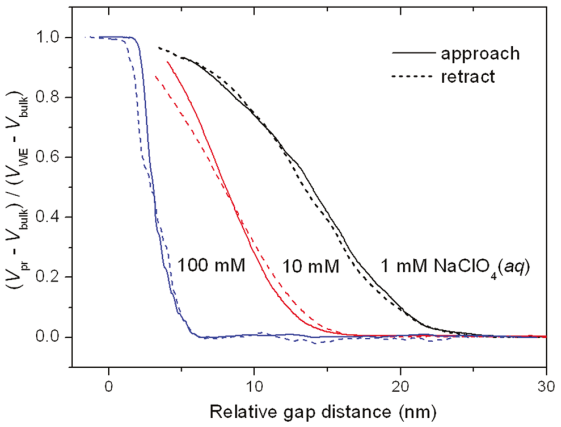

Figure 2.13.: Potential-distance curves obtained with a distance modulation technique at electrolyte concentrations of 1, 10, and 100 mM. V_{pr} and V_{bulk} are the distance dependent probe potential and the probe potential far away from the surface, respectively. V_{WE} is the working electrode potential. From [127].

from a bulk potential at tip positions far away from the surface to the potential applied to the surface at close distances is shown (see Figure 2.13). The distance over which the EDL potential decays to $\frac{1}{e}$ in the electrolyte is described by the Debye length λ_{D} (see (2.17)). The reported curves show the expected trend of decreasing decay length with increasing electrolyte concentrations. However, the obtained values for λ_{D} do not coincide well with the theory.

According to the GCS theory, the EDL potential should first drop linearly with increasing distance from the surface and, at the OHP, change to an exponential decrease. The exponential decrease is shown in all experimentally determined curves found in literature, but a clear linear regime could not be observed. Usually, the curves exhibit an inflection point and approach the sample potential in a sigmoidal way. There have been attempts to explain this behavior by the overlap between tip and sample EDL, which increases with decreasing gap distance. Deviations from the EDL theory have also been explained by the finite length of the tip.[34] Only a probe with z dimensions smaller than the variation of the EDL potential with distance could reproduce the double layer

potential. Any extended tip would measure an overlap of potentials at different z positions. This has also been studied by Hamou et al., who simulated SECPM potentials with the finite element method (FEM).[128] They showed that a flattened probe reproduces the EDL potential more precisely than an extended tip. However, in their studies, the probe potential did not reach the sample potential, even at closest distances. This can be understood by the tip's vertical extent. Even at closest approach, only the very apex of the tip reads the potential applied to the sample. The remaining non-isolated tip surface measures a different potential farther in the electrolyte. The weighted average will give a tip potential different from the surface potential. A sigmoidal bending of the potential towards the sample potential as observed in the experimental reports could not be seen in the simulations. To understand the experimental observations, it is necessary to identify the origin of the potentials measured with an SECPM that need further clarification and will be addressed in this work.

2.6.2.3. Lateral imaging

Comparable to STM, there are two methods to map an electrode surface with SECPM: constant potential and constant height mode. In both cases, the tip is first approached until the potential difference between surface and tip potential reaches a predefined setpoint potential ΔE. In constant potential mode, the potential gradient recorded with the probe is used as feedback signal to keep the tip-surface distance constant. In constant height mode, the z feedback is switched off, different tip-surface distances result in potential changes, which are used for the image contrast. In order to obtain high resolution in lateral direction, it is necessary to have a sharp tip contrary to potential-distance measurements, where a flat probe is preferred.[129] The first report about lateral imaging with SECPM was a study of the tungsten (W) distribution in diamond-like C films.[130] A comparative study of SECPM and EC-STM used enzymes attached to HOPG.[34] It was shown that SECPM could resolve substructures in the biomolecules

that were not visible with EC-STM. Various metal surfaces were investigated with AFM, EC-STM and SECPM, all three showing comparable resolution.[131] However, although SECPM is supposed to have a resolution similar to STM, no examples of atomically resolved structures have been reported with this method.

2.6.3. Electrochemical atomic force microscopy

Only four years after the invention of the STM, Binnig and Rohrer reported about a second SPM, the AFM.[32] This instrument measures the deformation of a cantilever in mechanical contact with a sample and thus can be used to map the surface of conductive and non-conductive materials.

2.6.3.1. Working principle

The AFM probe consists of a sharp tip attached to a cantilever with a defined force constant. When the tip is approached to a surface, distance dependent attractive and repulsive forces act between the apex of the tip and the surface atoms. The simplest model for the interaction between a tip atom i and a sample atom j at a distance r_{ij} is based on the Lennard-Jones potential:

$$V_{ij}(r_{ij}) = \epsilon \left[\left(\frac{r_\mathrm{m}}{r_{ij}} \right)^{12} - 2 \left(\frac{r_\mathrm{m}}{r_{ij}} \right)^{6} \right], \tag{2.90}$$

where the r^{-6} term represents attractive Van-der-Waals forces and the r^{-12} term originates from short-range repulsion between orbitals of two different atoms due to the Pauli principle. r_m and ϵ are the position and the potential value of the function's minimum. The force on the tip is given by summing over the interaction between all tip and sample atoms

$$\boldsymbol{F}_\mathrm{tip} = \sum_i \sum_j \frac{\mathrm{d}V_{ij}}{\mathrm{d}r_{ij}} \frac{\boldsymbol{r}_{ij}}{r_{ij}}. \tag{2.91}$$

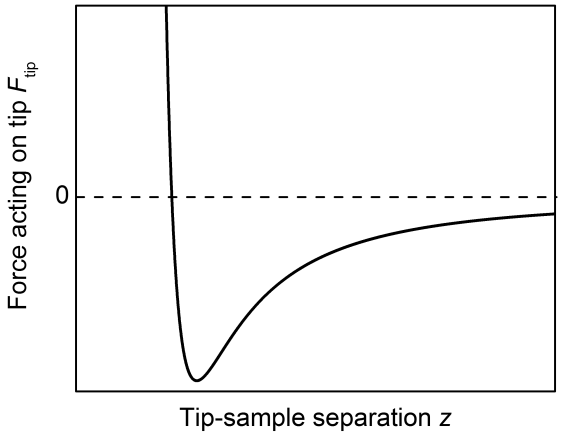

Figure 2.14.: Dependency of attractive ($F_{\mathrm{tip}} < 0$) and repulsive forces ($F_{\mathrm{tip}} > 0$) acting on an AFM tip on the separation between tip and sample surface according to (2.92).

For a tip shaped like a paraboloid of revolution interacting with a flat surface, (2.91) yields:[132]

$$F_{\mathrm{tip}}(z) = \frac{B}{180}\frac{R_{\mathrm{tip}}}{z_{\mathrm{tip}}^8} - \frac{A}{6}\frac{R_{\mathrm{tip}}}{z_{\mathrm{tip}}^2}, \tag{2.92}$$

where R_{tip} is the tip radius at its apex, $B = \pi^2 \epsilon r_{\mathrm{m}}^{12} \Omega_{\mathrm{tip}}^{-1} \Omega_{\mathrm{sample}}^{-1}$, $\Omega_{\mathrm{tip}}^{-1}$ and $\Omega_{\mathrm{sample}}^{-1}$ is the tip and sample volume, $A = 2Br_{\mathrm{m}}^{-6}$ and z_{tip} is the closest distance between tip apex and sample. When the tip approaches the sample, it is attracted by relatively long-range forces until repulsion forces prevail at closest distances (see Figure 2.14).

Tip-surface interaction leads to deflections of the cantilever, which have to be recognized by the system. Binnig and Rohrer used an STM attached to an AFM cantilever to measure these tiny changes in height.[32] Nowadays, usually the reflection of a laser beam from the backside of the cantilever is recorded by a photodiode sensor split into segments. Changes in cantilever deflection change the position of the laser spot on the photosensor, which is recorded by the control unit.

2.6.3.2. Surface imaging with Atomic Force Microscopy

There are three main methods for surface imaging with AFM: contact, intermediate-contact or tapping, and non-contact mode.[133] In contact mode, the tip is approached to the surface until a pre-set deflection of the cantilever is obtained, typically in the repulsive regime. While the tip is scanned over the surface, the piezo will vary the z position of the sample or tip in order to keep the deflection signal constant. This method applies the strongest force on the surface, which can help achieve high-resolution images. However, due to the close tip-surface interaction it is usually difficult to measure weakly adsorbed layers or biomolecules attached to the surface.

In tapping mode, the cantilever is oscillated at frequencies close to its resonance. When the tip gets close to the surface, tip-sample interaction will decrease the oscillation amplitude, which can be detected by the photosensor. Using the feedback to keep the amplitude at an predefined setpoint ensures a constant tip-surface distance. The main advantage of this method is the reduction of forces acting between probe and sample, which makes it also applicable to delicate samples.

While the first two methods usually work in the repulsive regime of tip-sample interaction, the non-contact mode allows for surface mapping in the attractive region. Here, the cantilever is oscillated at or close to its resonance frequency at an amplitude lower than in tapping mode. Long range attractive forces acting on the tip are usually detected by a change of frequency, but amplitude modulation can also be used to extract information about tip-surface interaction. Setting the feedback loop to a certain frequency or amplitude allows to follow surface features at a constant tip-sample separation.

The operation of an AFM in liquid environment under potential control, called EC-AFM is less complex than with an EC-STM.[134] It uses a three-electrode configuration, i.e. the probe stays passive (see Figure 2.15). The laser beam path has to be adjusted for refraction in the liquid environment it passes, and in tapping mode the cantilever resonance frequency is altered due to damping in the liquid medium.

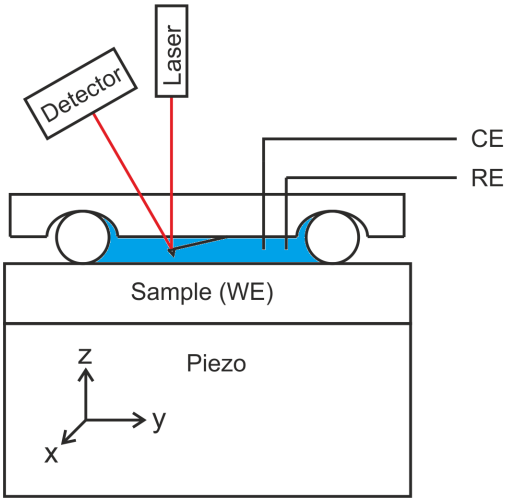

Figure 2.15.: Working principle of an EC-AFM.

2.6.3.3. Image artifacts

The main image artifact observed with AFM is the tip convolution effect. If the tip radius r is of the same order or greater than the size of a particle on the surface, the contour traveled by the tip is greater than the particle size (see Figure 2.16). A formula for this effect based on geometrical considerations is:[135]

$$x_{FWHM} = 2\sqrt{rd + \frac{d^2}{4}}, \tag{2.93}$$

where d is the diameter of a sphere on the surface and x_{FWHM} is the apparent full width at half maximum diameter of the sphere as observed with AFM.

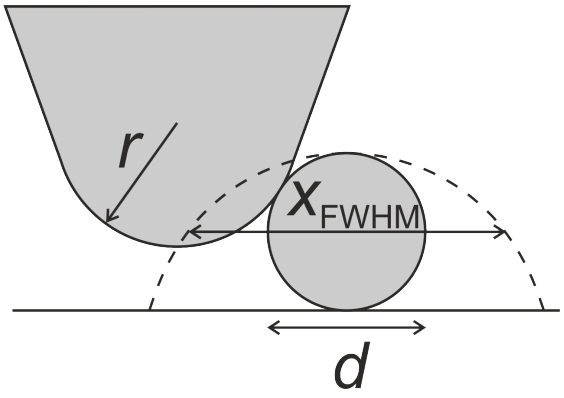

Figure 2.16.: Scheme illustrating the tip convolution effect. A tip with radius r scanning a spherical particle on a surface has to follow a greater contour as indicated by the dashed line.

3. Materials and experimental setup

In this chapter, the experimental details of the investigations carried out in this work are presented. An overview on the preparation of substances and electrodes is given as well as details on the electrochemical and electrochemical scanning probe microscopy setups.

3.1. Chemicals and materials

Chemicals and gases used in this work are listed in Tables 3.1 and 3.2. "Sigma-Aldrich" refers to Sigma-Aldrich Corp. (St. Louis, MO, USA) and "Merck" to Merck KGaA (Darmstadt, Germany). "p.a." is short for pro analysi. All gases were provided by Linde AG (Munich, Germany).

Au and Pt wires used as CE and pseudo-RE with a diameter of 0.25 mm and 0.5 mm and a purity of 99.99% were purchased from Carl Schäfer GmbH & Co. KG (Pforzheim, Germany). Au wires for bead single crystal preparation (1 mm, 99.999%) were acquired from Alfa Aesar (Ward Hill, MA, USA). The supplier of tungsten wire (W, 0.25 mm, >99.95%) was Mateck GmbH (Jülich, Germany). Ultrapure water (18.2 MΩ cm, 3 ppm total organic content (TOC)) was obtained from a combined Milli-Q Gradient / Elix 5 water purification system (Merck Millipore, Darmstadt, Germany).

Table 3.1.: List of commercially obtained chemicals used in this work. In alphabetical order.

Name	Formula	Supplier	Purity
2-Naphthalenethiol	$C_{10}H_8S$	Sigma-Aldrich	99%
2,2'-Azino-bis(3-ethylbenzo-	$C_{18}H_{24}N_6O_6S_4$	Sigma-Aldrich	98%
3-Mercaptopropionic acid	$C_3H_6O_2S$	Sigma-Aldrich	99%
thiazoline-6-sulphonic acid)			
Acetic acid	$C_2H_4O_2$	Sigma-Aldrich	99.99%
Citric acid monohydrate	$C_6H_8O_7 \cdot H_2O$	Sigma-Aldrich	99.5%
Ethanol (absolute)	C_2H_6O	Merck	p.a.
Hydrochloric acid (32%)	HCl	Merck	p.a.
Hydrogen peroxide (30%)	H_2O_2	Merck	p.a.
Nitric acid (65%)	HNO_3	Sigma-Aldrich	p.a.
Phosphoric acid (60%)	H_3PO_4	Merck	p.a.
Potassium hexacyanoferrate(II)	$K_4[Fe(CN)_6] \cdot 3H_2O$	Merck	p.a.
Potassium hexacyanoferrate(III)	$K_3[Fe(CN)_6]$	Merck	p.a.
Sodium acetate	$NaC_2H_3O_2$	Sigma-Aldrich	>99%
Sodium citrate	$Na_3C_6H_5O_7$	Sigma-Aldrich	99.5%
Sodium hydroxide	NaOH	Sigma-Aldrich	99.99%
Sodium phosphate dibasic	Na_2HPO_4	Sigma-Aldrich	99.5%
Sulphuric acid (96%)	H_2SO_4	Merck	p.a.

3.2. Cleaning and preparation procedures

3.2.1. Cleaning procedures

Prior to use, all glass, polytetrafluoroethylene (PTFE) and noble metal parts were immersed in fresh piranha solution, a mixture of H_2SO_4 and H_2O_2 at a volume ratio of 3:1. (*Caution: Piranha solution is highly corrosive and reacts violently with organic matter!*) Subsequently, the parts were thoroughly rinsed with Milli-Q water and dried in a stream of Ar. Au and Pt wires were flame annealed to weak red glow in a propane flame for ∼1 min, again rinsed with Milli-Q water and dried with Ar.

Table 3.2.: Gases used in this work

Name	Formula	Purity
Argon	Ar	99.998%
Hydrogen	H_2	99.999%
Oxygen	O_2	99.999%

3.2.2. Preparation of electrolytes

All electrolytes were prepared using Milli-Q water. For 0.1 M citrate buffer pH 5, 0.1 M sodium citrate monohydrate was added to 0.1 M sodium citrate until the desired pH was reached. The pH value was monitored using a Voltcraft PH-100 ATC (Conrad Electronic AG, Wollerau, Switzerland). Prior to each measurement, the pH meter was calibrated using pH 4.01 and 7.00 buffer solutions (Schott Instruments GmbH, Mainz, Germany). 10 mM acetate buffer pH 5.5 was prepared by adding acetic acid to 10 mM sodium acetate. McIlvaine buffer pH 5, which was used for all electrochemical and EC-SPM measurements involving TvLc, is a mixture of 0.2 M sodium phosphate dibasic and 0.1 M citric acid.

3.2.3. Synthesis of thiolated veratric acid

tVA was synthesized in the group of Prof. Jan Biernat according to a procedure described in Ref. [19]. In short, veratroyl chloride was prepared as a first step by adding thionyl chloride and dry pyridine to 3,4-dimethoxybenzoic acid and removing the volatiles. For the synthesis of tVA, veratroyl chloride was added to a solution of cysteamine hydrochloride, pyridine and water. After acidification, the product was extracted with ethyl acetate. Removing the solvent, trituration with saturated sodium bicarbonate solution, filtering and washing with water yielded the solid product.

3.2.4. Enzyme purification

TvLc powder with an activity of 13.6 $\mathrm{u\,mg^{-1}}$ was purchased from Sigma-Aldrich. One unit (u) corresponds to the amount of enzyme that oxidizes 1 µmol of 2,2'-azino-bis(3-ethylbenzothiazoline-6-sulphonic acid) (ABTS) per minute. The enzyme was purified according to a previously published procedure with minor modifications.[30] The powder was dissolved in 10 mM acetate buffer pH 5.5 at a ratio of 2 $\mathrm{mg\,mL^{-1}}$, vortexed and sonicated for 5 min. In order to remove particles, the suspension was passed through a 0.22 µm syringe filter.

The supernatant was loaded into a DEAE gravity flow column (DEAE-Sepharose, Sigma-Aldrich Corp., St. Louis, MO, USA) and washed with five column volumes of 10 mM acetate buffer pH 5.5. These fractions showed negligible ABTS activity. The enzyme was eluted with five fractions of 10 mM acetate buffer and 0.1 M ammonium sulfate solution pH 5.5 and the activity was analyzed with ABTS. ∼10% loss in activity was found. After combining the fractions and buffer exchange to 10 mM acetate buffer pH 5.5, the cleaning procedure was repeated. The buffer of the resulting purified solution was exchanged to 0.1 M citrate buffer pH 5 and concentrated to an activity of 130 $\mathrm{u\,mL^{-1}}$. The total activity of the purified TvLc was ∼80% of the initial activity.

3.3. Electrode preparation

Electrochemical and EC-SPM experiments in this work were performed mainly on the (111) surface of single-crystalline Au and Cu electrodes. For CV measurements presented in section 4.2, W wire electrodes were used.

3.3.1. Au(111) single crystals

Two different kinds of Au(111) electrodes were employed. The first type was a single crystal purchased from Mateck GmbH, Jülich, Germany oriented in the (111) direction

with a precision of 0.4° and a surface roughness of 0.03 µm. In addition to the (111) orientation, it had a flat in the $[\bar{1}\bar{1}2]$ direction, which defines the in-plane orientation during SPM experiments. The production of the second type of Au(111) electrodes, bead-like or Clavilier type electrodes is described in the following.

3.3.1.1. Fabrication of Clavilier-type electrodes

In 1979, Clavilier et al. reported about the the low-cost (aside from the material cost) production of single-crystalline Pt(111) electrodes from Pt wires.[136] A similar method was used for the fabrication of Au(111) electrodes. The basic material was a Au wire (1 mm diameter, 99.999% purity) from Alfa Aesar, Lancashire, UK. Au wires with a lower purity were found to give unsatisfying results. The first step in the production was cleaning in fresh piranha solution to remove any organic contaminants from the surface followed by thorough rinsing with Milli-Q water. After drying, one side of the wire was carefully heated with a burner until the extremity started to melt. Both hydrogen-oxygen and propane-air flames were found to be adequate for this process. The melting was continued carefully, until the bead reached a size of $2 - 3$ mm. During cooling down, the bead crystallized, ideally as a single crystal. Sometimes brownish spots were found on the surface, which were identified as impurities, mainly consisting of iron, that diffuse to the surface during the heating process. These contaminants could be removed by immersing the bead in fresh aqua regia, a mixture of nitric acid and hydrochloric acid at a ratio of 1:3. After rinsing with Milli-Q water, the bead was heated again, until the lower part melted, which could be seen by a thin line separating the molten from the crystalline part. Continuous slow heating and cooling down was found to improve the single-crystallinity of the bead. At the end of the process, one or more facets were seen on the surface, which are oriented in the (111) direction. The backside of such a bead facet was then fixed to a Au foil by heating both pieces below the melting point

and pressing them together. These Au(111) electrodes can be used for (EC-)SPM and were found to give atomically flat terraces with sizes up to 1 µm.

For electrochemical measurements, the (111) surface had to be increased by oriented polishing in order to achieve currents detectable by electrochemical instruments. Such beads (0.25 mm diameter, orientation accuracy $<0.5°$, surface roughness 0.05 µm) were purchased from icryst, Jülich, Germany.

3.3.1.2. Annealing of gold single crystals

Prior to each experiment, the Au(111) single crystals were immersed in fresh piranha solution for at least one minute to remove organic contaminants on the surface. After thorough rinsing with Milli-Q water, the electrodes were flame annealed with a Bunsen burner. The crystal was slowly heated to weak red glow and kept at this temperature for at least one minute. This procedure was done in a dark environment to increase the contrast of the glowing crystal and thus avoid damage by overheating. After cooling down in an Ar atmosphere, the crystal was quenched with Milli-Q water. Repeating this step several times resulted in a surface free from contaminants with atomically flat terraces. After annealing, the Au(111) surface was reconstructed as confirmed in STM experiments by the typical herringbone $(22 \times \sqrt{3})$ pattern.

3.3.1.3. Formation of self-assembled monolayers and enzyme immobilization

SAMs in this work were all formed from EtOH or EtOH/H_2O solutions with a total thiol concentration of 1 mM. The water content in solution was adjusted by the addition of Milli-Q water. After the annealing procedure, the Au(111) single crystals were immersed in the thiol solution and kept there overnight. After $\sim$15 h, the electrode was taken out and rinsed with EtOH and Milli-Q water to remove unbound thiols.

The SAM covered electrodes were either used directly for measurements or immersed in a solution with purified TvLc. After 3 h, the enzyme covered electrode was directly

transferred to the electrochemical cell used for the measurements without allowing it to dry.

3.3.2. Cu(111) single crystals

Cu(111) single crystals were prepared according to a previously published procedure.[71] They were oriented using Laue diffraction with a precision of 1°. Prior to each measurement, they were mechanically polished with diamond slurry in several steps with decreasing grading. The final grain size was 0.25 µm. Subsequently, the crystals were electropolished for 5 min in 60% H_3PO_4 at a potential of 1.8 V versus a Cu counter electrode. In order to heal out defects and increase the terrace size, they were annealed at 800 °C in a quartz reactor under a flow of H_2 for 16 h. The crystals were stored in the reactor in H_2 atmosphere until used in an experiment. This helped minimizing the oxidation of the surface. After mounting the crystal in an electrochemical or EC-STM cell, the Cu(111) surface was exposed to the electrolyte at OCP and the potential was scanned from −0.25 V to −1.20 V to reduce the oxide film formed in air during the transfer.

3.3.3. Tungsten wire

W CVs were recorded in 0.1 M NaOH with a W wire that was also used as STM tip material. The electrode was freshly cut and cleaned with EtOH and H_2O prior to the experiments. The geometrical surface area exposed to the electrolyte was 0.08 cm^2.

3.4. Electrochemical experiments

Electrochemical experiments were carried out in a half cell made of glass in a three-electrode configuration and controlled by a potentiostat (see Figure 3.1).

Figure 3.1.: Model of an electrochemical glass half cell. The main compartment (left) contains WE (red), CE (green), two gas inlets and a gas outlet. The RE (blue) is connected to the main compartment via a Haber-Luggin capillary.

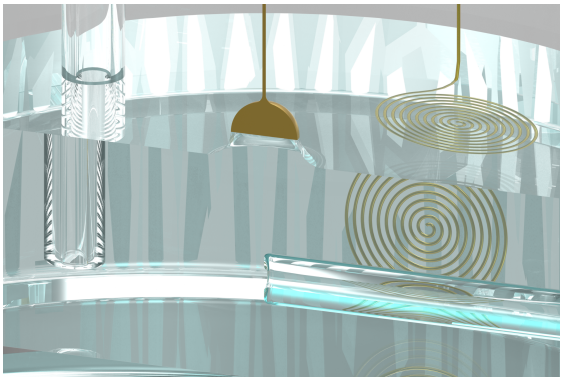

Figure 3.2.: Cut through the main electrolyte compartment shown in Figure 3.1. The Au bead of the WE is connected to the electrolyte via the hanging-meniscus configuration. The CE Au coil is visible in the background, gas inlet and Luggin capillary are shown at the left and at the bottom of the cell, respectively.

3.4.1. The electrochemical half cell

The main compartment of the glass half cell contained the CE, a Au coil with a wire diameter of 0.5 mm and the WE (see Figure 3.2). For measurements involving Au(111), a bead electrode was used as WE in the so-called hanging-meniscus configuration: the bead was approached to the electrolyte surface with the Au(111) surface aligned horizontally and facing downwards. As soon as the electrode got in contact with the liquid, it was withdrawn from the surface by a few mm. Due to surface tension, a liquid layer was retained between electrode and electrolyte. This ensured that only the Au(111) surface was in contact with the electrolyte. The geometric area of the Au(111) surface of the bead electrode was 0.049 cm^2. For experiments with Cu(111), the WE was inserted in a sample holder made of PTFE and sealed by an o-ring. The geometric area exposed to the electrolyte was 0.20 cm^2.

The RE was kept in a separate compartment connected to the main compartment by a Luggin capillary. This brought the RE close to the WE, thus minimizing IR drop in the cell. Experiments in basic solution were carried out using a Hg/HgO RE in 0.1 M

NaOH with a potential of 0.165 V. For measurements in McIlvaine buffer, the RE was Hg/Hg_2SO_4 in 0.1 M H_2SO_4 with a potential of 0.66 V. Both REs were purchased from Schott Instruments GmbH, Mainz, Germany.

To maintain a stable environment, the cell headspace and the electrolyte could be purged independently with gas through two separate inlets. The electrolyte was either purged with O_2 to increase the amount of oxygen from 0.25 mM in air saturated solution to 1.2 mM in O_2 saturated solution,[137] or with Ar to remove oxygen from the electrolyte. Purging of the cell was maintained for at least 15 min prior to all experiments.

The gas outlet was a small glass volume filled with water. It served as a bubble counter for the estimation of the gas flow rate and prevented diffusion of air into the cell.

3.4.2. Potentiostats

For data acquisition and potential control, three different potentiostats were used. For cyclic voltammetry measurements involving Au(111), a home-built potentiostat (Schramm Electronics, Düsseldorf, Germany) controlled by LabVIEW software was used. Cyclic voltammetry experiments with Cu(111) and W wire were carried out with a combined potentiostat/galvanostat PGSTAT 302N controlled by NOVA software (Metrohm Autolab B.V., Utrecht, The Netherlands). The potentiostat used for EIS experiments was a Biologic VSP (Biologic SAS, Claix, France).

3.4.3. Electrochemical impedance spectroscopy

EIS was used to determine the charge transfer resistance R_{ct} across different SAMs (tVA, MPA and 2-naphthalenethiol (NT)) at the Au(111)-electrolyte interface. The frequency range was 0.05 to 10^5 Hz, scanning 10 frequencies per decade, and using a sinusoidal signal with a voltage amplitude of 5 mV. The electrolyte was McIlvaine buffer pH 5 with each 2.5 mM $K_3[Fe(CN)_6]$ and $K_4[Fe(CN)_6]\cdot 3H_2O$, where Fe^{2+}/Fe^{3+} acts as redox couple. EIS was performed at the stable OCP (0.45 V, formal redox potential), which

was reached after measuring the equilibrium potential of the SAM covered Au(111) electrodes in the studied electrolyte for 20 min.

3.5. Electrochemical scanning probe microscopy setups

EC-SPM experiments were carried out with a Multimode 8 combined (EC-)STM, SECPM and (EC-)AFM sample scanning instrument (Bruker Nano GmbH, Berlin, Germany) and a 5500 AFM combined (EC-)STM and (EC-)AFM tip scanning device (Keysight Technologies, Santa Rosa, USA).

3.5.1. Electrochemical scanning tunneling microscopy and scanning electrochemical potential microscopy

The same setup was used for both EC-STM and SECPM experiments with the Multimode 8. This instrument was used for experiments involving TvLc covered electrodes and Cu(111) surfaces. High-resolution EC-STM imaging on SAM covered Au(111) was performed with the 5500 AFM.

3.5.1.1. Tip etching and insulation

There are two main techniques for the fabrication of STM tips: cutting and etching. Cutting is a rather simple method that, if applied properly, produces tips that yield atomic resolution on HOPG. For EC-STM it is less suited due to the irregularly shaped tip, which complicates tip insulation. Tips obtained from electrochemical etching are more regular and thus better suited for insulation. In this work, electrochemically etched tungsten tips insulated with PE were used.

Prior to etching, the rolled up W wire was straightened with a pair of tweezers and cut into pieces not longer than ∼7 cm each. Longer pieces were increasingly prone to vibration during the etching process thus reducing tip quality. The wire was fixed into a hypodermic needle for the etching procedure (see Figure 3.3A). A graphite rod

from a zinc-carbon battery was used as counter electrode in a two-electrode setup. A beaker filled with electrolyte, a 2 M NaOH solution was mounted on a height-adjustable platform and elevated until the W wire was immersed $1-2$ mm into the electrolyte. Both electrodes were connected to the ac power supply, a continuously adjustable transformer galvanically isolated from the electric grid. To start the etching process, the voltage was increased to 10 V, which resulted in bubbles generated at the wire. During the etching, the rate of bubble formation decreased continuously due to the dissolution of the immersed part of the wire. For a perfectly sharp tip, the etching process should be stopped a few seconds before it comes to an end on its own. This was done by lowering the platform with the beaker, thus removing the wire from the electrolyte. The tip was cut from the wire at a length of $\sim$ 1.5 cm. After rinsing with Milli-Q water, the tip was inspected with a microscope. Only tips with an etched front tapering off continuously with no rounding off at the very apex visible in the microscope were used for the experiments.

For the insulation procedure, a 1.5 mm thick copper plate with a 1 mm wide slit was attached to a soldering iron (see Figure 3.3B), similar to a setup reported in literature.[138] After heating the copper plate, a PE hot glue stick was molten until the slit was filled with PE. For the insulation, the tip was positioned below the molten PE with the sharp end facing upwards, carefully pushed through the transparent layer in the slit and moved out sideways. This lead to a tip covered with PE except for the very apex. The area of the tip protruding from the insulation layer depended on the temperature of the copper plate with higher temperatures leading to a greater free area. The free area is directly correlated to leakage currents observed in the EC-STM setup and had to be optimized by variation of current/temperature at the soldering iron.

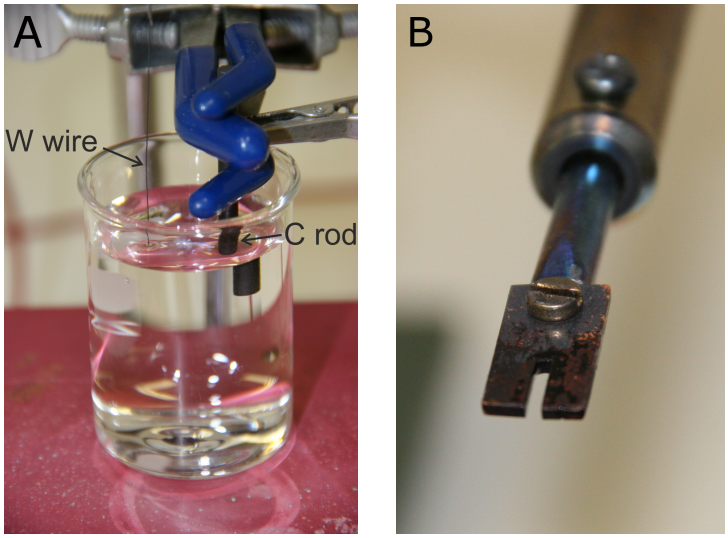

Figure 3.3.: A) Setup for W STM tip etching showing the W wire (left) and a carbon rod electrode (right) immersed in NaOH solution. The beaker containing the electrolyte is standing on a height-adjustable platform. B) Close-up of the modified soldering iron used for tip insulation. A copper plate containing a thin slit is screwed to the front of the device.

3.5.2. Liquid cells

The design of the liquid cell used for EC-STM experiments with the Multimode 8 was based on the commercial cell from Bruker Nano (see Figure 3.4). A groove for an o-ring was added to the top PTFE part of the cell, which was found to improve the sealing quality. The geometric area exposed to the electrolyte was 0.38 cm^2. The bottom part of the cell consists of ferromagnet steel ensuring a stable attachment and electric conductivity to the magnetic holder. The liquid cell for the 5500 AFM contains an o-ring, which gave an adequate sealing. Pt wires with a diameter of 0.5 mm were used as CE and pseudo-RE. The RE potentials were stable in 0.1 M NaOH and McIlvaine buffer pH 5 with potentials of 0.2 V and 0.8 V, respectively.

Tip potentials in SECPM mode and electrochemical currents in EC-STM mode were determined by first approaching the tip and then retracting it to a tip–WE distance

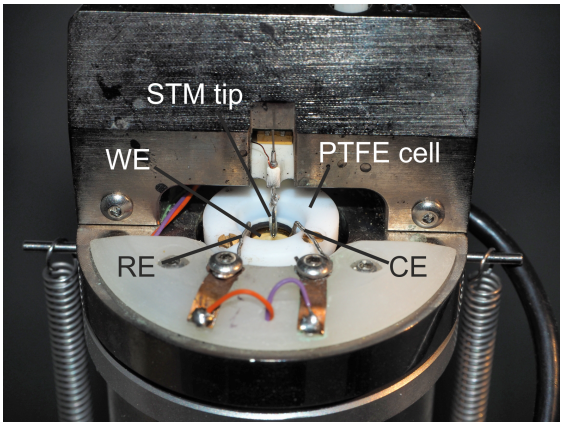

Figure 3.4.: Close-up of the Multimode 8 EC-STM/SECPM setup with a Au(111) single crystal in a liquid cell. Insulated tip, reference electrode and counter electrode are fixed to the instrument head.

$z_{\mathrm{tip}} = 20\,\mathrm{nm}$. Stable potentials were usually obtained after a waiting time of 10 – 60 min, and stable currents after 5 – 20 min.

For the direct determination of tip leakage currents I_{SECPM}, resistors with values of $R = 1$, 10, and $100\,\mathrm{G\Omega}$ ($\Delta R = \pm 5 - \pm 10\%$, esr GmbH, Ottobrunn, Germany) were used. Potential–distance measurements were carried out by first approaching the tip to a potential set-point of $\Delta E = 5\,\mathrm{mV}$. The tip was then retracted 10 nm from the surface and the tip potential was recorded as it was re-approached at a rate of $1\,\mathrm{nm\,s^{-1}}$.

3.5.3. Electrochemical atomic force microscopy

EC-AFM experiments were carried out with the Multimode 8 instrument.

3.5.3.1. Cantilevers

Commercially available ScanAsyst-Fluid+ cantilevers from Bruker Nano suitable for the use in liquid media were used for the experiments. The nominal specifications for this probe were: tip radius: 2 nm, resonant frequency: 150 kHz, spring constant: $0.7\,\mathrm{N\,m^{-1}}$.

3.5.3.2. The liquid atomic force microscopy cell

The EC-AFM cell was a transparent MMTMEC glass fluid cell (Bruker Nano) with an integrated holder for the cantilever. CE and RE were Pt wires fitted through the entry holes of the cell.

4. Results and discussion

In this chapter, the experimental results will be presented and discussed. It is divided into two main parts. Section 4.1 deals with electrochemical and EC-SPM studies of thiol SAMs for laccase immobilization and of the enzyme adsorbed on these surfaces. The goal is to gain further insights in the immobilization processes using EC-STM and SECPM. In the second part, section 4.2, OH adsorption on Cu(111) is investigated with SECPM. This surface, well-known from EC-STM studies, deals as a model surface to gain a deeper understanding of the SECPM working principle.

4.1. Laccase immobilization on Au(111) surfaces

In this study, TvLc is immobilized on mixed thiol SAMs on Au(111) consisting of a linker, tVA, where the enzyme is supposed to bind specifically and a diluent, MPA to increase the lateral spacing between the linker molecules. Depending on the assembly conditions of the monolayer, different molecular arrangements are observed with EC-STM on two different SAMs as shown in subsection 4.1.2. The electrocatalytic activity of TvLc on several monolayers is studied with cyclic voltammetry in subsection 4.1.3. In subsection 4.1.4, enzyme coverages on these two monolayers are determined with EC-AFM, EC-STM and SECPM.

4.1.1. Model for TvLc immobilization on mixed thiol monolayers

On several electrodes, bioelectrocatalytic activity of immobilized laccase has been explained by specific binding between the enzymes' active center and isolated linker molecules on the surface which exhibit a moiety similar to the enzyme's natural substrates (see subsection 2.5.4). This is intuitively plausible, however, there are no reports in literature about experiments verifying this theory on a local, molecularly resolved basis.

In this investigation, laccase activity is studied on two different mixed monolayers consisting of linker and diluent molecules as depicted in Figure 4.1. In case of a dense arrangement of linkers (see Figure 4.1A), specific binding to the enzyme's active center is strongly inhibited, hence oriented immobilization is not favored. Due to the random orientation of laccase on the surface, DET to the T1 center is possible only for a small fraction of enzymes, in most cases the T1 copper is too far away from the surface, which results in little to non-detectable ORR catalytic currents.

The second case, laccase immobilization on a mixed monolayer, where the lateral distance between linker molecules is increased by the incorporation of diluent molecules is shown in Figure 4.1B. If enzymes can specifically bind to isolated linkers, this allows for an oriented attachment with the T1 center close to the surface. DET along the linker to the T1 copper and subsequently to the trinuclear cluster leads to bioelectrocatalytic reduction of O_2 to H_2O detectable as currents in electrochemical experiments.

A real system used for such a study must fulfill several prerequisites. In order to assign enzymatic activity to DET along an isolated linker specifically bound to the enzyme, the biomolecule should not show catalytic activity neither on a monolayer consisting only of linker molecules nor on a pure diluent SAM. To exclude alternate reasons for enzymatic activity or the absence thereof, the same species should be used for the inactive and the active configuration. In this case, parameters have to be found to change the mixed monolayer from an inactive configuration where the linkers are densely arranged to an active configuration with an increased lateral distance between neighboring linker

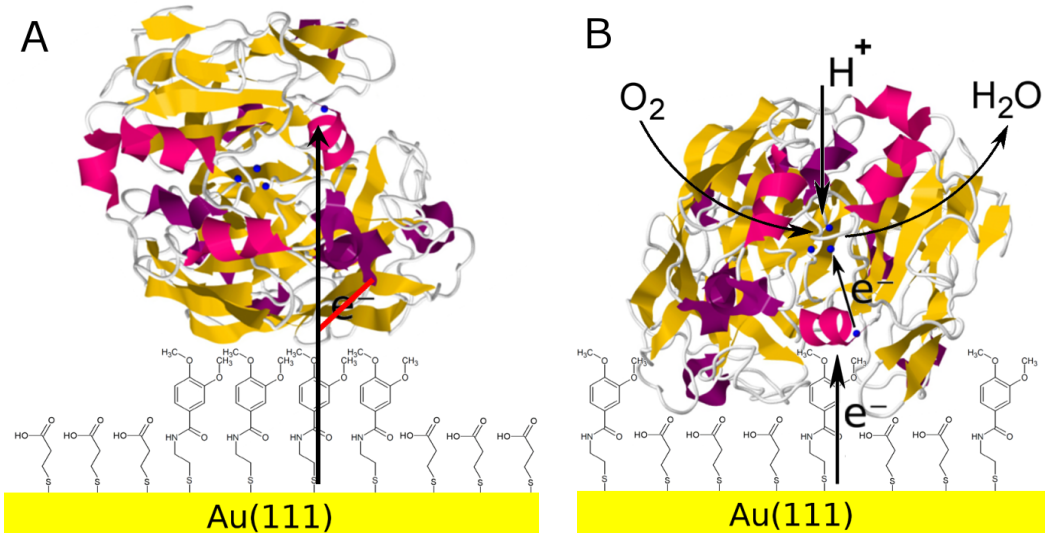

Figure 4.1.: (A) Laccase molecules immobilized on a mixed monolayer with densely arranged tVA linker molecules are expected to be randomly oriented. This prevents DET to the active center resulting in negligible bioelectrocatalytic activity. (B) Isolated linker molecules on the surface are supposed to bind specifically to the enzyme's active center resulting in DET to the T1 center and subsequent ORR catalytic activity.

molecules. The molecular arrangement has to be observed in the same environment used for experiments with immobilized enzymes, e.g. with EC-STM and finally a clear difference in current signal must be measured.

For this study, tVA is chosen as linker molecule. Carbon surfaces modified with veratric acid residues similar to tVA showed clear bioelectrocatalytic activities.[19] The negligible activity of laccase immobilized on a mixed monolayer of tVA and buthanethiol reported in literature[19] can probably be explained by the weak interaction between the two thiol species leading to a phase-separation into tVA and buthanethiol domains. In the present study, mixed monolayers of tVA and MPA as diluent are studied. The similarity in chemical structure between these two molecules is expected to facilitate mixing on the molecular level, e.g. via hydrogen bonds (see Figure 4.1B). In case of a molecularly mixed monolayer, the dimethoxybenzene moiety is supposed to protrude from the surface allowing for a specific laccase immobilization.

4.1.2. Molecular arrangements of linkers and diluents in mixed thiol monolayers

EC-STM studies are performed on two different enzyme-free mixed SAMs consisting of tVA and MPA in order to determine the arrangement of molecules in the monolayer. In this work, an important parameter is found to influence the SAM structure: the water content in thiol solution used for monolayer formation. Here below, high resolution EC-STM investigations of SAMs formed in thiol solutions with a tVA:MPA molar ratio of 1:99 are presented. The H_2O content in solution is 0% and 4%. All EC-STM studies presented in this section are carried out in McIlvaine buffer pH 5.

4.1.2.1. Monolayers assembled from a thiol solution containing 0% water

In Figure 4.2, an EC-STM image of the mixed monolayer assembled in a thiol solution containing 0% H_2O is shown. A phase separation is clearly visible on the surface, re-

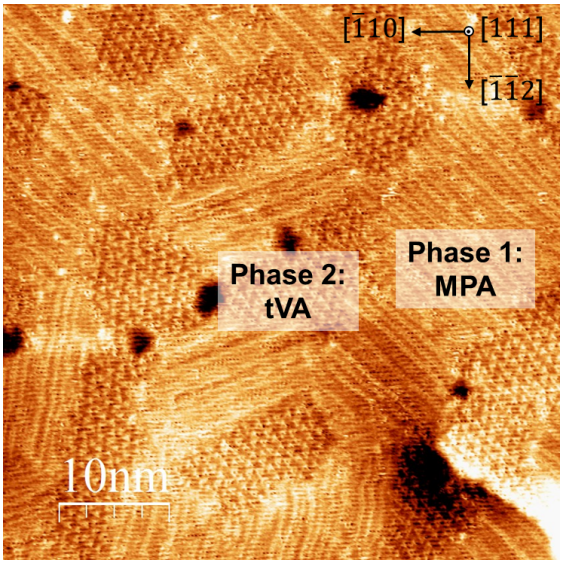

Figure 4.2.: EC-STM image of the mixed tVA/MPA monolayer assembled in a water-free solution. A phase-separation between stripe-like domains (phase 1) and domains consisting of triangular features (phase 2) is observed. In-plane orientations as known from the flat in the single-crystal are indicated in the top right corner. Imaging conditions: $E = 0.60\,\mathrm{V}$, $E_{\mathrm{tip}} = 0.20\,\mathrm{V}$, $I_{\mathrm{tun}} = 0.65\,\mathrm{nA}$, image size: $(50 \times 50)\ \mathrm{nm}^2$.

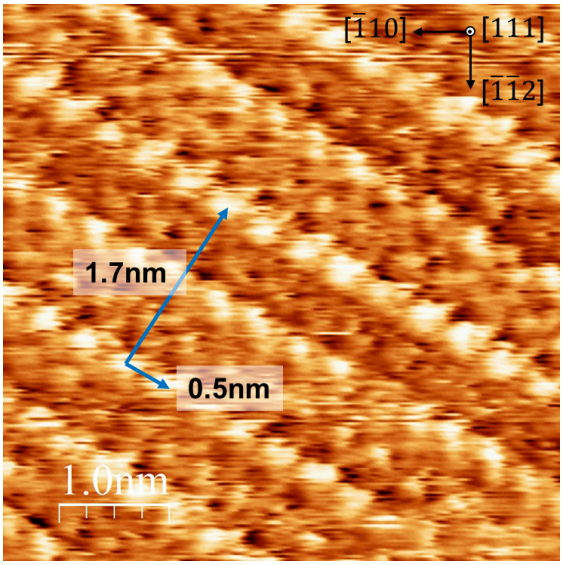

Figure 4.3.: Close-up showing the molecular arrangement of phase 1 in Figure 4.2. Dimensions of the rectangular unit cell are indicated by arrows. Imaging conditions: $E = 0.60\,\mathrm{V}$, $E_{\mathrm{tip}} = 0.20\,\mathrm{V}$, $I_{\mathrm{tun}} = 2.0\,\mathrm{nA}$, image size: $(5 \times 5)\ \mathrm{nm}^2$.

vealing stripe-like structures (phase 1) and triangular features (phase 2). The surface coverage of phase 1 and phase 2 is $\sim\frac{2}{3}$ and $\sim\frac{1}{3}$, respectively. Three different stripe orientations are found in phase 1, which can be related to the 120° symmetry of Au(111). Dark spots on the surface are due to one gold atomic layer deep holes typical for Au(111) surfaces covered with thiol SAMs.[61, 65]

A close-up of phase 1 is depicted in Figure 4.3. The molecules arrange in a rectangular pattern with an additional sub-structure visible between the bright rows. The dimensions of the unit cell are $(1.7 \times 0.5)\ \mathrm{nm}^2$, which corresponds to a $(6 \times \sqrt{3})$ ($6\,\mathrm{a} = 1.73\,\mathrm{nm}$, $\sqrt{3}\,\mathrm{a} = 0.50\,\mathrm{nm}$) adlayer, with the lattice constant of Au(111) being $a = 0.288\,\mathrm{nm}$. Such $(p \times \sqrt{3})$ unit cells, with p being an integer, have been reported for MPA SAMs.[139] Hence, phase 1 is identified as homogeneous MPA phase.

Figure 4.4A shows an image with molecular resolution of phase 2. It reveals a highly-ordered honeycomb-like pattern with clearly resolved substructure. The latter is formed by triangular features consisting of three bright spots at opposing angles. The distances

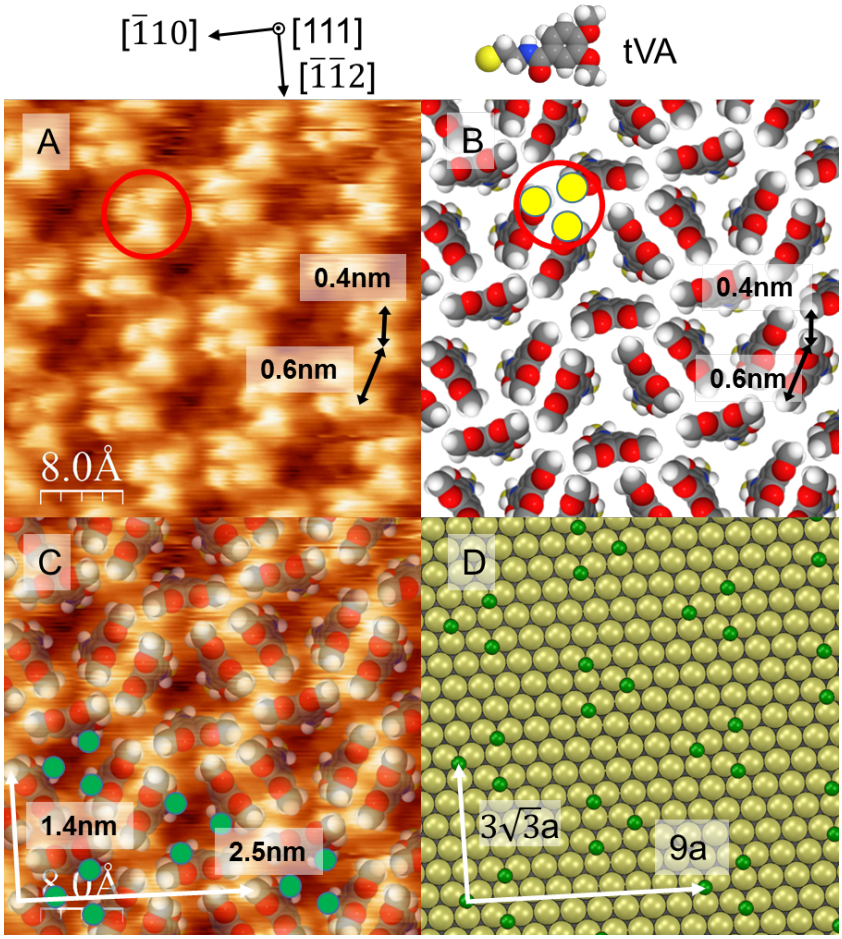

Figure 4.4.: A) High-resolution image of phase 2 in Figure 4.2. The red circle highlights one of the triangular features. Arrows indicate the distances between the nearest and next nearest neighboring spots. Imaging conditions: $E = 0.60\,\mathrm{V}$, $E_{\mathrm{tip}} = 0.20\,\mathrm{V}$, $I_{\mathrm{tun}} = 0.65\,\mathrm{nA}$, image size: $(4 \times 4)\ \mathrm{nm}^2$. (B) Molecular model of the structure observed in A. Three methyl groups forming the marked triangle in A are highlighted in yellow. (C) Molecular model overlaid on the STM image. The unit cell is marked with white arrows. Green spots represent positions of sulfur atoms in tVA molecules. (D) Model illustrating the location of sulfur atoms with respect to the Au(111) lattice. Unit vectors are marked in white.

between nearest neighbors in the triangle are in the range of 0.3 - 0.4 nm. Such distances are much smaller than the dimensions of a single tVA molecule, thus it can be concluded that the individual spots originate from densely packed exposed functional groups in the external part of the monolayer. The proposed arrangement of the molecules is presented in Figure 4.4B. It is assumed that the tVA adsorbs in upright configuration, with the molecular axis slightly tilted. This allows for a very close arrangement of the terminal methyl groups in the methoxy moieties of neighboring molecules at a distance comparable to their doubled van der Waals radius. As a result, each spot in one triangular feature corresponds to the methyl group of a different tVA molecule as shown in Figure 4.4B. The distances separating next nearest neighbors are ∼0.6 nm, which corresponds to the distance between the methyl groups in one tVA molecule. Thus, the structural model reproduces the STM contrast very well. Figure 4.4C shows the same model overlaid on the STM image, and the unit cell of the two-dimensional lattice is displayed. Due to symmetry reasons, its dimensions can be measured between corresponding bright features in the EC-STM image. The lengths of the two unit vectors are 2.5 nm and 1.4 nm with a 90° angle between them. The green circles in Figure 4.4C mark the position of the thiolate groups which are clearly also arranged in triangles. The specific location of the thiolate moieties with respect to the Au(111) lattice is shown in Figure 4.4D. The model shows the sulfur atoms bound at threefold hollow sites, which are energetically favored binding sites.[67] White arrows indicate the $(9 \times 3\sqrt{3})$ unit cell. The corresponding distances ($9\,a = 2.59\,nm$, $3\sqrt{3}\,a = 1.50\,nm$) are in good agreement with the measured distances. The considerations outlined above lead to the conclusion that phase 2 is a homogeneous tVA phase. There are 6 tVA molecules per unit cell, which results in a coverage of 1.7 molecules/nm^2.

Figure 4.2 shows that tVA molecules form domains, which means that under specific monolayer assembly conditions tVA – tVA and MPA - MPA interactions are more favorable than tVA - MPA interactions. Within such a domain (Figure 4.4), the molecules

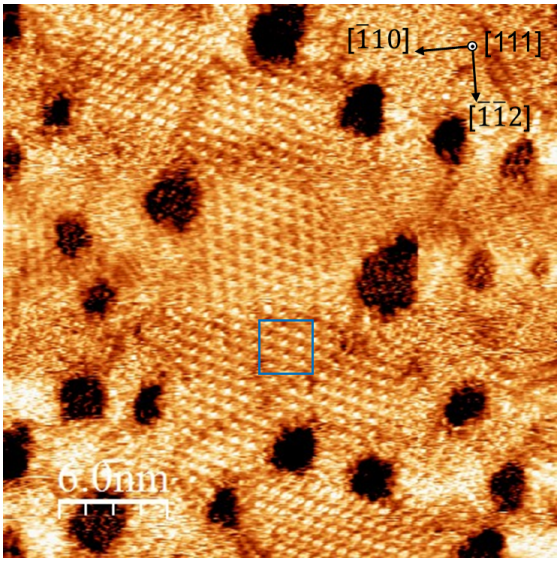

Figure 4.5.: EC-STM image of a tVA/MPA SAM on Au(111) assembled in a thiol solution with a water content of 4%. Only one homogeneous phase with hexagonal structure is visible. Imaging conditions: $E = 0.60\,\mathrm{V}$, $E_{\mathrm{tip}} = 0.40\,\mathrm{V}$, $I_{\mathrm{tun}} = 0.65\,\mathrm{nA}$, image size: $(30 \times 30)\ \mathrm{nm}^2$.

are organized in interconnected clusters consisting of three interacting tVA molecules, where all molecules that form one cluster belong to at least one neighboring cluster. According to the model shown in Figure 4.1, immobilized laccase molecules must be able to bind to a single isolated tVA linker protruding from the surface in order to achieve oriented immobilization resulting in DET to the enzymes' T1 copper center and subsequent ORR activity. The close linker arrangement in clusters shown here with a cluster size exceeding the dimension of the hydrophobic pocket of laccase is expected to result in low enzymatic activity.

4.1.2.2. Monolayers assembled from a thiol solution containing 4% water

An EC-STM image of the mixed SAM assembled from a thiol solution containing 4% H_2O is shown in Figure 4.5. An ordered hexagonal adlayer covers most of the surface. No phase separation has been found in all studies of this monolayer.

A high-resolution EC-STM image of the area marked by a blue square in Figure 4.5 reveals the structural details of the mixed thiol monolayer, which consists of a hexagonally arranged adlayer with high contrast and an additional substructure of lower contrast (see Figure 4.6A). The lattice parameter of the main high contrast structure is 0.9 nm. One high contrast feature together with the two closest low contrast features form a triangle. The distance between the single spots of the triangle is $\sim$0.3 nm, which is too close to identify them as individual molecules. A model for this arrangement is proposed in Figure 4.6B, where the three triangularly ordered features are assumed to belong to one tVA molecule. An upright orientation of the molecule with a slight tilt angle exposes the two methoxy groups and the carbonyl oxygen, where the highest electron densities have been calculated. In the high-resolution STM image, the methoxy group positioned at the longest distance from the surface appears as the brightest spot, while the second methoxy group and the carbonyl oxygen are imaged with a lower contrast. In the structure proposed here, each tVA molecule is surrounded by three MPA molecules that cause additional darker contrasts visible in the STM image. An overlay of the proposed thiol arrangement with the STM image shows that the positions agree very well (see Figure 4.6C). Differences in contrast between individual MPA features can be explained by the varying strength of hydrogen bonds between the carboxy group of MPA and the amide groups of tVA leading to different charge densities on the surface. The proposed arrangement of thiolate moieties on the Au(111) surface is depicted in Figure 4.6D. tVA sulfurs (green) are arranged in a hexagonal ($2\sqrt{3} \times 2\sqrt{3}$) unit cell with surrounding sulfurs from MPA molecules (purple) located at a distance of $\sqrt{3}\,a = 0.50$ nm. Similar to Figure 4.4, the resulting distances between nearest tVA molecules of 1.0 nm can be directly compared to the measured distances of 0.9 nm between the bright features and show an acceptable agreement. According to the proposed model, tVA molecules are oriented upright with a distance between nearest tVA molecules of 1.0 nm. Thus, the tVA linkers are widely separated in the structure as shown in Figures 4.5 and 4.6

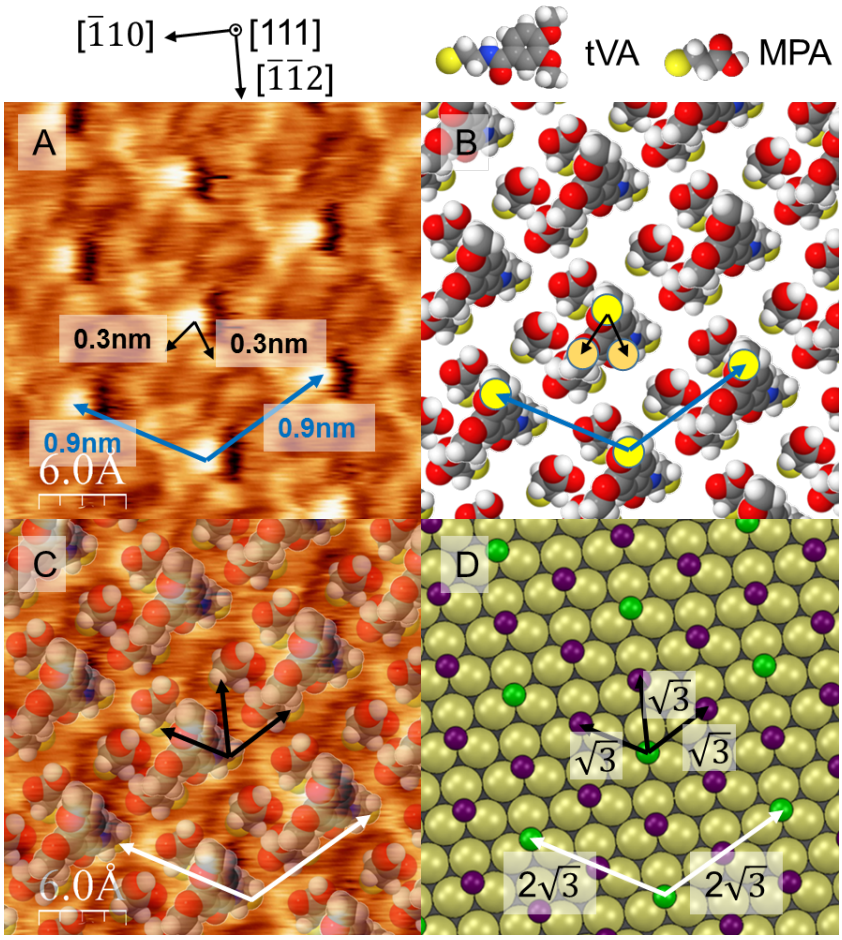

Figure 4.6.: (A) High resolution EC-STM image of the area marked by the blue square in Figure 4.5. The bright spots span a hexagonal pattern with dimensions of (0.9×0.9) nm^2. Imaging conditions: $E = 0.60\,\mathrm{V}$, $E_{\mathrm{tip}} = 0.40\,\mathrm{V}$, $I_{\mathrm{tun}} = 0.65\,\mathrm{nA}$, image size: (3×3) nm^2. (B) Model for the molecular arrangement of tVA and MPA molecules generating the contrast in A. (C) Molecular model overlayed on the STM image. (D) Arrangement of tVA (green) and MPA (violet) thiolates on Au(111).

when compared to their close packing in the structure of the pure tVA phase shown in Figure 4.4. This wide arrangement of the tVA linker molecules, which are more isolated and surrounded by shorter MPA diluent molecules, is supposed to allow for an immobilization of TvLc with the T1 copper center facing the tVA linker molecule. Thus, higher enzymatic activity is expected on this homogeneously mixed thiol monolayer compared to the phase separated monolayer.

In the following, the monolayers obtained from a tVA/MPA solution at a ratio of 1:99 and a H_2O content of 0% (Figures 4.2-4.4) and 4% (Figures 4.5,4.6) will be referred to as phase-separated and homogeneously mixed SAM, respectively.

4.1.3. Electrochemical activity measurements

According to the EC-STM investigations, monolayers assembled in thiol solutions of tVA and MPA at a ratio of 1:99 containing 0% (4%) water show phase separation (homogeneous mixing) of linker and diluent molecules. The catalytic activity of TvLc immobilized on the two SAMs towards ORR is examined with cyclic voltammetry. In case of DET to the T1 copper center of the enzyme and subsequent reduction of O_2 to H_2O, a cathodic current is expected at potentials negative of 0.8 V.

4.1.3.1. Enzymatic activity on the phase-separated and the homogeneously mixed monolayer

CVs of the enzyme-free electrodes show no cathodic currents between 0.3 V and 0.8 V in oxygen saturated electrolyte, only the charging current of the double layer is detected (see Figure 4.7A, black curve for the homogeneously mixed SAM, not shown for the phase-separated SAM). Hence, the monolayer itself does not show any catalytic background activity in the relevant potential window. With laccase immobilized on the homogeneously mixed SAM, negative currents are detected in oxygen–saturated electrolyte at potentials $\lesssim$ 0.8 V, while no currents are detected in an oxygen-free environment (see

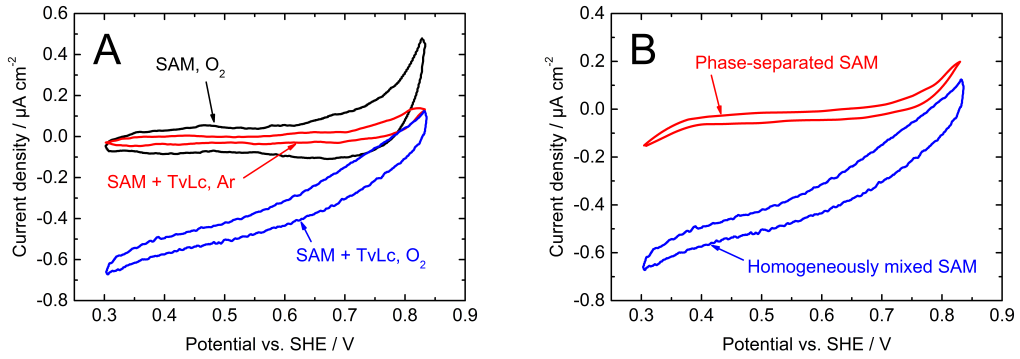

Figure 4.7.: (A) CVs of TvLc immobilized on the homogeneously mixed SAM on Au(111) in oxygen saturated (blue) and in Ar saturated McIlvaine buffer (red). The black curve shows the activity of the SAM without laccase in oxygen atmosphere. (B) CVs of TvLc immobilized on the homogeneously mixed SAM (blue) and the phase-separated SAM (red) on Au(111) in oxygen saturated solution. Scan rate: $1\,\mathrm{mV\,s^{-1}}$.

Figure 4.7A, blue and red curve). Thus, the currents can be assigned to enzymatic ORR activity. The second slight current increase at potentials negative of 0.40 V relates to electrocatalytic activity of enzymes that are immobilized with their trinuclear cluster close to the electrode surface.[104] At these potentials DET to the T2/T3 center leads to a conversion of O_2 to H_2O_2 instead of H_2O. This shows that not all enzymes immobilized on the surface are oriented with the T1 center facing the surface. Anodic currents at $\gtrsim 0.70\,\mathrm{V}$ are due to oxidative desorption processes of the thiol monolayer from the surface.[140] Thus, ORR activity has to be evaluated at potentials between 0.4 V and 0.7 V. In partially deaerated solutions, a redox peak couple is found at $E = 0.37\,\mathrm{V}$ (see Figure 4.8). Similar findings at potentials of $\sim$0.4 V have been reported previously and were assigned to oxidation and reduction of the T2 copper of laccase.[101, 104, 141]

A comparison of the electrocatalytic activities of TvLc immobilized on the homogeneously mixed and the phase-separated SAMs is depicted in Figure 4.7B. The molecularly mixed SAM shows a clear cathodic wave starting at $\sim 0.8\,\mathrm{V}$ that is assigned to enzy-

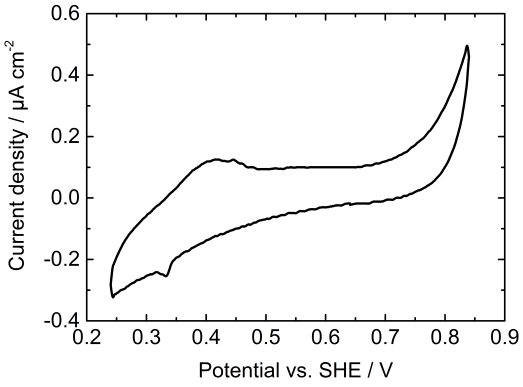

Figure 4.8.: CV of TvLc immobilized on homogeneously mixed tVA/MPA SAM on Au(111) in a partially deaerated electrolyte. A redox peak couple is visible at 0.37 V. Scan rate: $1\,\mathrm{mV\,s^{-1}}$.

matic ORR activity (blue curve). Current densities reach a value of $-0.58\,\mu\mathrm{A\,cm^{-2}}$ at a potential of 0.40 V. In case of the phase-separated monolayer, a cathodic wave is hardly visible (red curve). Current densities stay as low as $-0.06\,\mu\mathrm{A\,cm^{-2}}$ at 0.4 V, which is almost one order of magnitude lower than on the homogeneously mixed SAM. A current increase is only observed at potentials $< 0.4\,\mathrm{V}$, related to H_2O_2 formation, which occurs if the enzymes are immobilized with their trinuclear cluster close to the electrode as it is possible also for the phase-separated SAM. EC-STM images of the phase-separated SAM show that a considerable fraction of the surface consists of close-packed domains of tVA molecules ($\frac{1}{3}$) as well as of MPA domains ($\frac{2}{3}$). From the negligible enzymatic activity on this monolayer it is concluded that TvLc immobilization on domains of pure tVA or MPA does not result in an enzyme orientation suitable for DET to the T1 center. The observed differences in catalytic current do not originate from chemical modifications of the surface, but have to be related to differences in the molecular arrangement between the two SAMs. EC-STM data show that in the phase-separated SAM, tVA linkers are arranged in dense clusters with distances between individual molecules that are smaller than the size of the notch where the TvLc active center is located. Hence, an induced-fit binding between laccase and linkers is hindered, resulting in low enzymatic

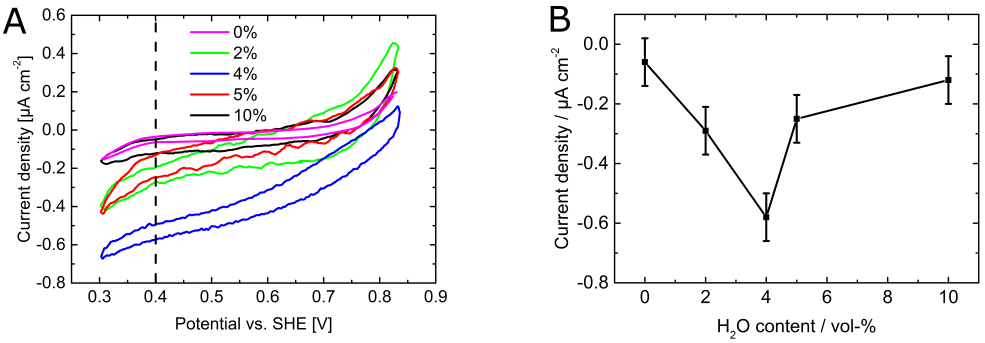

Figure 4.9.: (A) CVs of TvLc immobilized on SAMs assembled in thiol solutions with a water content between 0% and 10% and a fixed tVA:MPA ratio of 1:99. Measurements in oxygen saturated electrolyte at a scan rate of $1\,\mathrm{mV\,s^{-1}}$. (B) Current densities of the CVs in (A) at 0.4 V plotted versus the H_2O content in thiol solution.

activity. The homogeneous mixing of tVA and MPA in one phase results in an increased distance between neighboring tVA linker molecules of 1 nm. This is expected to allow for an enzyme immobilization via induced-fit binding in a proper orientation for DET to the T1 center and subsequent ORR bioelectrocatalysis as shown by electrochemical measurements.

4.1.3.2. Parameters for maximum enzymatic activity

Maximum activity on mixed tVA/MPA monolayers is determined by a parameter study of the ratio between tVA and MPA and of the H_2O content in solution during SAM formation. Figure 4.9A shows CVs of TvLc immobilized on monolayers formed from thiol solutions with different H_2O contents and a constant ratio of tVA:MPA of 1:99. Measurements are performed in oxygen saturated electrolyte at a scan rate of $1\,\mathrm{mV\,s^{-1}}$. For increased distinguishability, current densities at a potential of 0.4 V are plotted versus the water content in thiol solution in Figure 4.9B. The SAM assembled in a thiol solution with a water content of 4% exhibits the highest activity with a current density

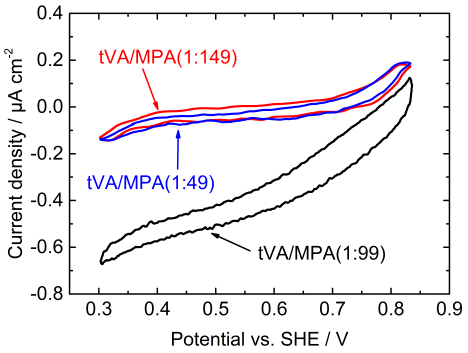

Figure 4.10.: CVs of Laccase immobilized on three different monolayers on Au(111) assembled in thiol solutions with tVA:MPA ratios of 1:49 (blue), 1:99 (black) and 1:149 (red) and a water content of 4%. All CVs have been measured in oxygen saturated electrolyte at a scan rate of $1\,\mathrm{mV\,s^{-1}}$.

of $-0.58\,\mu\mathrm{A\,cm^{-2}}$. Current density values decrease continuously to $-0.06\,\mu\mathrm{A\,cm^{-2}}$ and $-0.12\,\mu\mathrm{A\,cm^{-2}}$ for a water content of 0% and 10%, respectively.

The influence of the ratio between tVA and MPA is studied for three different monolayers assembled in thiol solutions with tVA:MPA ratios of 1:49, 1:99 and 1:149. The water content is kept constant at 4%. Figure 4.10 depicts a series of CVs of ORR at TvLc immobilized on these three monolayers. A dependency of electrocatalytic current on tVA:MPA ratios is clearly observed. The maximum activity of $-0.58\,\mu\mathrm{A\,cm^{-2}}$ for the SAM assembled from a solution with a ratio of 1:99 decreases to $-0.08\,\mu\mathrm{A\,cm^{-2}}$ for both ratios of 1:49 and 1:149. Hence, the parameter study shows highest enzymatic ORR current densities for the homogeneously mixed monolayer assembled in a thiol solution with a tVA:MPA ratio of 1:99 and a H_2O content of 4%. The maximum activity of $-0.58\,\mu\mathrm{A\,cm^{-2}}$ is lower than highest DET based ORR activities of high potential laccases on Au surfaces reported in literature, which are in the range of $25 - 40\,\mu\mathrm{A\,cm^{-2}}$.[30, 102, 108] The origin of this difference is analyzed in the following section.

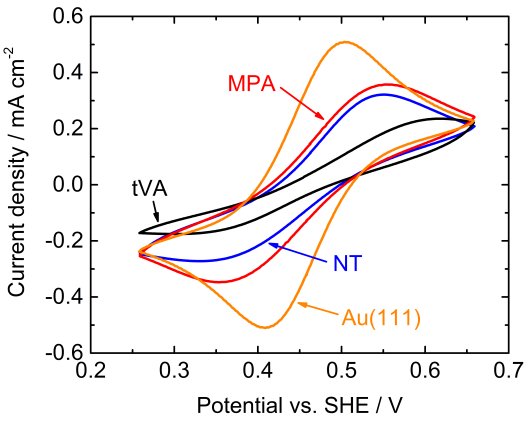

Figure 4.11.: CVs of MPA, NT and tVA SAMs on Au(111) and bare Au(111) in oxygen-free McIlvaine buffer pH 5 containing a hexacyanoferrate redox couple. Scan rate: 50 mV s^{-1}.

4.1.3.3. Comparison of enzymatic activity to literature data

A possible explanation for the two orders of magnitude difference between the herein obtained ORR current density compared to literature values is the different conductivity of the linkers used here (tVA) and in literature (anthracene-2-methanethiol [30], MPA [102] or an aryldiazonium derivative [108]). Electrochemical and EIS studies are performed on SAMs of tVA, MPA and an aromatic thiol, 2-naphthalenethiol (NT) without enzymes present in the solution to compare the conductivities of these species. 5 mM hexacyanoferrate(II/III) at a ratio of 1:1 is used as a redox probe to simulate the outer sphere electron transfer from the electrode to the enzyme under the assumption that the electron transfer process from the linker to the iron in the hexacyanoferrate is comparable to the one to the T1 Cu in the enzyme.

CVs of the three SAMs and bare Au(111) for comparison are shown in Figure 4.11. The only electrochemical activity visible in the graphs originates from the hexacyanoferrate redox couple with a formal redox potential of $E^0 = 0.45$ V. Peak current densities and peak separations for the different surfaces are collected in Table 4.1. tVA exhibits the lowest peak currents and highest peak separation of the three SAMs indicating that it is

Table 4.1.: Peak current densities j_p and peak separations ΔE_p for different thiol monolayers on Au(111) obtained from CVs shown in Figure 4.11.

Thiol	tVA	NT	MPA	Au(111)
j_p/mA cm^{-2}	0.24	0.32	0.36	0.51
ΔE_p/mV	320	220	200	95

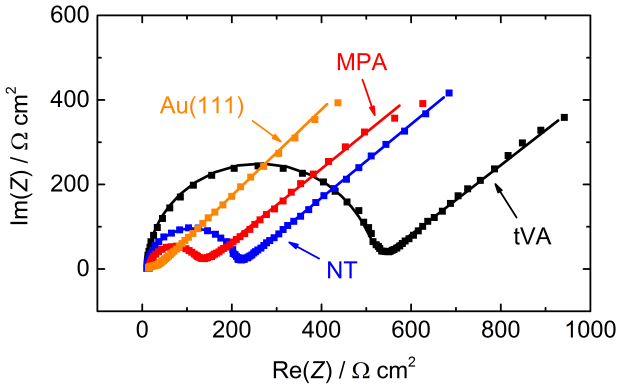

Figure 4.12.: Nyquist plot showing typical electrochemical impedance spectra of MPA, NT and tVA SAMs on Au(111) and bare Au(111).

the least active surface for the redox reaction and the reaction is less reversible than on the other surfaces. As expected, the activity and reversibility is highest on bare Au(111). In all cases, the peak separation is higher than the 59 mV expected from Equation (2.69) for a reversible one-electron reaction. This shows that for all the systems studied here the reaction is quasi-reversible or irreversible.

The charge transfer resistance R_{ct} of the different SAMs is studied by EIS in the same electrolyte. A static potential of $E = 0.45$ V is applied corresponding to the formal redox potential, where the redox reaction is in equilibrium. The amplitude of the AC potential is 5 mV. The resulting spectra together with fits according to a Randles equivalent circuit are shown in Figure 4.12 in the Nyquist representation. The extracted values for R_{ct} are summarized in Table 4.2. tVA clearly exhibits the highest R_{ct} of the three thiol

Table 4.2.: Charge transfer resistances R_{ct} for different thiol monolayers on Au(111) obtained from the fit to electrochemical impedance spectra.

Thiol	tVA	NT	MPA	Au(111)
$R_{ct}/\Omega\,cm^2$	520	186	92	21

linkers, which is in agreement with the CV results. This high resistance is considered one reason for the lower current densities observed in the present studies compared to literature data.

Another reason for the low current values obtained here is that not all enzymes are immobilized on the surface in an optimum way, which inhibits DET. As mentioned before, this can be explained by the maximum lateral distance between neighboring linker molecules of 1 nm, which is lower than the radius of TvLc. Hence, induced-fit enzyme immobilization on tVA is expected to be improved, but not optimal. This can be seen by the current density increase in the CVs of Figure 4.7 at potentials $< 0.4\,V$, which is attributed to enzymes that are immobilized on the surface in an orientation not suitable for DET to the T1 copper. Increasing the linker-linker distance could prove beneficial for oriented enzyme immobilization and enhanced biocatalytic currents.

4.1.4. Enzyme coverages on mixed monolayers

Apart from the previously discussed poor conductivity of the employed linker, also variations in enzyme coverage on the different SAMs might explain the obtained low current densities. Investigation of enzyme immobilization on the two SAM covered Au(111) surfaces studied with EC-STM in subsection 4.1.2 is carried out by means of EC-AFM, EC-STM and SECPM. The real enzyme coverage can be accessed with EC-AFM, since it images all enzymes, independent of their electrical contact to the SAM. EC-STM on the other hand, is sensitive to these enzymes only which have sufficient electrical contact to the surface/SAM to allow for efficient electron tunneling. As will be shown, only

the active enzymes can be imaged with EC-STM. Due to its expected importance in destruction free and sensitive imaging of biomolecules, particular attention will be devoted to SECPM, whose image contrast and resolution will be critically compared to EC-STM. Any features resolved in the enzyme structure could give an information on the orientation of TvLc molecules on the surface.

4.1.4.1. Electrochemical atomic force microscopy

Topographic EC-AFM images of enzyme coverages on the phase-separated and the homogeneously mixed SAM are shown in Figures 4.13A and B, respectively. In both images, a random distribution of spheres is observed that densely cover the surface and which are not visible before enzyme immobilization. From the particles' size distributions, an average lateral size of 8.2 nm and 9.4 nm is determined (see Figures 4.13C and D), which is wider than the average diameter $d = 5.5\,\text{nm}$ of TvLc known from crystallographic data.[90]

This discrepancy can be explained by the tip convolution effect (see subsection 2.6.3.3). According to Equation 2.93

$$x_{FWHM} = 2\sqrt{rd + \frac{d^2}{4}}, \qquad \text{(2.93 rev.)}$$

the FWHM values of 8.2 nm and 9.4 nm obtained with EC-AFM can stem from globular enzymes with a diameter of $d = 5.5\,\text{nm}$ if the surface is scanned with AFM tips with radii of $r = 1.7\,\text{nm}$ and 2.6 nm, respectively. These tip radii are close to the nominal tip radius $r = 2\,\text{nm}$ of the two different probes used to obtain topographic images in Figures 4.13A and B. This implies that the observed spheres can be identified as TvLc molecules and differences between the two images are in the range of deviations explicable by tip effects. In conclusion, both surfaces are densely covered with enzymes, differences in enzymatic activity due to different coverages can be excluded.

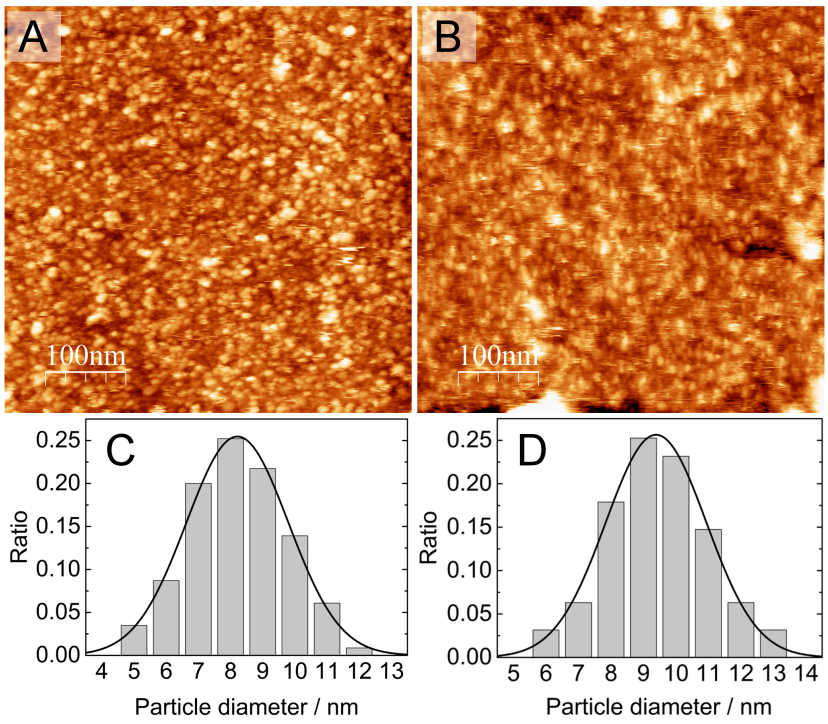

Figure 4.13.: Topographic EC-AFM images of laccase coverages on a (A) phase-separated and (B) homogeneously mixed SAM. Image sizes: (500×500) nm^2, $E = 0.7$ V. (C) and (D): Histograms of particle sizes obtained from the images in (A) and (B).

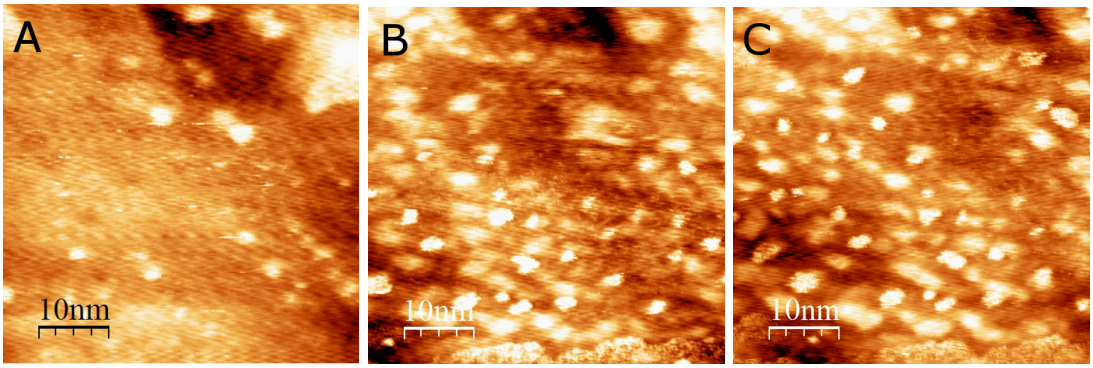

Figure 4.14.: Series of EC-STM images of a homogeneously mixed tVA/MPA monolayer covered with TvLc taken at potentials of (A) 0.75 V, (B) 0.70 V, and (C) 0.65 V. Imaging conditions: $E_{\mathrm{tip}} = 0.20\,\mathrm{V}$, $I_{\mathrm{tun}} = 0.1\,\mathrm{nA}$, image size: $(50 \times 50)\ \mathrm{nm}^2$.

4.1.4.2. Electrochemical scanning tunneling microscopy

EC-STM images of the homogeneously mixed monolayer covered with TvLc at potentials close to the OCP ($\sim$0.8 V) show only pitch holes typical for thiol SAMs. No difference to an enzyme-free electrode, i.e. no evidence of enzyme presence on the surface is observed. When the electrode potential is decreased to values where bioelectrocatalytic activity is visible in the CV, single bright spots start to appear at $E \approx 0.75\,\mathrm{V}$ (see Figure 4.14A). By further decreasing the potential, the amount of bright spots increases (see Figures 4.14B and C) until the surface is covered almost uniformly (see Figure 4.15A) at $E = 0.60\,\mathrm{V}$. On parts of the surface not covered with bright spots, step edges and pitch holes from the underlying surface are visible. On the same monolayer in the absence of enzymes (see Figures 4.5 and 4.6) and on the catalytically inactive phase-separated SAM covered with TvLc, no bright spots are observed in the potential range 0.60 - 0.80 V (see Figure 4.16).

A similar potential dependent EC-STM image contrast has been reported for a different laccase on buthanethiol modified Au(111).[102] It was further shown that purging the electrolyte with O_2 increased the image contrast while removing O_2 by purging with Ar resulted in a complete disappearance of the bright spots. The authors related this

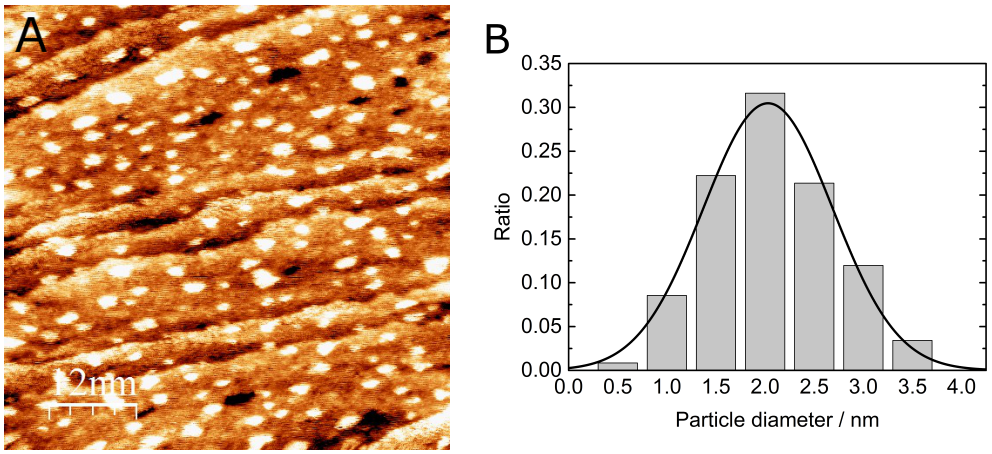

Figure 4.15.: (A) EC-STM images of TvLc immobilized on a homogeneously mixed tVA/MPA SAM. Imaging conditions: $E = 0.60\,\mathrm{V}$, $E_{\mathrm{tip}} = 0.20\,\mathrm{V}$, $I_{\mathrm{tun}} = 0.1\,\mathrm{nA}$, image size: $(60 \times 60)\ \mathrm{nm}^2$. (B) Histogram showing the particle size distribution in (A).

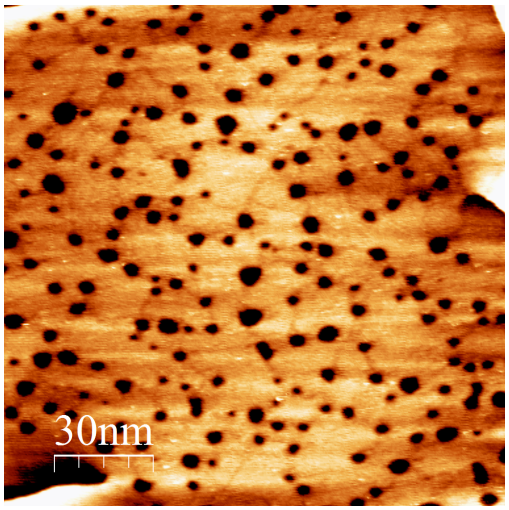

Figure 4.16.: EC-STM image of TvLc immobilized on a phase-separated tVA/MPA SAM. Imaging conditions: $E = 0.60\,\mathrm{V}$, $E_{\mathrm{tip}} = 0.20\,\mathrm{V}$, $I_{\mathrm{tun}} = 0.1\,\mathrm{nA}$, image size: $(150 \times 150)\ \mathrm{nm}^2$.

phenomenon to the enzyme's redox activity. A catalytically active enzyme exhibits a fast internal electron transfer pathway via an oxygen bridge between the T1 center and the trinuclear cluster in the peroxy and the native intermediate state (see subsection 2.5.2). In the absence of O_2 or at potentials where no enzymatic activity is observed, this internal electron transfer is hampered. Hence, electron tunneling via laccase molecules resulting in a visible image contrast from the enzymes is only possible if the biomolecules are catalytically active.

The average size of bright spots of 2.0 nm observed on the surface (see Figure 4.15B) is smaller than the diameter of TvLc, $d = 5.5\,\mathrm{nm}$. This can also be explained by the tunneling process described above. If electron tunneling proceeds only via the electrocatalytically active part of the enzyme, the outer protein shell not directly involved in the redox processes stays invisible to STM imaging. Thus, only a part of the enzyme is effectively observed. The size and intensity of the bright spots might give an information on the activity of the corresponding enzyme.

The enzyme coverage on the homogeneously mixed SAM at 0.6 V is found to be $\sim 3 \cdot 10^{-2}\,\mathrm{nm}^{-2}$. For laccase immobilization on a mixed tVA/buthanethiol SAM, a coverage of $286\,\mathrm{ng\,cm}^{-2}$ has been reported using surface plasmon resonance.[19] Using an enzyme weight of 57.6 kDa[142], the same enzyme number density of $3.0 \cdot 10^{-2}\,\mathrm{nm}^{-2}$ is obtained. This corresponds to 79% of the maximum coverage, a hexagonal packing of circles[143] with a diameter of 5.5 nm.

4.1.4.3. Scanning electrochemical potential microscopy

While the image contrast in EC-STM is found to be strongly dependent on electron transfer pathways through an enzyme and thus on enzyme activity on the surface, this limitation should not be present for SECPM. The feedback signal for SECPM imaging is the EDL potential of the surface, which, compared to the enzyme-free surface should be disturbed by the sheer presence of biomolecules on the surface, displacing ions from the

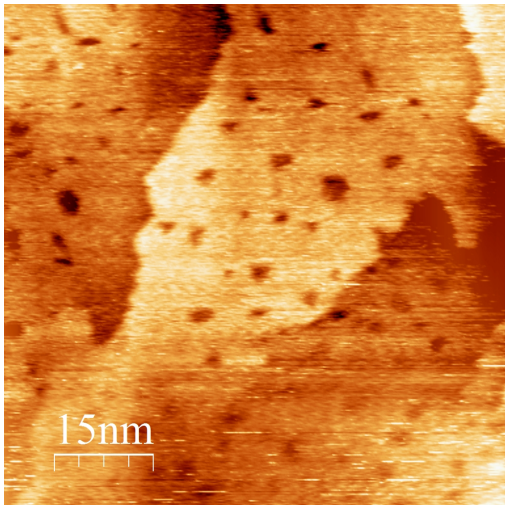

Figure 4.17.: SECPM image of a homogeneously mixed tVA/MPA monolayer covered with TvLc in the bioelectrocatalytically inactive potential range. Imaging conditions: $E = 0.80\,\mathrm{V}$, $\Delta E = 25\,\mathrm{mV}$, image size: $(75 \times 75)\ \mathrm{nm}^2$.

surface and changing the local permittivity. Baier et al. not only showed that imaging of biomolecules with SECPM is possible, but also achieved higher resolution when imaging these molecules with SECPM compared to EC-STM.[34]

In Figure 4.17, an SECPM image is shown of a homogeneously mixed tVA/MPA SAM with TvLc immobilized on the surface at a potential of $E = 0.80\,\mathrm{V}$, where no enzymatic activity is measured. Similar to EC-STM imaging, only dark pitch holes related to the thiol monolayer are observed, no features are visible that could be assigned to enzymes. By decreasing the potential applied to the electrode, an increasing number of bright spots becomes visible. At $E = 0.60\,\mathrm{V}$, the surface is densely covered (see Figure 4.18A) with a number density of $\sim 2.5 \cdot 10^{-2}\,\mathrm{nm}^{-2}$, similar to the EC-STM value. The average spot size observed with SECPM ($\sim 4\,\mathrm{nm}$) is higher than the value measured with EC-STM ($\sim 2\,\mathrm{nm}$). A closeup of TvLc molecules observed with EC-STM is compared to an image obtained with SECPM in Figure 4.19. The main difference between the two methods concerning imaging of laccase is the size of the observed biomolecules. Besides this size difference, the resolution achieved with SECPM is comparable to EC-STM, no

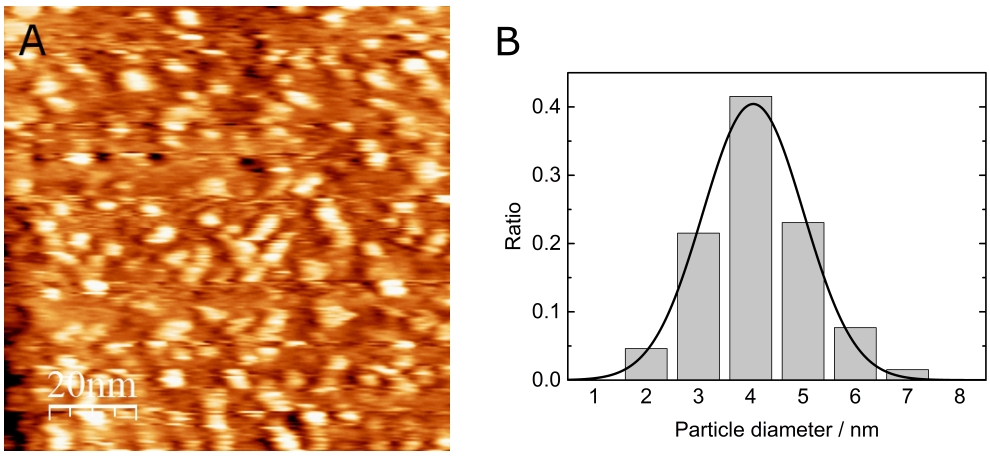

Figure 4.18.: (A) SECPM image of a homogeneously mixed tVA/MPA SAM covered with TvLc at a potential where enzymatic activity is observed. Imaging conditions: $E = 0.60\,\mathrm{V}$, $\Delta E = 25\,\mathrm{mV}$, image size: $(100 \times 100)\ \mathrm{nm}^2$. (B) Histogram showing the particle size distribution in (A).

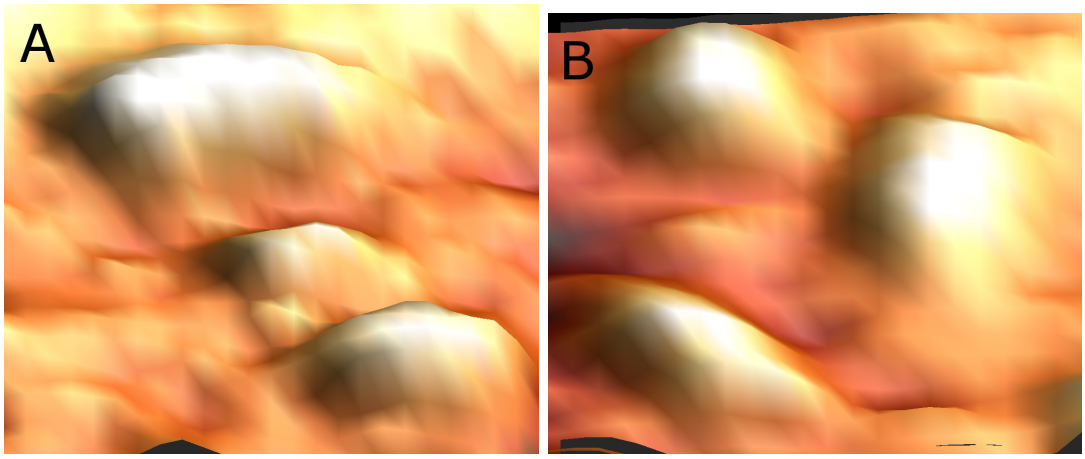

Figure 4.19.: 3D representation of (A) EC-STM and (B) SECPM closeups of TvLc molecules immobilized on a homogeneously mixed SAM in the potential range where enzyme activity is detected. Imaging conditions: $E = 0.60\,\mathrm{V}$, (A) $E_{\mathrm{tip}} = 0.20\,\mathrm{V}$, $I_{\mathrm{tun}} = 0.1\,\mathrm{nA}$, image size: $(6 \times 6)\ \mathrm{nm}^2$, (B) $\Delta E = 25\,\mathrm{mV}$, image size: $(19 \times 19)\ \mathrm{nm}^2$.

substructures in the biomolecule could be seen in all the measurements. The observations presented in this section indicate that there are common features in SECPM and EC-STM imaging which are difficult to explain by the current understanding of the SECPM technique. In order to gain a deeper understanding of the SECPM working principle, a more simplified system than the immobilized biomolecules imaged in this section is required. In the following section, SECPM studies are carried out on a model Cu(111) surface.

4.1.5. The ratio of active enzymes on the surface

The results presented in this section show a clear influence of the linker-linker separation on the activity of immobilized TvLc with current densities staying below values reported in literature. Lower enzyme coverages can be excluded as reason for reduced activities according to the EC-SPM investigations in subsection 4.1.4 that show fully covered surfaces. The lower current densities are partially explained by the higher charge transfer resistance of tVA compared to linkers used in previous studies (see subsection 4.1.3.3) and by the limited access of the enzymes' active centers to isolated tVA molecules, which causes that the enzymes are partially active only. This conclusion provokes the question on the ratio of active enzymes r_{active} in the immobilized layer. To determine r_{active}, it is necessary to compare the measured current density - voltage response $j_{\text{TvLc,meas}}(E)$ to the (only theoretically available) response of a fully active layer of TvLc $j_{\text{TvLc,theo}}(E)$ on the same surface:

$$r_{\text{active}} = \frac{j_{\text{TvLc,meas}}}{j_{\text{TvLc,theo}}}. \tag{4.1}$$

In the following, the $j_{\text{TvLc,theo}}(E)$ response of a fully active monolayer of TvLc during ORR is calculated assuming a Butler-Volmer behavior according to

$$j = j_0 \left(\exp\left(\frac{\alpha_{\text{a}} F (E - E^0)}{RT} \right) - \exp\left(-\frac{\alpha_{\text{c}} F (E - E^0)}{RT} \right) \right). \tag{2.50 rev.}$$

Three variables define the $j(E)$ behavior of an arbitrary reaction: the redox potential E^0, the exchange current density j_0 and the anodic/cathodic charge transfer coefficient $\alpha_{a/c}$. The model described here aims at obtaining values for these three parameters for a layer of active TvLc on the heterogeneous tVA/MPA SAM and at calculating the CV curve using (2.50).

The redox potential of TvLc is known as $E^0 = 780\,\mathrm{mV}$[144], which is in good agreement with the starting potential of the ORR reaction measured in the present study (see Figure 4.7). Electrochemical investigations of TvLc immobilized on roughened Au via anthracene-2-methanethiol show that an activation controlled current range with a cathodic charge transfer coefficient of $\alpha_c = 0.41$ exists.[30] This value shows that the one-electron transfer from the electrode surface to the enzyme's T1 center is the rate-determining step (RDS) for the TvLc ORR. As tVA is less conductive than anthracene-2-methanethiol, the same RDS is assumed here.

To obtain j_0, the enzyme's redox reaction is mimicked by using a redox couple. For this it is crucial to study a redox reaction with the same exchange current density $j_{0,\mathrm{redox}}$ as a fully active enzyme $j_{0,\mathrm{TvLc}}$ or at least to know the ratio between these two values $c_{\mathrm{ratio}} = \frac{j_{0,\mathrm{redox}}}{j_{0,\mathrm{TvLc}}}$. Ideally, the reaction path would go along the same energy levels in both cases.

If such a species is found, j_0 can be obtained by EIS at the redox potential E^0. The sinusoidal potential perturbation is then

$$E - E^0 = E_{\mathrm{amp}} \exp(i\omega t), \tag{4.2}$$

where the left hand side is equal to the overpotential $\eta = E - E^0$. The low amplitude $E_{\mathrm{amp}} = 5\,\mathrm{mV}$ used in EIS sets an upper limit for η, therefore the low-overvoltage approximation for the Butler-Volmer equation can be used:

$$j = j_0 \frac{nF\eta}{\nu RT}. \tag{2.56 rev.}$$

The electron transfer reaction at the T1 center is repeated four times to complete one enzyme catalyzed ORR reaction, hence $n = \nu = 4$, and

$$j = j_0 \frac{F\eta}{RT}. \tag{4.3}$$

By performing the EIS experiment at E^0, stationary currents can be eliminated, thus the following equality for the charge transfer resistance is valid:

$$R_{\mathrm{ct}} = \frac{\eta}{j}. \tag{4.4}$$

Combining (4.4) and (2.56) and rearranging yields:

$$j_{0,\mathrm{redox}} = \frac{RT}{FR_{\mathrm{ct}}}. \tag{4.5}$$

It is difficult to find a redox couple that mimics the redox reaction at the T1 center of laccase. There have been several attempts to synthesize a molecule complexing the T1 Cu with a structure similar to that of the enzyme,[145–147] but none of them was successful in reproducing key properties such as the high redox potential.

EIS showed that R_{ct} for a redox reaction on tVA is substantially larger than on the other linker covered surfaces studied in subsection 4.1.3.3. Under the assumption that R_{ct} mainly consists of the sum of the resistance for the electron transfer along the tVA molecule R_{tVA} and the redox reaction itself R_{redox}, it can be concluded from Table 4.2, that R_{ct} is dominated by R_{tVA}. In this case, the redox reaction and thus the redox species plays an inferior role for R_{ct}. According to (4.5), this is also true for $j_{0,\mathrm{redox}}$. Following the same argument in a similar way for the enzyme reaction means that $j_{0,\mathrm{TvLc}}$ is also dominated by R_{tVA}. Therefore, the parameter c_{ratio} becomes less important the

higher the influence of R_{tVA} is:

$$c_{\mathrm{ratio}} = \frac{j_{0,\mathrm{redox}}}{j_{0,\mathrm{TvLc}}} \approx \frac{R_{\mathrm{redox}} + R_{\mathrm{tVA}}}{R_{\mathrm{TvLc}} + R_{\mathrm{tVA}}} \to 1 \text{ for } R_{\mathrm{tVA}} \gg R_{\mathrm{redox}}, R_{\mathrm{TvLc}}. \tag{4.6}$$

Another important factor in the calculation of $j_{0,\mathrm{TvLc}}$ from $j_{0,\mathrm{redox}}$ is the ratio between the amount of redox couples and of enzymes reacting with the electrode surface. These values are available from the EC-SPM studies in subsection 4.1.4 and from the literature. EC-STM and SECPM images shown in subsection 4.1.4.2 and 4.1.4.3 reveal a consistent enzyme coverage of $\Gamma_{\mathrm{TvLc}} = 3 \cdot 10^{-2}\,\mathrm{nm}^{-2}$, in good agreement with surface plasmon resonance data.[19] According to the model presented in subsection 4.1.1, TvLc can exchange electrons with the surface via tVA molecules only, hence the redox couple reaction is investigated on a surface of pure tVA. In this case, the amount of reacting species is limited by the amount of tVA on the surface, i.e. it is independent of the surface coverage with redox couples Γ_{redox} and of their lateral size d if their coverage $\Gamma_{\mathrm{redox}} \gtrsim \Gamma_{\mathrm{tVA}}$ and $d_{\mathrm{redox}} \lesssim d_{\mathrm{tVA}}$. Phase 2 of the heterogeneous tVA/MPA monolayer studied in subsection 4.1.2, which consists of a pure tVA layer, yields $\Gamma_{\mathrm{tVA}} = 1.7\,\mathrm{nm}^{-2}$. Hence, j_0 obtained from the redox couple reaction according to (4.5) has to be rescaled by $c_{\mathrm{coverage}} = \frac{\Gamma_{\mathrm{tVA}}}{\Gamma_{\mathrm{TvLc}}}$ in order to obtain the exchange current density of TvLc on a tVA surface $j_{0,\mathrm{TvLc}}$.

Altogether, the enzyme exchange current density can be obtained from the redox couple $j_{0,\mathrm{redcouple}}$ via

$$j_{0,\mathrm{TvLc}} = c_{\mathrm{ratio}} c_{\mathrm{coverage}} j_{0,\mathrm{redcouple}} = c_{\mathrm{ratio}} \frac{\Gamma_{\mathrm{tVA}}}{\Gamma_{\mathrm{TvLc}}} \frac{RT}{FR_{\mathrm{ct}}}. \tag{4.7}$$

Inserting α, E^0 and $j_{0,\mathrm{TvLc}}$ into (2.50) yields the theoretical ORR Butler-Volmer curve for a fully active monolayer of TvLc on the mixed tVA/MPA SAM:

$$j_{\mathrm{TvLc,theo}} = -c_{\mathrm{ratio}} \frac{\Gamma_{\mathrm{tVA}}}{\Gamma_{\mathrm{TvLc}}} \frac{RT}{FR_{\mathrm{ct}}} \exp\left(-\frac{\alpha_{\mathrm{c}} F(E - E^0)}{RT}\right), \tag{4.8}$$

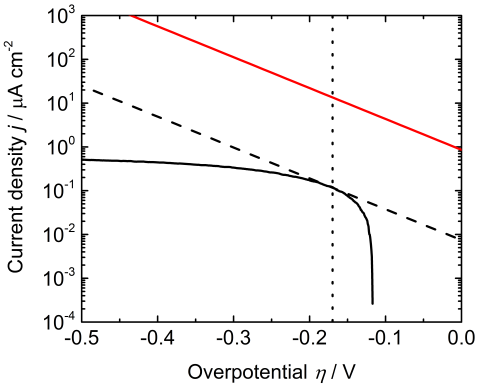

Figure 4.20.: Tafel plot of TvLc activity on the heterogeneously mixed tVA/MPA monolayer (solid black) and the theoretically obtained ORR curve of a fully active TvLc layer according to the model described in subsection 4.1.5 using $c_{\mathrm{ratio}} = 1$ in (4.8) (red). Dashed black line: fit to the measured curve with a slope of 144 mV/dec.

where for simplicity only the negative branch is considered. To obtain the ratio of active enzymes r_{active} according to (4.1), it is necessary to choose a potential range for $j_{\mathrm{TvLc,meas}}$, where the assumptions for the theoretical model are fulfilled at best, i.e. where the reaction is activation controlled. At higher potentials, the measured current density is influenced by anodic dissolution of the thiol monolayer and at lower potentials, the current is limited by mass transport effects (see subsection 4.1.3.1). A clear activation controlled potential range as indicated by a straight line in the Tafel plot is not observed for the TvLc measurements in this study (see Figure 4.20, black line). The $j_{\mathrm{TvLc,meas}}$ curve presented here is the average of the anodic and the cathodic scans of the blue curve shown in Figure 4.7. According to Ref. [30], $\alpha_{\mathrm{c}} = 0.41$, corresponding to a Tafel slope of 144 mV/dec. This slope (see Figure 4.20, dashed black line) is observed for $j_{\mathrm{TvLc,meas}}$ at $\eta = -0.17\,\mathrm{V}$. Assuming that $j_{\mathrm{TvLc,meas}}$ exhibits an activation controlled area, the corresponding potential range is just too limited to be observable in the Tafel plot, the adequate value for the measured curve is $j_{\mathrm{TvLc,meas}}(-0.17\,\mathrm{V}) = 0.12\,\mu\mathrm{A\,cm^{-2}}$. The theoretical curve for a fully active TvLc layer is determined from the hexacyanoferrate

redox couple studies in subsection 4.1.3.3 according to Equation 4.8 (see Figure 4.20, red line). The according current density value is $j_{\mathrm{TvLc,theo}}(-0.17\,\mathrm{V}) = 13.5\,\mu\mathrm{A\,cm^{-2}}$. Hence, the ratio of active enzymes is

$$r_{\mathrm{active}} = \frac{j_{\mathrm{TvLc,meas}}(-0.17\,\mathrm{V})}{j_{\mathrm{TvLc,theo}}(-0.17\,\mathrm{V})} = \frac{0.9\%}{c_{\mathrm{ratio}}}. \tag{4.9}$$

Taking the limit $c_{\mathrm{ratio}} \to 1$ as described in (4.6) yields $r_{\mathrm{active}} = 0.9\%$. This value allows to explain the two orders of magnitude difference in enzyme activity observed in the studies presented here in comparison to other studies [30, 102, 108] as discussed in subsection 4.1.3.3.

During the derivation of this model, it was assumed that R_{ct} is dominated by R_{tVA}, which allows to mimic the enzyme reaction by a redox couple like hexacyanoferrate. The fact that the value for r_{active} obtained from Equation 4.9 lies in the expected range indicates that the assumptions discussed here are, at least to a certain extent, fulfilled in the present system.

4.2. SECPM studies on Cu(111) surfaces

Several details of the SECPM working principle are still not understood as outlined in subsection 2.6.2 and subsection 4.1.4. Furthermore, although atomic resolution is expected to be achievable with this technique, no reports about atomically or molecularly resolved structures with dimensions lower than the size of an enzyme are found in literature. In this section, OH adsorbate layers on Cu(111), a surface well-studied with EC-STM, is chosen as a model substrate for SECPM imaging for two main reasons. First, the negative charge of the specifically adsorbed ions is expected to locally influence the EDL stronger than single atoms on an atomically flat surface. Second, the increased distance between next neighbors in an OH adsorbate layer should additionally facilitate imaging of individual ions with SECPM.

In subsection 4.2.1, high-resolution images of OH adsorption on Cu(111) surfaces obtained with SECPM are presented. In subsection 4.2.2, the origin of SECPM potentials is analyzed with a focus on leakage currents and electron tunneling. Two methods to determine leakage currents in this system are presented.

4.2.1. High-resolution imaging of the initial stages of Cu(111) oxidation with SECPM

Metallic Cu(111) is imaged with SECPM prior to anodic potential scans in the underpotential range of oxidation, where hydroxide adsorption takes place. Figure 4.21 depicts SECPM micrographs of metallic Cu(111) surfaces after reduction of the native oxide. Depending on the amount of native oxide, the surfaces show terraces with widths of several 100 nm or terraces of approximately 40 nm in width (see Figure 4.21A and B, respectively). The image quality of the metallic Cu surface is the same as that obtainable with EC-STM under the same conditions.[71, 72, 74] Figure 4.21B shows the typical hexagonal form of metallic Cu(111) terraces separated by monoatomic steps of (0.20 ± 0.04) nm in height. The measured terrace height is in agreement with the theo-

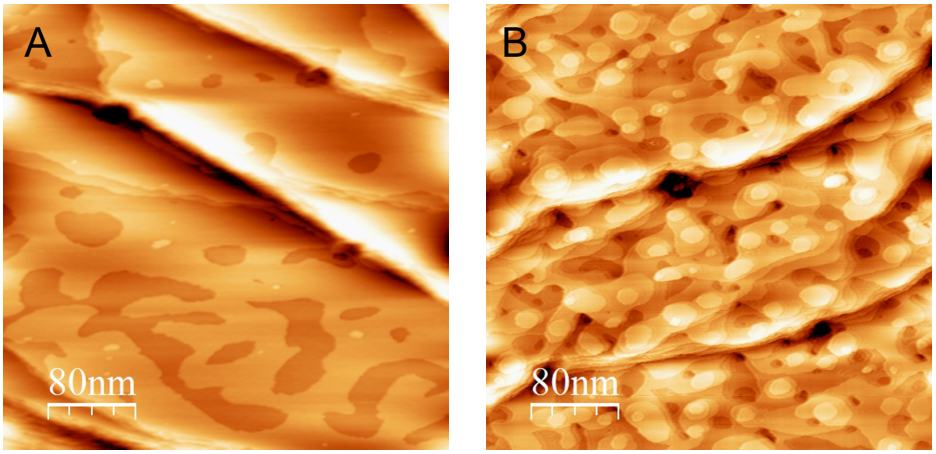

Figure 4.21.: Topographic SECPM images obtained on metallic Cu(111): A)$E = -0.89\,\mathrm{V}$, scan size: $(400\times400)\,\mathrm{nm}^2$, z range: $1.5\,\mathrm{nm}$, $\Delta E = 25\,\mathrm{mV}$; B) $E = -0.94\,\mathrm{V}$, scan size: $(400\times400)\,\mathrm{nm}^2$, z range: $2\,\mathrm{nm}$, $\Delta E = 25\,\mathrm{mV}$.

retical value of 0.209 nm[71] and is even more accurate than the value of $(0.26 \pm 0.03)\,\mathrm{nm}$ obtained from EC-STM studies.[74]

To probe the hydroxide adsorbate in the underpotential range of oxidation, the potential is gradually increased to $E = -0.65\,\mathrm{V}$ (see Figure 4.22). It is possible to follow the dynamics of OH layer formation with SECPM, even though the image quality is lower than that obtained in EC-STM experiments during the potential steps.[71–74] A OH desorption charge of $56\,\mu\mathrm{C\,cm}^{-2}$ is calculated from a CV measured after 19 min at a potential of $-0.65\,\mathrm{V}$ (see Figure 4.23). This corresponds to approximately 0.2 monolayers (ML) (0.2 $\mathrm{OH_{ad}}$ per Cu atom) of adsorbed hydroxide and is consistent with the literature.[72]

Figure 4.24 shows the OH adsorbate layer detected with SECPM, in high resolution, after a potential scan to $E = -0.68\,\mathrm{V}$. Its structure shows a hexagonal arrangement in different domains (see unit cells marked in Figure 4.24A). The structural parameter of $(0.60 \pm 0.04)\,\mathrm{nm}$ is in excellent agreement with the previously reported value of

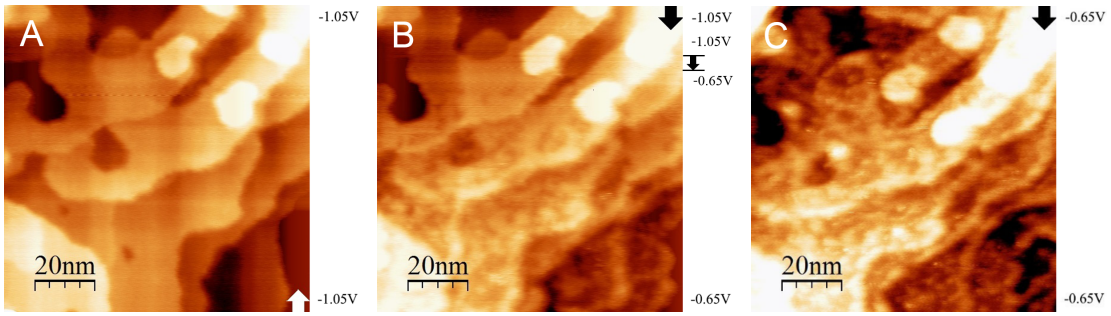

Figure 4.22.: Topographic SECPM images obtained on metallic Cu(111) A) prior to, B) during, and C) after the anodic potential sweep from -1.0 to $-0.65\,\mathrm{V}$; scan size: $(100 \times 100)\ \mathrm{nm}^2$, z range: $1\,\mathrm{nm}$, $\Delta E = 25\,\mathrm{mV}$, potential ramp rate: $20\,\mathrm{mV\,s^{-1}}$; scan directions are indicated by arrows.

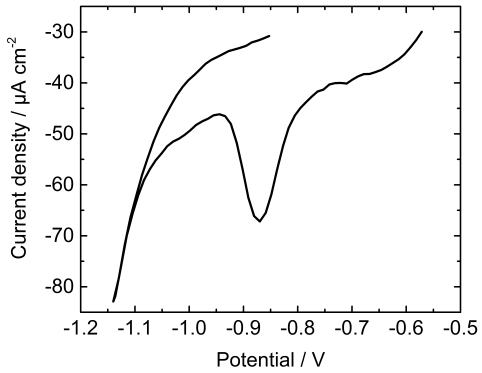

Figure 4.23.: Cyclic voltammogram showing the cathodic wave corresponding to the desorption of the OH monolayer adsorbed during the potential step in Figure 4.22B. Potential ramp rate: $20\,\mathrm{mV\,s^{-1}}$.

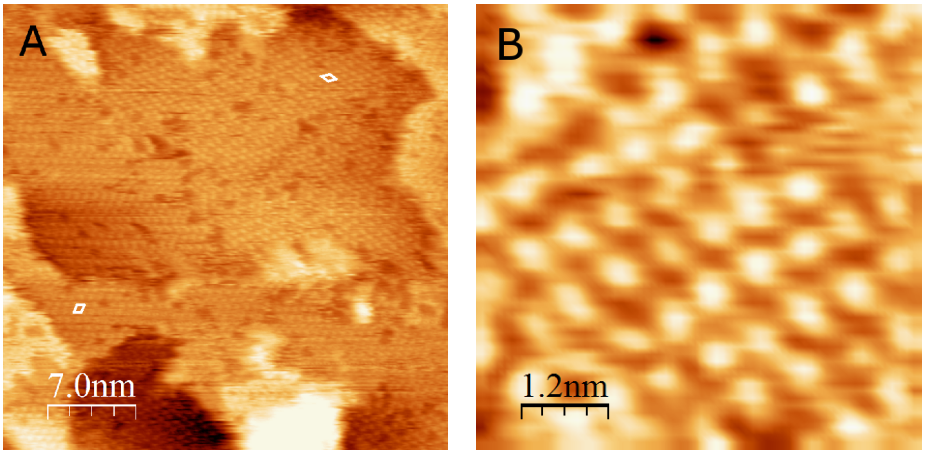

Figure 4.24.: Topographic SECPM images obtained on Cu(111) after a potential sweep from -1.0 to −0.68 V; A) scan size: (35×35) nm^2, z range: 0.6 nm, $\Delta E = 25$ mV; B) scan size: (6×6) nm^2, z range: 0.2 nm, $\Delta E = 25$ mV.

(0.60 ± 0.05) nm obtained with EC-STM.[72, 73] Dark vacancy islands are observed inside the OH adlayer, which are (0.09 ± 0.02) nm in depth and have a width of ≥ 0.6 nm.

These images demonstrate that SECPM can compete with the resolution achievable with EC-STM. On the other hand, the obvious similarity between images obtained with EC-STM and SECPM as shown here and in section 4.1 raises the question if there are similarities in the working principle of these two techniques. In the next section the origin of potentials measured with SECPM will be discussed in detail.

4.2.2. The origin of SECPM potentials

To analyze the origin of the potential value that is used as a feedback signal for imaging in constant-potential mode and its variation with surface topography, a potential-distance curve is recorded during approach of a sharp, insulated SECPM tip to the WE surface (see Figure 4.25A). It differs from the theoretical potential-distance curve in several points. At distances far away from the sample surface ($z_{\mathrm{tip}} > 1$ nm), the tip potential converges to a constant value of $E_{\mathrm{SECPM}} = -0.26$ V. This value is different from the OCP

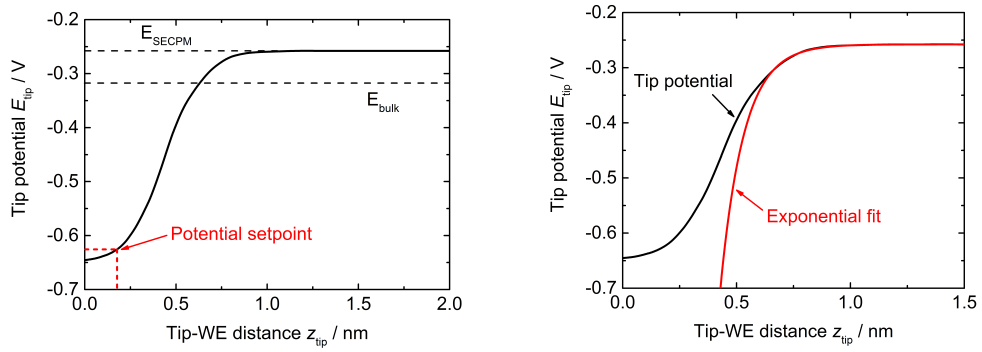

Figure 4.25.: (A) Potential distance curve of a sharp W SECPM tip in 0.1 M NaOH with an OCP of $E_{\mathrm{SECPM}} = -0.26\,\mathrm{V}$ and a WE potential of $E = -0.65\,\mathrm{V}$. The bulk OCP (E_{bulk}) of a non-insulated W wire (gray dashed line) is shown for comparison. The tip position for a SECPM potential set-point of $\Delta E = 25\,\mathrm{mV}$ used for imaging (Figures 4.21-4.24) is indicated by the dashed rectangle. B) Plot of the potential curve shown in A) (black) and exponential fit to the data for distances $z_{\mathrm{tip}} > 0.65\,\mathrm{nm}$.

of a W wire with a macroscopic surface area, $E_{\mathrm{OCP}} = -0.32\,\mathrm{V}$, the latter value being in agreement with literature data.[148] For different tips, E_{SECPM} values between -0.27 and $-0.1\,\mathrm{V}$ are found. The reason for this deviation is discussed below. At closer distances to the WE surface, the tip potential starts to bend towards the applied sample potential of $E = -0.65\,\mathrm{V}$. According to the GCS theory of the EDL, the potential behavior in this range should be exponential. At tip-WE distances $z_{\mathrm{tip}} > 0.65\,\mathrm{nm}$, the curve can be fitted with an exponential function (see Figure 4.25B). However, the characteristic Debye length obtained from this fit, $\lambda_{\mathrm{D,exp}} = 0.10\,\mathrm{nm}$ deviates from the theoretical value for 0.1 M NaOH, $\lambda_{\mathrm{D,theo}} = 0.96\,\mathrm{nm}$ (see subsection 2.1.2) by almost one order of magnitude. When the tip approaches the surface further, the potential does not decrease linearly, but, after an inflection point, it bends towards an offset value of $\Delta E = 5\,\mathrm{mV}$. This value is set as a minimum by the software to avoid direct contact between the tip and the sample surface. Similar sigmoidal SECPM profiles have been reported for flattened tip geometries.[126,127] In the present case of an extended tip with its non-insulated volume

extending completely through the double layer region in the z direction, the potential is measured at different positions between the tip apex and the boundary between the insulated and non-insulated area,[34] which should lead to the detection of an integral potential over the non-insulated area of the tip. In the EDL region, where the potential is z dependent, this integral signal is different from that at the tip apex; hence, even at closest tip-sample distances, it is not possible to measure the potential applied to the WE. This intuitive idea is supported by simulations by Hamou et al., which show that potential curves of extended tip geometries run more gradual compared to flattened probes and do not reach the WE potential at close gap distances.[128] Therefore, the profile measured with an extended tip as depicted in Figure 4.25A is unlikely to originate only from the double-layer potential of the working electrode, and must be influenced by additional processes. With a series of experiments, it is tried to gain insight in the processes determining the potential profile measured with SECPM (Figure 4.25A) to better understand the meaning of the topographic images shown in Figures 4.21-4.24.

4.2.2.1. Leakage current transport mechanisms and direct determination of leakage currents

The potential set-point used for SECPM imaging in the present work ($\Delta E = 25\,\mathrm{mV}$) is indicated by the dashed red rectangle in Figure 4.25A. The tip-WE distance at this set-point, according to the graph, is $z_{\mathrm{tip}} = 0.18\,\mathrm{nm}$. To understand the image contrast in the $x - y$ SECPM micrographs, processes that influence the measured potential profile at the position of the tip during imaging have to be identified. An important parameter that is studied in the context of this section is the leakage current, I_{SECPM}, present in the SECPM setup. Leakage currents originate from the input current of the operational amplifier, imperfect insulations, and leakages on the printed circuit board. To close the electrical circuit, these currents need to be transported between the tip and the WE during SECPM experiments. I_{SECPM} is measured with the help of a resistor R that is

clamped between the tip holder and the WE sample holder, which is connected to the ground potential in the SECPM setup. For this experiment, the tip is not in contact with the electrolyte and positioned far away from the surface; therefore, leakage currents can exclusively be transported by the resistor. In SECPM mode, the operational amplifier reads the potential drop E_{R} across the resistor, which can be converted to the leakage current by using $I_{\mathrm{SECPM}} = \frac{E_{\mathrm{R}}}{R}$. Typical values are $0.5 - 30\,\mathrm{pA}$. For the timescale of the potential-distance measurements and the surface scans presented herein (∼hours), the leakage currents are found to be constant. The flux of electrons is directed from the WE to the tip holder. In the SECPM system, leakage currents I_{SECPM} have to be transported by processes taking place in the electrochemical cell of the microscope, according to:

$$I_{\mathrm{SECPM}} = I_{\mathrm{Faraday}} + I_{\mathrm{tunnel}} + I_{\mathrm{misc}}, \tag{4.10}$$

where I_{Faraday} is the electrochemical current caused by faradaic processes, I_{tunnel} is the tunneling current, and I_{misc} represents non-faradaic currents occurring in the electrochemical cell. The predominant process is determined by its resistivity at the corresponding tip position relative to the WE surface. Owing to the exponential distance dependency of the tunneling resistance, electronic tunneling prevails at lower gap distances up to a few nanometers.[149] At large tip distances from the WE surface ($z_{\mathrm{tip}} > 1 - 2\,\mathrm{nm}$), the leakage current is transported by faradaic processes in the electrolyte (I_{Faraday}). Processes occurring in the intermediate region of z_{tip} are difficult to determine as they might not only be a combination of tunneling processes and faradaic currents, but also include effects such as overlapping of the two double layers and capacitive charging.

4.2.2.2. Electron tunneling at close distances

To study the effect of leakage-current transport via electron tunneling on the tip potential at small tip-WE distances, the working principle of SECPM with presence of leakage currents is compared to that of an EC-STM. In an EC-STM experiment, a constant

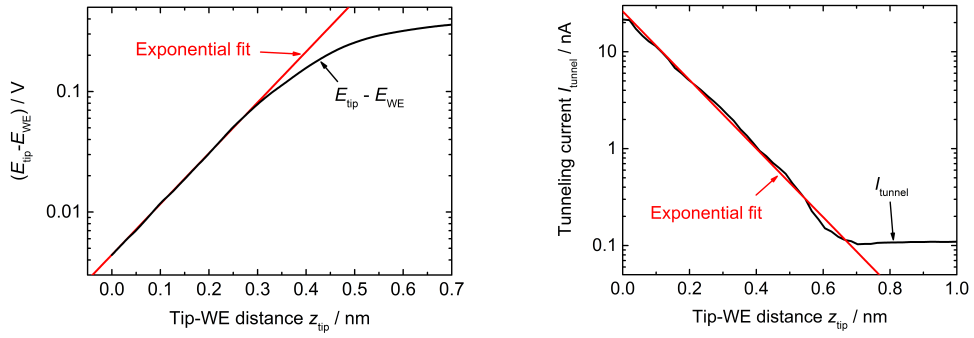

Figure 4.26.: A) Semi-logarithmic plot of the potential data shown in Figure 4.25 (black) and exponential fit to the data between 0 and 0.29 nm (red). B) Semi-logarithmic plot of a current-distance curve measured with a sharp insulated W tip in 0.1 M NaOH in EC-STM mode (black) and exponential fit to the data between 0 and 0.7 nm (red).

bias voltage is applied between the tip and the WE, $E_{\text{bias}} = E_{\text{tip}} - E_{\text{WE}}$. As has been deduced in subsection 2.6.1, the resulting tunneling current is:

$$I_{\text{tunnel}} \propto E_{\text{bias}} \cdot \mathrm{e}^{-1.025\sqrt{\phi}\cdot z_{\text{tip}}}, \qquad (2.89 \text{ rev.})$$

where ϕ is the tunneling barrier height in eV and z_{tip} is the tip-WE distance in Å. In SECPM mode at short distances, the tunneling current is equal to the constant leakage current present in the system, $I_{\text{tunnel}} = I_{\text{SECPM}}$. Equation (2.89) can thus be rewritten as:

$$E_{\text{bias}} \propto I_{\text{tunnel}} \cdot \mathrm{e}^{1.025\sqrt{\phi}\cdot z_{\text{tip}}}. \qquad (4.11)$$

In Figure 4.26, a semi-logarithmic plot of $(E_{\text{tip}} - E_{\text{WE}})$ as a function of the tip-WE gap distance z_{tip} is shown. Between 0 and 0.29 nm, the curve can be fitted with a linear function, which means that there is an exponential dependence of $E_{\text{tip}} - E_{\text{WE}}$ on the gap between the tip and the surface, as predicted by equation (4.11). This finding is consistent with the literature, where an exponential relationship between bias voltage and gap distance at constant tunneling currents has been reported previously.[118] From

the regression curve, according to equation (4.11), a tunnel barrier height $\phi = 0.90\,\mathrm{eV}$ is found for the data shown here. For comparison, a current-distance curve is recorded in EC-STM mode with the same tip (see Figure 4.26B). An exponential fit according to (2.89) in the range 0 to 0.9 nm yields a tunnel barrier of $\phi = 0.89\,\mathrm{eV}$, in excellent agreement with the value obtained from the potential-distance curve. Tunnel barriers obtained for other, identically prepared, W tips are in the range of 0.80 to 1.23 eV. These values are well in the range of parameters reported in the literature (see, e.g. Ref. [118, 150] and references therein). On close examination, one can see that the current-distance curve does not exactly follow the exponential fit, but shows a weak oscillating behavior around the red curve (see Figure 4.26B). Such a phenomenon has been reported in literature and was assigned to different layers of H_2O molecules in the EDL that are passed by the tip while approaching the surface.[150] An oscillating behavior similar to the current-distance curve in Figure 4.26B, which shows one single approach curve is not visible in Figure 4.26A. The potential-distance curve depicted there is an average of 52 approach curves, hence oscillations are lost on averaging. In addition, potential-distance curves were by far more perturbed by noise than current-distance curves, which makes the averaging necessary. Any oscillating features are mostly hidden in the noise.

4.2.2.3. Faradaic processes at longer distances and indirect determination of leakage currents

At increasing distances, where the tunneling impedance becomes similar to the faradaic impedance, the curve shape deviates from an exponential tunneling behavior as the leakage current is expected to flow partially through tunneling and electrochemical processes. With increasing distance, and hence increasing ratio of faradaic to tunneling currents, this leads to a convergence of the tip potential towards E_{SECPM}.

Electrochemical processes on the W tip surface at tip distances far away from the WE surface, where faradaic processes are prevailing, are determined by the current-voltage

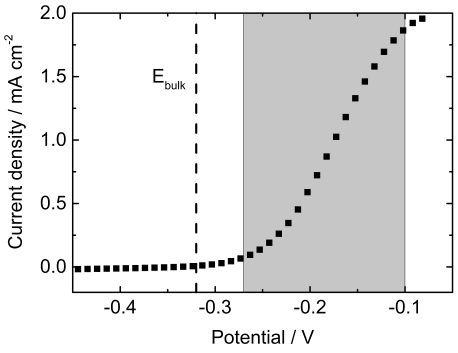

Figure 4.27.: CV of a W wire in 0.1 M NaOH. The OCP is indicated by a dashed line. The anodic potential range, where stable tip potentials E_{SECPM} have been measured, is highlighted in gray. Ramp rate: $50\,\mu V\,s^{-1}$, potential step size: 10 mV.

interdependence of W in 0.1 M NaOH, as depicted in approximation by the CV shown in Figure 4.27. The OCP is reached after $30 - 40$ min stabilization, resulting in a value of $E_{\mathrm{bulk}} = -0.32$ V, as indicated by the dashed line. This OCP corresponds to a corrosion or mixed potential where the cathodic currents are caused by oxygen reduction to water, and anodic currents originate from W oxidation and dissolution through multistep reactions.[148,151–154] The potential region between -0.27 and -0.10 V, where stable values of SECPM tip potential E_{SECPM} are found (see Figure 4.25A), is highlighted in gray. All E_{SECPM} values are located in the anodic current region, that is, oxidative processes prevail at the tip surface, and thus the electron flux is directed from the electrochemical interface between electrolyte and tip to the STM microscope head. This observation is in accordance with the direct leakage-current measurements mentioned above. The origin of these faradaic processes at the tip is, therefore, assumed to be the constant leakage current I_{SECPM} in the system. The non-insulated area A of a coated SECPM tip exposed to the electrolyte is different for every tip, and current densities j should therefore vary according to:

$$j = \frac{I_{\mathrm{SECPM}}}{A} \tag{4.12}$$

The tip-dependent current densities can be related to overpotentials by the W CV shown in Figure 4.27. The reason for variations in E_{SECPM} is the constant I_{SECPM} flowing through the non-insulated surface area of the tips, which differs for different tips. The larger the non-insulated surface area of the tip, the lower the leakage current density and the smaller the overpotential.

The Multimode instrument used for the present experiments allows for changes between potential measurement in SECPM mode and current measurements at an applied bias voltage in EC-STM mode, using an analog switch, which connects the tip with the potentiometer and potentiostat, respectively, thus without changing the electrochemical setup. This possibility is used to estimate the leakage currents in the SECPM setup that are considered responsible for imaging in SECPM mode. In EC-STM mode, the electrochemical tip current measured far away from the WE surface is proportional to the free-tip area A by $I_{\mathrm{STM}} = j \cdot A$. To determine A, the electrochemical currents I_{STM} are measured for different tips in STM mode at an applied tip potential of $E = -0.20\,\mathrm{V}$, and thus, at a constant current density $j_{-0.20\,\mathrm{V}}$. From Figure 4.27, a value of $j_{-0.20\,\mathrm{V}} = 0.62\,\mathrm{mA\,cm^{-2}}$ is obtained. It has to be mentioned that the anodic regime of the W CV is influenced by diffusion at potentials $E > -0.17\,\mathrm{V}$. Diffusion limitation is different at extended surfaces such as the W wire used for the CV measurement in Figure 4.27 and the STM tips, because on smaller electrodes, mass transport normalized to the unit area of the electrode is faster. Electrochemical reactions that take place at $-0.20\,\mathrm{V}$ are mainly kinetically controlled (for detailed analysis of the errors introduced by this method, see below); therefore, the assumption of constant current density at $E = -0.20\,\mathrm{V}$, regardless electrode size, is reasonable. Hence:

$$A = \frac{I_{\mathrm{STM}}}{j_{-0.20\,\mathrm{V}}} \tag{4.13}$$

Surface areas determined with this method are in the range of 0.82 to $2.1 \cdot 10^3\,\mu m^2$ for I_{STM} values, detected in the studies presented here, between 5.1 pA and 12.8 nA. Combining equations (4.12) and (4.13) leads to:

$$\frac{1}{I_{STM}} = \frac{j}{I_{SECPM} \cdot j_{-0.20\,V}} \tag{4.14}$$

The relation between electrochemical current density j and electrode potential E for the oxidation and dissolution of W in basic media has been reported to follow a Tafel-like behavior between -0.30 and $-0.05\,V$:[148]

$$j = j_{corr} \cdot e^{(E-E_{bulk})/\beta}, \tag{4.15}$$

where j_{corr} is the corrosion current density at the OCP and $\beta = \frac{RT}{\alpha_a F}$ is the anodic Tafel coefficient.

Inserting equation (4.15) into (4.14) results in:

$$\frac{1}{I_{STM}} = a \cdot e^{(E-E_{bulk})/\beta} \tag{4.16}$$

with a constant $a = \frac{j_{corr}}{I_{SECPM} \cdot j_{-0.20\,V}}$. In the nanoscopic system, the working electrode is the tungsten tip, thus $E = E_{SECPM}$. The leakage current can be determined from a:

$$I_{SECPM} = \frac{j_{corr}}{a \cdot j_{-0.20\,V}}. \tag{4.17}$$

The parameter a is determined from a semi-logarithmic plot of I_{STM}^{-1} versus E_{SECPM} according to equation (4.16) for four different sets of tips, where each data point corresponds to a different tip. For each data point in Figure 4.28, the electrochemical current I_{STM} for a single tip, determined in STM mode at an applied tip potential of $E = -0.20\,V$, is plotted versus the tip potential E_{SECPM} of the same tip obtained in SECPM mode far away from the electrode. Variation of I_{STM}^{-1} for each set of tips (1-4)

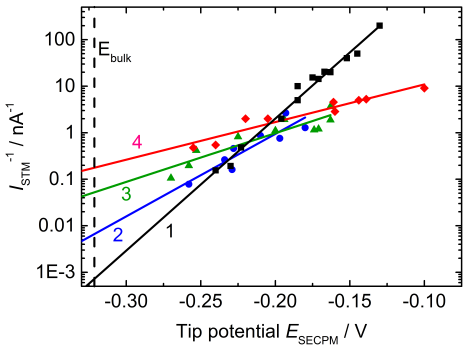

Figure 4.28.: Semi-logarithmic plot of I_{STM}^{-1} versus tip potential for four different sets of W tips (data points) and linear fits to each set. The dashed line indicates $E_{\mathrm{bulk}} = -0.32\,\mathrm{V}$ of W.

corresponds to a variation in active surface area A, according to equation (4.13). Each set was measured on a different day; therefore, the leakage currents are expected to differ between each set. Straight lines are fitted to the data according to equation (4.16). Each set of data points can be approximated by a linear curve, which means that the electrochemical reaction is activation controlled by one rate-determining step over the whole range of potentials. Values for the Tafel coefficient β obtained by the fits are in the 0.015 - 0.053 V range, as shown in Table 4.3, with a mean value of $\beta = 0.033\,\mathrm{V}$. The reason for this variation could be the different oxidation states of the individual tip sets caused by aging before they are immersed into the electrolyte. If different oxide-layer thicknesses, compositions, or structures influence the rate-determining reaction taking place at the interface, the Tafel coefficient can also change. The constant a is found by extrapolating the regression curve to $E_{\mathrm{bulk}} = -0.32\,\mathrm{V}$ according to equation (4.16), and the resulting values are between $7.9 \cdot 10^{-4}$ and $0.18\,\mathrm{nA}^{-1}$.

To obtain the current density j_{corr} at the OCP, the electrochemical behavior of W is depicted in the Tafel plot in Figure 4.29. The black curve shows the data of Figure 4.27, where a linear activation-controlled behavior is hardly achieved. This is in contrast to studies by Heumann et al.,[148] where linearity is reported over a potential range of

Table 4.3.: Tafel coefficients β and leakage currents I_{SECPM} obtained from the four data sets of Figure 4.28, according to Equations (4.16) and (4.17).

Data set	β / V	I_{SECPM} / nA
1	0.015	32
2	0.024	3.6
3	0.041	0.47
4	0.053	0.18

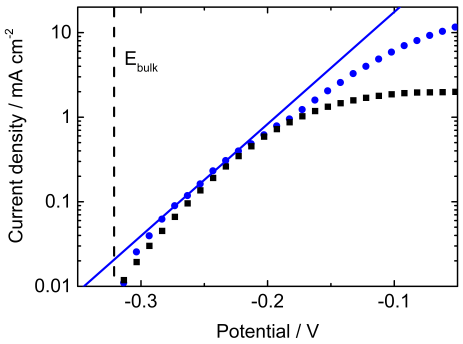

Figure 4.29.: Tafel plots of W in 0.1 M NaOH without (black squares, from Figure 4.27) and with stirring (blue circles) of the solution. The solid blue line represents a linear fit to the blue data points in the potential range between -0.28 and −0.22 V. The bulk OCP is indicated by a dashed line. Ramp rate: 50 µV s^{-1}, potential step size: 10 mV.

100 mV. According to the present data, the curve quickly approaches a plateau, indicating a process limited by diffusion of reactants to, or from, the interface. The situation resembles the etching process of W STM tips through anodic dissolution,[155] where the electrochemical current is mainly limited by two processes, which are the transport of hydroxide to the wire and a shielding of the wire caused by dissolved tungstates. In the case of a W wire vertically dipped into solution, as is also the case in the experiments shown here, the electrode is partially blocked by the flow of tungstate ions down the wire. Similar processes are considered responsible for the current limitation into a diffusion-controlled regime at relatively low potentials.

To improve access of reactants to the electrode, the electrolyte solution is stirred during the experiment. The resulting current densities (see Figure 4.29, blue circles) are generally higher than in the non-stirred case, and the current decay towards a plateau is slower and occurs at higher potentials. Between -0.28 and $-0.22\,\mathrm{V}$, a linear trend is visible, and a linear regression gives a Tafel coefficient of $\beta = 0.033\,\mathrm{V}$, which is in good agreement with the literature value of $\beta = 0.035\,\mathrm{V}$.[148] The current density at $E_{\mathrm{bulk}} = -0.32\,\mathrm{V}$ obtained from a linear fit is $j_{\mathrm{corr}} = 21\,\mu\mathrm{A\,cm^{-2}}$, and at $E = -0.20\,\mathrm{V}$, a current density value of $j_{-0.20\,\mathrm{V}} = 0.62\,\mathrm{mA\,cm^{-2}}$ is measured. These current density values are higher than those reported in the literature, which is most likely because of the unknown roughness of the W wire used in the experiments presented here, as current densities are calculated by using the geometric surface area. For the calculation of I_{SECPM}, the ratio of j_{corr} and $j_{-0.20\,\mathrm{V}}$ is taken, which is independent of the area. Thus errors attributed to the roughness are negligible. Figure 4.29 shows that $j_{-0.20\,\mathrm{V}}$ is below the Tafel line, indicating that diffusion processes limit the reaction rate at this potential. A comparison with the current density obtained from the Tafel equation shows that the measured value of $j_{-0.20\,\mathrm{V}}$ is 18% below the expected value without diffusion limitation, $j_{-0.20\,\mathrm{V,\,Tafel}} = 0.76\,\mathrm{mA\,cm^{-2}}$. Values for I_{SECPM} are calculated according to equation (4.17) assuming the same value for $j_{-0.20\,\mathrm{V}}$ for microscopic and macroscopic

systems. Unlike the macroscopic system, the microscopic system is not diffusion limited (see Figure 4.28), thus the error of 18% is directly taken over. This error is acceptable for the goal of this work, which is to estimate leakage currents present in the SECPM system. The resulting values are listed in Table 4.3.

The I_{SECPM} values obtained from data sets 2-4 are in the typical range of tunneling currents used in EC-STM. Data set 1 yields $I_{\mathrm{SECPM}} = 32\,\mathrm{nA}$, which is unusually high. The reason is most likely the divergence of the Tafel coefficient, $\beta = 0.015\,\mathrm{V}$, obtained for this data set from the one from the CV, $\beta = 0.035\,\mathrm{V}$, thus indicating different electrochemical processes at the microscopic tip surface and the macroscopic wire surface. β is inversely proportional to the slope of the Tafel function. Hence, the extrapolation of the steep Tafel function of data set 1 leads to a lower value of a and, according to equation (4.17), to an overestimation of the leakage current. A similar argument should hold in the opposite way for data set 4, with a high value of $\beta = 0.053\,\mathrm{V}$, leading to an underestimation of the leakage current obtained from this measurement. Tafel coefficients obtained from data sets 2 and 3 are close to the values from the CV; therefore, reactions at the microscopic and macroscopic surface are considered equal and the two current values are assumed to be in the correct range.

The results presented here show that it is possible to determine leakage currents flowing in the SECPM system I_{SECPM} from the electrochemical behavior of the W tips in the Faraday regime of the potential-distance curve. Leakage current values determined in situ with electrochemical methods (ca. 1 nA) are 2-3 orders of magnitude higher than those measured ex situ by using a resistor ($< 1 - 30\,\mathrm{pA}$). A possible explanation for this could be thin fluid films moistening the tip and tip holder while the tip is in contact with electrolyte, thus increasing leakage currents to the tip. In conclusion, the magnitude of the leakage current is considered independent of the transport mechanism between the tip and the surface; hence, the same current is responsible for the potential drop at the tip in the tunneling regime according to Equation (4.11).

Another important factor to discuss is tip dissolution owing to electrochemical processes occurring at the tip surface at anodic potentials and the resulting size reduction. It has already been discussed that the tunneling impedance is negligible compared to electrochemical impedances at tip-WE distances typically used for imaging in SECPM mode. Hence, leakage currents are only transported by electron tunneling if the tip is approached to the WE without inducing electrochemical modifications at the tip surface.

For the electrochemical measurements used to determine leakage currents, tip potentials between -0.27 and $-0.1\,\mathrm{V}$ are measured, corresponding to current densities between 0.10 and $12.9\,\mathrm{mA\,cm^{-2}}$. Higher current densities are obtained for smaller free tip surface areas and vice versa. The percentage error in the measurement, owing to anodic dissolution, corresponds to a relative change in tip surface and, the smaller the tip surface and the higher the faradaic current density, the higher the percentage error is expected to be. Hence, if the anodic tip dissolution changes the free tip surface, a deviation from the ideal Tafel behavior is expected in the plot of Figure 4.28 for higher values of I_{STM}^{-1} (corresponding to smaller tip surfaces according to equation (4.13)) and higher values of E_{SECPM} (corresponding to higher current densities according to equation (4.15)). As no deviation from the linear behavior is observed at these data points, it is concluded that the tip surface is not significantly modified.

SECPM imaging is usually performed at small potential set-points.[34,131] All SECPM images presented in this work are recorded at potential set-points of $\Delta E = 25\,\mathrm{mV}$, that is, with the tip potential very close to the WE potential. To estimate the real tip-WE distance, the origin of the zero point on the z_{tip} axis of Figure 4.25 has to be studied further. As mentioned above, it is determined by the minimum possible set-point of $\Delta E = 5\,\mathrm{mV}$ in the SECPM system. The real voltage E_{c} between tip and WE at the contact point is determined by the contact conductance $G_{\mathrm{c}} = \frac{I_{\mathrm{tunnel}}}{E_{\mathrm{c}}}$. For the tunneling contact between a W tip and a Cu(111) surface $G_{\mathrm{c}} = \frac{2e^2}{h} = 77.5\,\mu\mathrm{S}$ is assumed, where e is the elementary charge and h is Planck's constant. This value corresponds to one

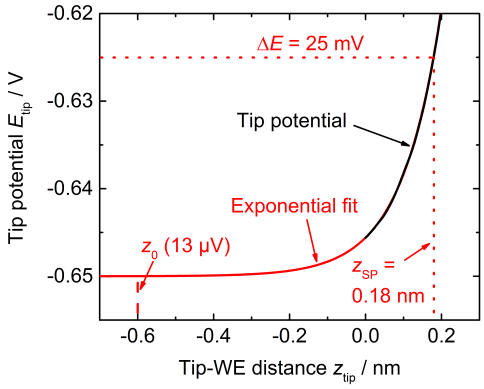

Figure 4.30.: Extrapolation of the exponential fit (red) to the potential distance curve shown in Figure 4.25 (black) to 'negative' tip-WE distances. The setpoint distance z_{SP} corresponding to $\Delta E = 25\,\mathrm{mV}$ and the 'real' tip-WE contact point calculated for a leakage current of 1 nA are indicated by dotted and dashed red lines, respectively.

conductance quantum number and is in good agreement with the literature.[156] Assuming $I_{\mathrm{tunnel}} = 1\,\mathrm{nA}$ yields $E_{\mathrm{c}} = 13\,\mu\mathrm{V}$. Extrapolating the linear fit in Figure 4.25B to $E_{\mathrm{c}} = 13\,\mu\mathrm{V}$ results in a 'real' zero-point at $z_0 = -0.60\,\mathrm{nm}$ (see Figure 4.30). Hence, the estimated distance between the tip and the WE for the images shown in this study is approximately $z_{\mathrm{tip}} = 0.78\,\mathrm{nm}$. For a leakage current of 1 pA, the extrapolation yields $z_0 = -1.31\,\mathrm{nm}$, and the corresponding tip-WE distance is approximately $z_{\mathrm{tip}} = 1.49\,\mathrm{nm}$.

5. Summary and conclusions

In this work, the influence of linker separation on catalytic activity of the oxygen reducing enzyme TvLc immobilized on mixed monolayers on Au(111) has been studied with electrochemical and EC-SPM techniques. This was followed by a methodical analysis of the working principle of the most recent of these EC-SPM techniques, the SECPM.

In the first part, TvLc immobilization on Au(111) covered with a mixed monolayer of tVA linker and MPA diluent molecules was investigated. The molecular arrangement of linkers and diluents was determined with high-resolution EC-STM. The spacing between neighboring linker molecules could be changed from close-packing in a phase-separated SAM to a distance of 1 nm in a homogeneously mixed SAM by variation of the water content in thiol solution used for monolayer formation from 0% to 4%. Enzymatic activity based on DET was determined with cyclic voltammetry and showed maximum current densities of $-0.58\,\mu A\,cm^{-2}$ for the homogeneously mixed SAM, whereas current densities were at least one order of magnitude lower on the phase-separated monolayer. This finding was explained by the accessibility of linker molecules for TvLc immobilization via induced-fit binding. In case of the phase-separated monolayer, tVA molecules are densely packed with cluster sizes exceeding the size of the hydrophobic pocket, where the active center is located. This prevents induced-fit binding and proper orientation of the enzyme. Hence, no activity is observed. On the homogeneously mixed SAM, tVA molecules are more isolated, allowing for enzymatic induced-fit binding. This facilitates DET from the electrode through the linker molecule to the T1 center of laccase,

resulting in the observed electrocatalytic activity. EC-AFM studies after enzyme immobilization showed that both surfaces were densely covered with TvLc, hence differences in bioelectrocatalytic activity related to enzyme coverages could be excluded. This is the first direct proof of the effect of linker separation on enzymatic activity. EC-STM and SECPM studies of the enzyme-covered monolayers revealed a potential-dependent image contrast, where laccase molecules could only be observed in potential ranges where enzymatic activity was measured. For EC-STM, such an effect has previously been reported, but was not expected for SECPM imaging. The enzyme coverage was found to be in agreement with literature values. In order to explain the lower enzyme activities found here compared to literature studies, a model is developed taking into account electrochemical, EIS and EC-SPM studies presented in the previous sections. According to this model, only a fraction of the enzymes is catalytically active and contributes to the measured current densities. Activity levels similar to literature values can most likely be achieved by tailoring the linker separation to the enzyme's dimensions and thus maximizing the ratio of active enzymes. Including the effect of linker separation to improve induced-fit binding in the design of new functionalized electrode surfaces for enzyme immobilization might lead to further improvements of the biocatalytic activity.

The surprising similarity between EC-STM and SECPM imaging found in the first part of the thesis triggered the subsequent systematic study of the SECPM working principle, which at that time was not fully understood. Hydroxide adsorbate layers on Cu(111) were chosen as a model system to investigate the expected, but unproven atomic or molecular resolution capability of this technique. It was possible to follow the adsorption process of hydroxide on Cu(111) with a spatial resolution similar to that of EC-STM. For the first time, high-resolution imaging with this instrument could be demonstrated by probing the molecular arrangement of OH on Cu(111). Potential-distance curves of SECPM tips at the Cu(111) surface were recorded and analyzed to determine the processes responsible for the potential used as a feedback signal in SECPM

imaging. Leakage currents have been found to be present in the instrument, which are considered to be crucial for the interpretation of the SECPM data. At distances far away from the surface, leakage currents are transported between the tip and the surface through electrochemical processes, hence potentials in this region can be interpreted as electrochemical overpotentials. At close tip-surface distances, typically used for imaging, the current-transport mechanism is identified as electron tunneling, resulting in a potential drop across the tunneling impedance. In other words, the leakage currents are responsible for the measured tip potential through the whole range of tip-to-sample distances. The tip is never at the OCP, but polarized by the leakage current. In this case, the $x-y$ imaging process is similar to an EC-STM measurement at a constant, but random tunneling current caused by the leakage currents occurring in the electronics of the SECPM setup. This explains, why no differences in enzyme imaging behavior could be found between the SECPM and EC-STM techniques. Differences in SECPM and EC-STM image contrasts reported in literature can be explained by the different feedback mechanisms (potential instead of current), low effective tunneling bias ΔE, and possibly tunneling currents that are unusually high or low compared to EC-STM.

A. Appendix

A.1. Abbreviations and symbols

α	Symmetry factor or charge transfer coefficient
a	2D lattice constant (next-neighbor spacing) in the (111) plane
a_0	3D lattice constant
a_i	Activity of species i
ABTS	2,2'-Azino-bis(3-ethylbenzothiazoline-6-sulphonic acid)
AC	Alternating current
(EC-)AFM	(Electrochemical) Atomic force microscopy
AMT	Anthracene-2-methanethiol
Au	Gold
BOx	Bilirubin oxidase
C	Carbon
C_D	Differential capacitance
C_0^*	Bulk concentration
C(ys)	Cysteine
CE	Counter electrode
ct	Charge transfer
Cu	Copper
CV	Cyclic voltammetry
D	Density of states
D_0	Diffusion coefficient
Da	Dalton corresponding to one atomic mass unit u
DC	Direct current
DET	Direct electron transfer
DFT	Density functional theory

ϵ_μ	Energy of state μ
ε_0	Vacuum permittivity ($8.854 \cdot 10^{-12}\,\mathrm{F\,m^{-1}}$)
ε	Permittivity
E	Electric potential
e	Elementary charge ($1.602 \cdot 10^{-19}\,\mathrm{C}$)
E^{00}	Standard (redox) potential
E^0	(Non-standard) redox potential
E_{corr}	Corrosion potential
$\mathfrak{E}$	Electric field
EDL	Electric double layer
EIS	Electrochemical impedance spectroscopy
η	Overpotential
F	Faraday constant ($9.649 \cdot 10^4\,\mathrm{C\,mol^{-1}}$)
F	Phenylanaline
$f(\epsilon)$	Fermi function
FWHM	Full width at half maximum
Γ_0	Surface coverage
G	Gibbs (free) energy
GCS	Gouy-Chapman-Stern
H	Enthalpy
$\hbar = \frac{h}{2\pi}$	Reduced Planck constant
H(is)	Histidine
HOPG	Highly oriented pyrolitic graphite
I	Current
IHP	Inner Helmholtz plane
IS	Inner sphere
j	Current density
j_{corr}	Corrosion current density
j_0	Exchange current density
k	Rate constant
k_{B}	Boltzmann constant ($8.617 \cdot 10^{-5}\,\mathrm{eV\,K^{-1}}$)
K_{M}	Michaelis constant
λ	Reorganization energy
λ_{D}	Debye length
$\bar{\mu}_i$	Electrochemical potential of species i
μ_i	Chemical potential of species i
$M_{\mu\nu}$	Tunneling matrix element between state μ and ν

MCO	Multicopper oxidase
MPA	3-Mercaptopropionic acid
$\mathfrak{n}_i$	Number density of species i
n	Total number of electrons transferred in an electrochemical reaction
n_i	Amount of substance i
NI	Native intermediate
NT	2-Naphthalenethiol
ν	Potential scan rate
OCP	Open circuit potential
OHP	Outer Helmholtz plane
ω	Angular frequency
ORR	Oxygen reduction reaction
OS	Outer sphere
ϕ	Work function
φ	Phase angle
PI	Peroxy intermediate
ψ	Quantum mechanical wave function
Pt	Platinum
PTFE	Polytetrafluoroethylene
q	Electric charge
R	Gas constant ($8.314\,\mathrm{J\,K^{-1}\,mol^{-1}}$)
R	Resistance
RDS	Rate determining step
RE	Reference electrode
ρ	Electric charge density
S	Entropy
SAM	Self-assembled monolayer
SECPM	Scanning electrochemical potential microscopy
SHE	Standard hydrogen electrode
σ	Surface charge
(EC-)SPM	(Electrochemical) Scanning probe microscopy
(EC-)STM	(Electrochemical) Scanning tunneling microscopy
T	Thermodynamic (absolute) temperature
ThLc	Laccase from *Trametes hirsuta*
TNC	Trinuclear cluster
tVA	Thiolated veratric acid

TvLc	Laccase from *Trametes versicolor*
U	Internal energy
u	Unit of TvLc activity corresponding to the amount of enzyme that oxidizes 1 µmol ABTS per minute
W	Tungsten
W	Warburg element
WE	Working electrode
Z	Impedance
$\mathfrak{z}_i$	Charge number of species i

A.2. Publications

Part of this work has been published:

Christoph Traunsteiner, Kaiyang Tu, Julia Kunze-Liebhäuser, High-Resolution Imaging of the Initial Stages of Oxidation of Cu(111) with Scanning Electrochemical Potential Microscopy. *ChemElectroChem*, 2:77-84, 2015.

Christoph Traunsteiner, Slawomir Sek, Carlos Valero Vidal, Julia Kunze-Liebhäuser, Laccase immobilized on a mixed thiol monolayer on Au(111) – structure-dependent activity towards oxygen reduction. *Electrochimica Acta*, 213:761-770, 2016

All permissions granted.

A.3. Conference contributions

In the following a selection of conferences is given where part of this work has been presented as a talk or poster.

Talks

06/2013	Electrochemistry at the Nanoscale, Universität Bern, Switzerland
09/2013	International Society of Electrochemistry, Querétaro, Mexico
02/2014	Electrical Characterization at the Nanoscale, Technische Universität München, Garching, Germany

Posters

06/2015	13th International Fischer Symposium, Lübeck, Germany
09/2012	GDCh-Tagung Electrochemistry 2012, Technische Universität München, München, Germany
03/2013	Bioelectrochemistry 2013, Ruhr-Universität Bochum, Bochum, Germany *Best Poster Prize Award*

A.4. Stipend and awards

- International Graduate School of Science and Engineering stipend, Technische Universität München
- Best Poster Prize Award, Bioelectrochemistry 2013
- Inside Cover Picture, ChemElectroChem 2, 2015

Bibliography

[1] United Nations Framework Convention on Climate Change. Copenhagen Accord, 2009.

[2] Rajendra K. Pachauri and Leo Meyer, editors. *IPCC, 2014: Climate Change 2014: Synthesis Report. Contribution of Working Groups I, II and III to the Fifth Assessment Report of the Intergovernmental Panel on Climate Change*. IPCC, Geneva, Switzerland, 2015.

[3] Wolf Vielstich, Arnold Lamm, and Hubert A. Gasteiger. *Handbook of Fuel Cells*. John Wiley and Sons, 2003.

[4] Hubert A. Gasteiger, Shyam S. Kocha, Bhaskar Sompalli, and Frederick T. Wagner. Activity benchmarks and requirements for Pt, Pt-alloy, and non-Pt oxygen reduction catalysts for PEMFCs. *Appl. Catal. B Environ.*, 56:9–35, 2005.

[5] Mark K. Debe. Electrocatalyst approaches and challenges for automotive fuel cells. *Nature*, 486:43–51, 2012.

[6] Alejandro G. Marangoni. *Enzyme Kinetics*. Wiley-VCH, Hoboken, New Jersey, 2002.

[7] Nicolas Mano, Valentine Soukharev, and Adam Heller. A laccase-wiring redox hydrogel for efficient catalysis of O2 electroreduction. *J. Phys. Chem. B*, 110:11180–11187, 2006.

[8] Christian H. Kjaergaard, Jan Rossmeisl, and Jens K. Nø rskov. Enzymatic versus inorganic oxygen reduction catalysts: comparison of the energy levels in a free-energy scheme. *Inorg. Chem.*, 49:3567–3572, 2010.

[9] Valentine Soukharev, Nicolas Mano, and Adam Heller. A four-electron O2-electroreduction biocatalyst superior to platinum and a biofuel cell operating at 0.88 V. *J. Am. Chem. Soc.*, 126:8368–8369, 2004.

[10] Vasile Coman, Cristina Vaz-Domínguez, Roland Ludwig, Wolfgang Harreither, Dietmar Haltrich, Antonio L. De Lacey, Tautgirdas Ruzgas, Lo Gorton, and Sergey Shleev. A membrane-, mediator-, cofactor-less glucose/oxygen biofuel cell. *Phys. Chem. Chem. Phys.*, 10:6093–6096, 2008.

[11] Yuji Kamitaka, Seiya Tsujimura, Norihiko Setoyama, Tsutomu Kajino, and Kenji Kano. Fructose/dioxygen biofuel cell based on direct electron transfer-type bioelectrocatalysis. *Phys. Chem. Chem. Phys.*, 9:1793–1801, 2007.

[12] Xuee Wu, Feng Zhao, John R. Varcoe, Alfred E. Thumser, Claudio Avignone-Rossa, and Robert C. T. Slade. A one-compartment fructose/air biological fuel cell based on direct electron transfer. *Biosens. Bioelectron.*, 25:326–331, 2009.

[13] Wenzhao Jia, Gabriela Valdés-Ramírez, Amay J. Bandodkar, Joshua R. Windmiller, and Joseph Wang. Epidermal biofuel cells: Energy harvesting from human perspiration. *Angew. Chemie - Int. Ed.*, 52:7233–7236, 2013.

[14] Michael J. Moehlenbrock and Shelley D. Minteer. Extended lifetime biofuel cells. *Chem. Soc. Rev.*, 37:1188–1196, 2008.

[15] M. N. Nasharudin, S. K. Kamarudin, U. A. Hasran, and M. S. Masdar. Mass transfer and performance of membrane-less micro fuel cell: A review. *Int. J. Hydrogen Energy*, 39:1039–1055, 2014.

[16] T. Zeng, D. Pankratov, M. Falk, S. Leimkühler, S. Shleev, and U. Wollenberger. Miniature direct electron transfer based sulphite/oxygen enzymatic fuel cells. *Biosens. Bioelectron.*, 66:39–42, 2015.

[17] J. Justin Gooding, Rahmat Wibowo, Jingquan Liu, Wenrong Yang, Dusan Losic, Shannon Orbons, Freya J. Mearns, Joe G. Shapter, and D. Brynn Hibbert. Protein electrochemistry using aligned carbon nanotube arrays. *J. Am. Chem. Soc.*, 125:9006–9007, 2003.

[18] Michael Holzinger, Alan Le Goff, and Serge Cosnier. Carbon nanotube/enzyme biofuel cells. *Electrochim. Acta*, 82:179–190, 2012.

[19] Maciej Karaskiewicz, Dominika Majdecka, Agnieszka Wieckowska, Jan F. Biernat, Jerzy Rogalski, and Renata Bilewicz. Induced-fit binding of laccase to gold and carbon electrodes for the biological fuel cell applications. *Electrochim. Acta*, 126:132–138, 2013.

[20] Scott Calabrese Barton, Josh Gallaway, and Plamen Atanassov. Enzymatic biofuel cells for implantable and microscale devices. *Chem. Rev.*, 104:4867–4886, 2004.

[21] Adam Heller. Miniature biofuel cells. *Phys. Chem. Chem. Phys.*, 6:209, 2004.

[22] Magnus Falk, Viktor Andoralov, Zoltan Blum, Javier Sotres, Dmitry B. Suyatin, Tautgirdas Ruzgas, Thomas Arnebrant, and Sergey Shleev. Biofuel cell as a power source for electronic contact lenses. *Biosens. Bioelectron.*, 37:38–45, 2012.

[23] James A. Cracknell, Kylie A. Vincent, and Fraser A. Armstrong. Enzymes as working or inspirational electrocatalysts for fuel cells and electrolysis. *Chem. Rev.*, 108:2439–2461, 2008.

[24] Pascale Chenevier, Laurent Mugherli, Sunita Darbe, Léa Darchy, Sylvain Dimanno, Phong D. Tran, Fabrice Valentino, Marina Iannello, Anne Volbeda, Christine Cavazza, and Vincent Artero. Hydrogenase enzymes: Application in biofuel

cells and inspiration for the design of noble-metal free catalysts for H2 oxidation. *Comptes Rendus Chim.*, 16:491–505, 2013.

[25] Matthew S. Thorum, Jessica Yadav, and Andrew A. Gewirth. Oxygen reduction activity of a copper complex of 3,5-diamino-1,2,4-triazole supported on carbon black. *Angew. Chemie - Int. Ed.*, 48:165–167, 2009.

[26] Adina Morozan, Bruno Jousselme, and Serge Palacin. Low-platinum and platinum-free catalysts for the oxygen reduction reaction at fuel cell cathodes. *Energy Environ. Sci.*, 4:1238–1254, 2011.

[27] Alan Le Goff, Michael Holzinger, and Serge Cosnier. Recent progress in oxygen-reducing laccase biocathodes for enzymatic biofuel cells. *Cell. Mol. Life Sci.*, 72:941–952, 2015.

[28] Christopher F. Blanford, Rachel S. Heath, and Fraser A. Armstrong. A stable electrode for high-potential, electrocatalytic O2 reduction based on rational attachment of a blue copper oxidase to a graphite surface. *Chem. Commun.*, 17:1710–1712, 2007.

[29] Christopher F. Blanford, Carina E. Foster, Rachel S. Heath, and Fraser Armstrong. Efficient electrocatalytic oxygen reduction by the 'blue' copper oxidase, laccase, directly attached to chemically modified carbons. *Faraday Discuss.*, 140:319–335, 2009.

[30] Matthew S. Thorum, Cyrus A. Anderson, Jeremy J. Hatch, Andrew S. Campbell, Nicholas M. Marshall, Steven C. Zimmerman, Yi Lu, and Andrew Gewirth. Direct, Electrocatalytic Oxygen Reduction by Laccase on Anthracene-2-methanethiol Modified Gold. *J. Phys. Chem. Lett.*, 1:2251–2254, 2010.

[31] G. Binnig, Hermann Rohrer, Ch. Gerber, and E. Weibel. Surface studies by scanning tunneling microscopy. *Phys. Rev. Lett.*, 49:57–61, 1982.

[32] G. Binnig, C. F. Quate, and Ch. Gerber. Atomic force microscope. *Phys. Rev. Lett.*, 56:930–933, 1986.

[33] Chunzeng Li and K.J. Kjoller. Scanning electrochemical potential microscope, 2007.

[34] Claudia Baier and Ulrich Stimming. Imaging single enzyme molecules under in situ conditions. *Angew. Chemie - Int. Ed.*, 48:5542–5544, 2009.

[35] Allen J. Bard and Larry R. Faulkner. *Electrochemical Methods: Fundamentals and Applications*. John Wiley & Sons, New York, NY, 2nd edition, 2001.

[36] J. O'M. Bockris, A. K. N. Reddy, and M. Gamboa-Aldeco. *Modern Electrochemistry 2A: Fundamentals of Electrodics*. Kluwer Academic Publishers, New York, NY, 2002.

[37] Carl H. Hamann, Andrew Hamnett, and Wolf Vielstich. *Electrochemistry*. Wiley-VCH, Weinheim, 2nd edition, 2007.

[38] H. Helmholtz. Studien über electrische Grenzschichten. *Ann. der Phys. und Chemie*, 243:337–382, 1879.

[39] M. Gouy. Sur la constitution de la charge électrique à la surface d'un électrolyte. *J. Phys. Théorique Appliquée*, 9:457–468, 1910.

[40] David Leonard Chapman. A contribution to the theory of electrocapillarity. *Philos. Mag. Ser. 6*, 25:475–481, 1913.

[41] Otto Stern. Zur Theorie der elektrolytischen Doppelschicht. *Zeitschrift für Elektrochemie*, 30:508–516, 1924.

[42] David C. Grahame. The electrical double layer and the theory of electrocapillarity. *Chem. Rev.*, 41:441–501, 1947.

[43] J. O'M. Bockris, M. A. V. Devanathan, and K. Müller. On the Structure of Charged Interfaces. *Proc. R. Soc. A Math. Phys. Eng. Sci.*, 274:55–79, 1963.

[44] Henry Eyring. The Activated Complex in Chemical Reactions. *J. Chem. Phys.*, 3:107–115, 1935.

[45] R. A. Marcus. On the Theory of Oxidation-Reduction Reactions Involving Electron Transfer. I. *J. Chem. Phys.*, 24:966–978, 1956.

[46] J. A. V. Butler. Studies in heterogeneous equilibria. Part II. - The kinetic interpretation of the nernst theory of electromotive force. *Trans. Faraday Soc.*, 19:729–733, 1924.

[47] Tibor Erdey-Grúz and Max Volmer. Zur Theorie der Wasserstoffüberspannung. *Z. Phys. Chem.*, 150:203–213, 1930.

[48] Carl Wagner and Wilhelm Traud. Über die Deutung von Korrosionsvorgängen durch Überlagerung von elektrochemischen Teilvorgängen und über die Potentialbildung an Mischelektroden. *Z. f. Elektroch.*, 7:391–454, 1938.

[49] Jeffrey Greeley and Nenad M. Markovic. The road from animal electricity to green energy: combining experiment and theory in electrocatalysis. *Energy Environ. Sci.*, 5:9246–9256, 2012.

[50] Marc T. M. Koper. Thermodynamic theory of multi-electron transfer reactions: Implications for electrocatalysis. *J. Electroanal. Chem.*, 660:254–260, 2011.

[51] J. Rossmeisl, A. Logadottir, and J. K. Nø rskov. Electrolysis of water on (oxidized) metal surfaces. *Chem. Phys.*, 319:178–184, 2005.

[52] Isabela C. Man, Hai-Yan Su, Federico Calle-Vallejo, Heine A. Hansen, José I. Martínez, Nilay G. Inoglu, John Kitchin, Thomas F. Jaramillo, Jens K. Nø rskov,

and Jan Rossmeisl. Universality in Oxygen Evolution Electrocatalysis on Oxide Surfaces. *ChemCatChem*, 3:1159–1165, 2011.

[53] J. Rossmeisl, Z. W. Qu, H. Zhu, G. J. Kroes, and J. K. Nø rskov. Electrolysis of water on oxide surfaces. *J. Electroanal. Chem.*, 607:83–89, 2007.

[54] A. Hamelin. Cyclic voltammetry at gold single-crystal surfaces. Part 1. Behaviour at low-index faces. *J. Electroanal. Chem.*, 407:1–11, 1996.

[55] C. Solliard and M. Flueli. Surface stress and size effect on the lattice parameter in small particles of gold and platinum. *Surf. Sci.*, 156:487–494, 1985.

[56] Ch. Wöll, S. Chiang, R. J. Wilson, and P. H. Lippel. Determination of atom positions at stacking-fault dislocations on Au(111) by scanning tunneling microscopy. *Phys. Rev. B*, 39:7988–7991, 1989.

[57] J. V. Barth, H. Brune, G. Ertl, and R. J. Behm. Scanning tunneling microscopy observations on the reconstructed Au(111) surface: Atomic structure, long-range superstructure, rotational domains, and surface defects. *Phys. Rev. B*, 42:9307–9318, 1990.

[58] D. M. Kolb. Reconstruction phenomena at metal-electrolyte interfaces. *Prog. Surf. Sci.*, 51:109–173, 1996.

[59] D.M. Kolb and J. Schneider. Surface reconstruction in electrochemistry: Au(100)-(5 x 20), Au(111)-(1 x 23) and Au(110)-(1 x 2). *Electrochim. Acta*, 31:929–936, 1986.

[60] A. Friedrich, B. Pettinger, D.M. M Kolb, G. Lüpke, R. Steinhoff, and G. Marowsky. An in situ study of reconstructed gold electrode surfaces by second harmonic generation. *Chem. Phys. Lett.*, 163:123–128, 1989.

[61] J. Christopher Love, Lara A. Estroff, Jennah K. Kriebel, Ralph G. Nuzzo, and George M. Whitesides. Self-assembled monolayers of thiolates on metals as a form of nanotechnology. *Chem. Rev.*, 105:1103–1169, 2005.

[62] Ralph G. Nuzzo and David L. Allara. Adsorption of bifunctional organic disulfides on gold surfaces. *J. Am. Chem. Soc.*, 105:4481–4483, 1983.

[63] Colin D. Bain, E. Barry Troughton, Yu-Tai Tao, Joseph Evall, George M. Whitesides, and Ralph G. Nuzzo. Formation of Monolayer Films by the Spontaneous Assembly of Organic Thiols from Solution onto Gold'. *J. Am. Chem. Soc.*, 111:321–335, 1989.

[64] Daniel K. Schwartz. Mechanisms and kinetics of self-assembled monolayer formation. *Annu. Rev. Phys. Chem.*, 52:107–137, 2001.

[65] Ornella Cavalleri, Andreas Hirstein, and Klaus Kern. Ostwald ripening of vacancy islands at thiol covered Au(111). *Surf. Sci.*, 340:L960–L964, 1995.

[66] Hannu Häkkinen. The gold-sulfur interface at the nanoscale. *Nat. Chem.*, 4:443–455, 2012.

[67] Y. Yourdshahyan, H. Zhang, and A. Rappe. n-alkyl thiol head-group interactions with the Au(111) surface. *Phys. Rev. B*, 63:81405, 2001.

[68] Paul E. Laibinis, George M. Whitesides, David L. Allara, Yu-Tai Tao, Atul N. Parikh, and Ralph G. Nuzzo. Comparison of the structures and wetting properties of self-assembled monolayers of n-alkanethiols on the coinage metal surfaces, copper, silver, and gold. *J. Am. Chem. Soc.*, 113:7152–7167, 1991.

[69] Gregory E. Poirier. Characterization of Organosulfur Molecular Monolayers on Au(111) using Scanning Tunneling Microscopy. *Chem. Rev.*, 97:1117–1128, 1997.

[70] M. E. Straumanis and L. S. Yu. Lattice parameters, densities, expansion coefficients and perfection of structure of Cu and of Cu–In α phase. *Acta Crystallogr. Sect. A*, 25:676–682, 1969.

[71] Julia Kunze, Vincent Maurice, Lorena H. Klein, Hans-Henning Strehblow, and Philippe Marcus. In Situ Scanning Tunneling Microscopy Study of the Anodic Oxidation of Cu(111) in 0.1 M NaOH. *J. Phys. Chem. B*, 105:4263–4269, 2001.

[72] V. Maurice, H.-H. Strehblow, and P. Marcus. In situ STM study of the initial stages of oxidation of Cu(111) in aqueous solution. *Surf. Sci.*, 458:185–194, 2000.

[73] Julia Kunze, Vincent Maurice, Lorena H. Klein, Hans-Henning Strehblow, and Philippe Marcus. In situ STM study of the effect of chlorides on the initial stages of anodic oxidation of Cu(111) in alkaline solutions. *Electrochim. Acta*, 48:1157–1167, 2003.

[74] Julia Kunze, Vincent Maurice, Lorena H. Klein, Hans-Henning Strehblow, and Philippe Marcus. In situ STM study of the duplex passive films formed on Cu(111) and Cu(001) in 0.1 M NaOH. *Corros. Sci.*, 46:245–264, 2004.

[75] Gadi Rothenberg. *Catalysis: Concepts and Green Applications.* 2008.

[76] Emil Fischer. Ueber die optischen Isomeren des Traubenzuckers, der Gluconsäure und der Zuckersäure. *Ber Dt Chem Ges*, 23:2611–2624, 1890.

[77] Emil Fischer. Einfluss der Configuration auf die Wirkung der Enzyme. *Ber Dt Chem Ges*, 27:2293–2985, 1894.

[78] D. E. Koshland. Application of a Theory of Enzyme Specificity to Protein Synthesis. *Proc. Natl. Acad. Sci. U. S. A.*, 44:98–104, 1958.

[79] L. Michaelis and Maud L. Menten. Die Kinetik der Invertinwirkung. *Biochem Zeit*, 49:333–369, 1913.

[80] George Edward Briggs and John Burdon Sanderson Haldane. A Note on the Kinetics of Enzyme Action. *Biochem. J.*, 19:338–339, 1925.

[81] A. Messerschmidt, R. Ladenstein, R. Huber, M. Bolognesi, L. Avigliano, R. Petruzzelli, A. Rossi, and A. Finazzi-Agró. Refined crystal structure of ascorbate oxidase at 1.9 A resolution. *J. Mol. Biol.*, 224:179–205, 1992.

[82] Edward I. Solomon, Anthony J. Augustine, and Jungjoo Yoon. O2 reduction to H2O by the multicopper oxidases. *Dalt. Trans.*, 30:3921–3932, 2008.

[83] David E. Heppner, Christian H. Kjaergaard, and Edward I. Solomon. Molecular Origin of Rapid vs. Slow Intramolecular Electron Transfer in the Catalytic Cycle of the Multicopper Oxidases. *J. Am. Chem. Soc.*, 135:12212–12215, 2013.

[84] David E. Heppner, Christian H. Kjaergaard, and Edward I. Solomon. Mechanism of the Reduction of the Native Intermediate in the Multicopper Oxidases: Insights into Rapid Intramolecular Electron Transfer in Turnover. *J. Am. Chem. Soc.*, 136:17788–17801, 2014.

[85] S. V. Shleev, O. V. Morozova, O. V. Nikitina, E. S. Gorshina, T. V. Rusinova, V. A. Serezhenkov, D. S. Burbaev, I. G. Gazaryan, and A. I. Yaropolov. Comparison of physico-chemical characteristics of four laccases from different basidiomycetes. *Biochimie*, 86:693–703, 2004.

[86] Sergey Shleev, Jan Tkac, Andreas Christenson, Tautgirdas Ruzgas, Alexander I. Yaropolov, James W. Whittaker, and Lo Gorton. Direct electron transfer between copper-containing proteins and electrodes. *Biosens. Bioelectron.*, 20:2517–2554, 2005.

[87] Hikorokuro Yoshida. Chemistry of lacquer (Urushi). Part I. *J. Chem. Soc. Trans.*, 43:472–486, 1883.

[88] Vernekar Madhavi and S. S. Lele. Laccase: Properties and applications. *BioResources*, 4:1694–1717, 2009.

[89] Edgar Ong, W. Brent R. Pollock, and Michael Smith. Cloning and sequence analysis of two laccase complementary DNAs from the ligninolytic basidiomycete Trametes versicolor. *Gene*, 196:113–119, 1997.

[90] Klaus Piontek, Matteo Antorini, and Thomas Choinowski. Crystal structure of a laccase from the fungus Trametes versicolor at 1.90-A resolution containing a full complement of coppers. *J. Biol. Chem.*, 277:37663–37669, October 2002.

[91] Maciej Klis, Elwira Maicka, Agnieszka Michota, Jolanta Bukowska, Slawomir Sek, Jerzy Rogalski, and Renata Bilewicz. Electroreduction of laccase covalently bound to organothiol monolayers on gold electrodes. *Electrochim. Acta*, 52:5591–5598, 2007.

[92] Manuel Antuch, Darío G. Abradelo, and Roberto Cao. Bioelectrocatalytic reduction of O2 at a supramolecularly associated laccase electrode. *New J. Chem.*, 38:386–390, 2014.

[93] Yvonne Beyl, Dmitrii A. Guschin, Sergey Shleev, and Wolfgang Schuhmann. A chloride resistant high potential oxygen reducing biocathode based on a fungal laccase incorporated into an optimized Os-complex modified redox hydrogel. *Electrochem. commun.*, 13(5):474–476, 2011.

[94] Magnus Falk, Zoltan Blum, and Sergey Shleev. Direct electron transfer based enzymatic fuel cells. *Electrochim. Acta*, 82:191–202, 2012.

[95] C. C. Page, C. C. Moser, X. Chen, and P. L. Dutton. Natural engineering principles of electron tunnelling in biological oxidation-reduction. *Nature*, 402:47–52, 1999.

[96] Sergey Shleev, Anna Jarosz-Wilkolazka, Anna Khalunina, Olga Morozova, Alexander Yaropolov, Tautgirdas Ruzgas, and Lo Gorton. Direct electron transfer reac-

tions of laccases from different origins on carbon electrodes. *Bioelectrochemistry*, 67:115–124, 2005.

[97] Edward I. Solomon, Uma M. Sundaram, and Timothy E. Machonkin. Multicopper Oxidases and Oxygenases. *Chem. Rev.*, 96:2563–2606, 1996.

[98] Maciej Sosna, Jean-Mathieu Chrétien, Jeremy D. Kilburn, and Philip N. Bartlett. Monolayer anthracene and anthraquinone modified electrodes as platforms for Trametes hirsuta laccase immobilisation. *Phys. Chem. Chem. Phys.*, 12:10018–10026, 2010.

[99] K. González Arzola, A. Gonzalez Orive, M. C. Arevalo, L. Vazques, A. Hernandez Creus, and M. A. Falcon. Adsorption of a Laccase from Fusarium Proliferatum on Au(111) and HOPG Electrodes: a Scanning Probe Microscopy and Electrochemical Approach. *Int. J. Electrochem. Sci.*, 7:1011–1026, 2012.

[100] Luciano Dos Santos, Victor Climent, Christopher F Blanford, and Fraser A Armstrong. Mechanistic studies of the 'blue' Cu enzyme, bilirubin oxidase, as a highly efficient electrocatalyst for the oxygen reduction reaction. *Phys. Chem. Chem. Phys.*, 12:13962–13974, 2010.

[101] Marcos Pita, Sergey Shleev, Tautgirdas Ruzgas, Victor M. Fernandez, Alexander I. Yaropolov, and Lo Gorton. Direct heterogeneous electron transfer reactions of fungal laccases at bare and thiol-modified gold electrodes. *Electrochem. commun.*, 8:747–753, 2006.

[102] Victor Climent, Jingdong Zhang, Esben Peter Friis, Lars Henrik Ø stergaard, and Jens Ulstrup. Voltammetry and Single-Molecule in Situ Scanning Tunneling Microscopy of Laccases and Bilirubin Oxidase in Electrocatalytic Dioxygen Reduction on Au(111) Single-Crystal Electrodes. *J. Phys. Chem. C*, 116:1232–1243, 2012.

[103] Dmitry Pankratov, Javier Sotres, Alejandro Barrantes, Thomas Arnebrant, and Sergey Shleev. Interfacial behavior and activity of laccase and bilirubin oxidase on bare gold surfaces. *Langmuir*, 30:2943–2951, 2014.

[104] Sergey Shleev, Marcos Pita, Alexander I. Yaropolov, Tautgirdas Ruzgas, and Lo Gorton. Direct Heterogeneous Electron Transfer Reactions of Trametes hirsuta Laccase at Bare and Thiol-Modified Gold Electrodes. *Electroanalysis*, 18:1901–1908, 2006.

[105] Urszula Salaj-Kosla, Sascha Pöller, Wolfgang Schuhmann, Sergey Shleev, and Edmond Magner. Direct electron transfer of Trametes hirsuta laccase adsorbed at unmodified nanoporous gold electrodes. *Bioelectrochemistry*, 91:15–20, 2013.

[106] Gautam Gupta, Vijaykumar Rajendran, and Plamen Atanassov. Bioelectrocatalysis of Oxygen Reduction Reaction by Laccase on Gold Electrodes. *Electroanalysis*, 16:1182–1185, 2004.

[107] M. L. Mena, V. Carralero, A. González-Cortés, P. Yáñez Sedeño, and J. M. Pingarrón. Laccase Biosensor Based on N-Succinimidyl-3-Thiopropionate-Functionalized Gold Electrodes. *Electroanalysis*, 17:2147–2155, 2005.

[108] Marcos Pita, Cristina Gutierrez-Sanchez, David Olea, Marisela Velez, Cristina Garcia-Diego, Sergey Shleev, Victor M. Fernandez, and Antonio L. De Lacey. High Redox Potential Cathode Based on Laccase Covalently Attached to Gold Electrode. *J. Phys. Chem. C*, 115:13420–13428, 2011.

[109] Cristina Vaz-Domínguez, Marcos Pita, Antonio L. de Lacey, Sergey Shleev, and Angel Cuesta. Combined ATR-SEIRAS and EC-STM Study of the Immobilization of Laccase on Chemically Modified Au Electrodes. *J. Phys. Chem. C*, 116:16532–16540, 2012.

[110] Piotr Olejnik, Barbara Palys, Agata Kowalczyk, and Anna M. Nowicka. Orientation of Laccase on Charged Surfaces. Mediatorless Oxygen Reduction on Amino- and Carboxyl-Ended Ethylphenyl Groups. *J. Phys. Chem. C*, 116:25911–25918, 2012.

[111] J. Tersoff and D. R. Hamann. Theory of the scanning tunneling microscope. *Phys. Rev. B*, 31:805–813, 1985.

[112] J. Bardeen. Tunnelling from a Many-Particle Point of View. *Phys. Rev. Lett.*, 6:57–59, 1961.

[113] C. Julian Chen. Origin of atomic resolution on metal surfaces in scanning tunneling microscopy. *Phys. Rev. Lett.*, 65:448–451, 1990.

[114] C. Julian Chen. Microscopic view of scanning tunneling microscopy. *J. Vac. Sci. Technol. A Vacuum, Surfaces, Film.*, 9:44–50, 1991.

[115] Roland Wiesendanger and H.-J. Güntherodt. *Scanning Tunneling Microscopy III*. Springer-Verlag, Berlin Heidelberg, 1993.

[116] G. Binnig, N. Garcia, H. Rohrer, J. M. Soler, and F. Flores. Electron-metal-surface interaction potential with vacuum tunneling: Observation of the image force. *Phys. Rev. B*, 30:4816–4818, 1984.

[117] G. E. Engelmann, J. C. Ziegler, and D. M. Kolb. Electrochemical fabrication of large arrays of metal nanoclusters. *Surf. Sci.*, 401:L420—-L424, 1998.

[118] D-H. Woo, E-M. Choi, Y-H. Yoon, K-J. Kim, I.C. C Jeon, and H. Kang. Current–distance–voltage characteristics of electron tunneling through an electrochemical STM junction. *Surf. Sci.*, 601:1554–1559, 2007.

[119] Richard Sonnenfeld and Paul K. Hansma. Atomic-resolution microscopy in water. *Science (80-.).*, 232:211–213, 1986.

[120] P. Lustenberger, H. Rohrer, R. Christoph, and H. Siegenthaler. Scanning tunneling microscopy at potential controlled electrode surfaces in electrolytic environment. *J. Electroanal. Chem. Interfacial Electrochem.*, 243:225–235, 1988.

[121] Kingo Itaya and Eisuke Tomita. Scanning tunneling microscope for electrochemistry - a new concept for the in situ scanning tunneling microscope in electrolyte solutions. *Surf. Sci.*, 201:L507–L512, 1988.

[122] M. Nonnenmacher, M. P. O'Boyle, and H. K. Wickramasinghe. Kelvin probe force microscopy. *Appl. Phys. Lett.*, 58:2921–2923, 1991.

[123] Andrew C. Hillier, Sunghyun Kim, and Allen J. Bard. Measurement of Double-Layer Forces at the Electrode/Electrolyte Interface Using the Atomic Force Microscope: Potential and Anion Dependent Interactions. *J. Phys. Chem.*, 100:18808–18817, 1996.

[124] Desiree Barten, J. M. Kleijn, J. Duval, H. P. v. Leeuwen, J. Lyklema, and M. A. Cohen Stuart. Double layer of a gold electrode probed by AFM force measurements. *Langmuir*, 19:1133–1139, 2003.

[125] Dae-ha Woo, Jung-suk Yoo, Su-moon Park, Il C. Jeon, and Heon Kang. Direct Probing into the Electrochemical Interface Using a Novel Potential Probe: Au(111) Electrode / NaBF4 Solution Interface. *Bull. Korean Chem. Soc.*, 25:577–580, 2004.

[126] C. Hurth, C. Li, and A.J. Bard. Direct Probing of Electrical Double Layers by Scanning Electrochemical Potential Microscopy. *J. Phys. Chem. C*, 111:4620–4627, 2007.

[127] Young-Hwan Yoon, Dae-Ha Woo, Taeho Shin, Taek Dong Chung, and Heon Kang. Real-Space Investigation of Electrical Double Layers. Potential Gradient Measurement with a Nanometer Potential Probe. *J. Phys. Chem. C*, 115:17384–17391, 2011.

[128] R. F. Hamou, P. U. Biedermann, A. Erbe, and M. Rohwerder. Numerical simulation of probing the electric double layer by scanning electrochemical potential microscopy. *Electrochim. Acta*, 55:5210–5222, 2010.

[129] R. F. Hamou, P. U. Biedermann, A. Erbe, and M. Rohwerder. Numerical analysis of Debye screening effect in electrode surface potential mapping by scanning electrochemical potential microscopy. *Electrochem. commun.*, 12:1391–1394, 2010.

[130] C. Corbella, E. Pascual, G. Oncins, C. Canal, J.L. L Andújar, and E. Bertran. Composition and morphology of metal-containing diamond-like carbon films obtained by reactive magnetron sputtering. *Thin Solid Films*, 482:293–298, 2005.

[131] Holger Wolfschmidt, Claudia Baier, Stefan Gsell, Martin Fischer, Matthias Schreck, and Ulrich Stimming. STM, SECPM, AFM and Electrochemistry on Single Crystalline Surfaces. *Materials (Basel).*, 3:4196–4213, 2010.

[132] Sergei Kalinin and Alexei Gruverman. *Scanning Probe Microscopy*. Springer Science+Business Media, New York, NY, 2007.

[133] R García. Dynamic atomic force microscopy methods. *Surf. Sci. Rep.*, 47:197–301, 2002.

[134] S. Manne, P. K. Hansma, J. Massie, V. B. Elings, and A. A. Gewirth. Atomic-resolution electrochemistry with the atomic force microscope: copper deposition on gold. *Science (80-.).*, 251:183–186, 1991.

[135] Andreas Engel, Cora-Ann Schoenenberger, and Daniel J Müller. High resolution imaging of native biological sample surfaces using scanning probe microscopy. *Curr. Opin. Struct. Biol.*, 7:279–284, 1997.

[136] J. Clavilier, R. Faure, G. Guinet, and R. Durand. Preparation of monocrystalline Pt microelectrodes and electrochemical study of the plane surfaces cut in the direc-

tion of the {111} and {110} planes. *J. Electroanal. Chem. Interfacial Electrochem.*, 107:205–209, 1979.

[137] J. A. Allen. Solubility of Oxygen in Water. *Nature*, 175:83–83, 1955.

[138] L. A. Nagahara, T. Thundat, and S. M. Lindsay. Preparation and characterization of STM tips for electrochemical studies. *Rev. Sci. Instrum.*, 60:3128–3130, 1989.

[139] M. J. Giz, B. Duong, and N. J. Tao. In situ STM study of self-assembled mercaptopropionic acid monolayers for electrochemical detection of dopamine. *J. Electroanal. Chem.*, 465:72–79, 1999.

[140] M. J. Esplandiú, H. Hagenström, and D. M. Kolb. Functionalized Self-Assembled Alkanethiol Monolayers on Au(111) Electrodes: 1. Surface Structure and Electrochemistry. *Langmuir*, 17:828–838, 2001.

[141] Sergey Shleev, Andreas Christenson, Vladimir Serezhenkov, Dosymzhan Burbaev, Alexander Yaropolov, Lo Gorton, and Tautgirdas Ruzgas. Electrochemical redox transformations of T1 and T2 copper sites in native Trametes hirsuta laccase at gold electrode. *Biochem. J.*, 385:745–754, 2005.

[142] Yousung Kim, Nam Seok Cho, Tae J. Eom, and Woonsup Shin. Purification and characterization of a laccase from Cerrena unicolor and its reactivity in lignin degradation. *Bull. Korean Chem. Soc.*, 23:985–989, 2002.

[143] László Fejes Tóth. *Lagerungen in der Ebene auf der Kugel und im Raum.* Springer Verlag, Berlin Heidelberg, 1953.

[144] O. V. Morozova, G. P. Shumakovich, M. A. Gorbacheva, S. V. Shleev, and A. I. Yaropolov. "Blue" laccases. *Biochemistry. (Mosc).*, 72:1136–1150, 2007.

[145] Patrick L Holland and William B. Tolman. A Structural Model of the Type 1 Copper Protein Active Site: N2S(thiolate)S(thioether) Ligation in a Cu(II) Complex. *J. Am. Chem. Soc.*, 122:6331–6332, 2000.

[146] Walter Canon-Mancisidor, Evgenia Spodine, Diego Venegas-Yazigi, Dario Rojas, Jorge Manzur, and Santiago Alvarez. Electrochemical Behavior of Copper Complexes with Substituted Polypyridinic Ligands: An Experimental and Theoretical Study. *Inorg. Chem.*, 47:3687–3692, 2008.

[147] Lei Yang and William B. Tolman. Type 1 copper site synthetic model complexes with increased redox potentials. *J. Biol. Inorg. Chem.*, 17(2):285–291, 2012.

[148] Th. Heumann and N. Stolica. The electrochemical behaviour of tungsten—II. The dissolution of tungsten in NaOH solutions. *Electrochim. Acta*, 16:1635–1646, 1971.

[149] J. R. Hahn, Y. A. Hong, and H. Kang. Electron tunneling across an interfacial water layer inside an STM junction: tunneling distance, barrier height and water polarization effect. *Appl. Phys. A Mater. Sci. Process.*, 66:S467–S472, 1998.

[150] Martin Hugelmann and Werner Schindler. Tunnel barrier height oscillations at the solid/liquid interface. *Surf. Sci.*, 541:L643–L648, 2003.

[151] R. S. Lillard. The Nature of Oxide Films on Tungsten in Acidic and Alkaline Solutions. *J. Electrochem. Soc.*, 145:2718, 1998.

[152] M. Anik and K. Osseo-Asare. Effect of pH on the Anodic Behavior of Tungsten. *J. Electrochem. Soc.*, 149:B224–B233, 2002.

[153] Mark C. Weidman, Daniel V. Esposito, Irene J. Hsu, and Jingguang G. Chen. Electrochemical Stability of Tungsten and Tungsten Monocarbide (WC) Over Wide pH and Potential Ranges. *J. Electrochem. Soc.*, 157:F179–F188, 2010.

[154] T. Tuvić, I. Pašti, and S. Mentus. Tungsten electrochemistry in alkaline solutions—Anodic dissolution and oxygen reduction reaction. *Russ. J. Phys. Chem. A*, 85:2399–2405, 2011.

[155] J. P. Ibe. On the electrochemical etching of tips for scanning tunneling microscopy. *J. Vac. Sci. Technol. A Vacuum, Surfaces, Film.*, 8:3570–3575, 1990.

[156] L. Limot, J. Kröger, R. Berndt, A. Garcia-Lekue, and W. Hofer. Atom Transfer and Single-Adatom Contacts. *Phys. Rev. Lett.*, 94:126102, 2005.